Development and testing of antenna and subsystems for MIST, a 21-cm global signal experiment to study the Cosmic Dawn

Matheus Azevedo Silva Pessôa
Department of Physics & McGill Space Institute
McGill University, Montréal
July, 2021

A thesis submitted to McGill University in partial fulfillment of the requirements of the degree of

Master of Science

Abstract

The epoch when the first stars in the Universe were born is an unsolved mystery in cosmology. Observations of this time are possible only through measurements of the redshifted 21-cm neutral hydrogen line, which are fundamental to our understanding of the Universe. The epoch known as the Cosmic Dawn can be probed by making 21–cm brightness temperature measurements averaged spatially across the sky, and the glow of the first stars is expected to cause a spectral absorption feature in this global signal. The EDGES experiment in 2018 reported an absorption feature centered at 78 MHz, with 0.5 K in depth; this absorption feature can be interpreted as being a detection of the global signal. RFI contamination, strong foreground emissions from the Milky Way ($\sim 10^3$ K), ionospheric effects, and instrumental systematics are the biggest challenges to overcome experimentally, representing the primary limitations in obtaining a high-fidelity detection, and therefore new independent measurements are necessary. This thesis focuses on the development of MIST and Mini-MIST, new experimental efforts for detecting the global signal. These instruments will be installed in northern Chile and at the McGill Arctic Research Station (MARS), two of the most radio quiet sites on Earth. Because the measurement is limited by systematics, rather than statistical error, the primary challenge is precise design and characterization of MIST subsystems. The ultimate goal involves distinguishing the signal from Galactic foreground emission, which requires rigorously calibrating the instrument to approximately 1 part in 10^4. This thesis presents the development of a variety of MIST subsystems, including antenna design, readout electronics characterization, data acquisition, software development, and environmental monitoring of soil conductivity and permittivity. With our efforts, MIST and Mini-MIST will provide invaluable, independent measurements of the Cosmic Dawn signal.

Abrégé

L'époque de la naissance des premières étoiles de l'Univers est un mystère non résolu en cosmologie. Les observations de cette époque ne sont possibles que grâce à des mesures de la raie de l'hydrogène neutre décalée vers le rouge de 21 cm, qui sont fondamentales pour notre compréhension de l'Univers. L'époque connue sous le nom d'aube cosmique peut être sondée en effectuant des mesures de température de luminosité de 21 cm moyennées spatialement dans le ciel, et la lueur des premières étoiles devrait provoquer une caractéristique d'absorption spectrale dans ce signal global. L'expérience EDGES en 2018 a signalé une caractéristique d'absorption centrée à 78 MHz, avec une profondeur de $0,5$ K ; cette caractéristique d'absorption peut être interprétée comme étant une détection du signal global. La contamination RFI, les fortes émissions de premier plan de la Voie lactée ($\sim 10^3$ K), les effets ionosphériques et la systématique instrumentale sont les plus grands défis à surmonter expérimentalement, représentant les principales limitations pour obtenir une détection haute fidélité, et donc de nouveaux des mesures indépendantes sont nécessaires. Cette thèse porte sur le développement de MIST et Mini-MIST, de nouveaux efforts expérimentaux pour détecter le signal global. Ces instruments seront installés dans le nord du Chili et à la McGill Arctic Research Station (MARS), deux des sites les plus silencieux de la planète. Étant donné que la mesure est limitée par la systématique plutôt que par l'erreur statistique, le principal défi est la conception et la caractérisation précises des sous-systèmes MIST. Le but ultime consiste à distinguer le signal de l'émission de premier plan galactique, ce qui nécessite de calibrer rigoureusement l'instrument à environ 1 partie pour 10^4. Cette thèse présente le développement d'une variété de sous-systèmes MIST, y compris la conception d'antennes, la caractérisation de l'électronique de lecture, l'acquisition de données, le développement de logiciels et la surveillance environnementale de la conductivité et de la permittivité du sol. Grâce à nos efforts, MIST et Mini-MIST fourniront des mesures indépendantes et inestimables du signal de l'aube cosmique.

Acknowledgements

If I had a time machine and could go back in time to show this thesis to the 14-year-old Matheus that was starting to feel amazed about studying physics, I would definitely do so. And I am pretty sure I would have felt like dreaming, since this indeed is a dream to me. Studying at a university outside Brazil, and on the path to become a scientist are two things I always dreamed about, and therefore I am very grateful for this.

I would like to thank Cynthia first, for being so kind to me even on the first-ever e-mails we exchanged back in 2018, when I was still deciding to apply for the program. She gave me an opportunity when I thought no one else would, and has been an amazing supervisor from the first day I got accepted into the program. Cynthia's enthusiasm for life and science have inspired me to go through all difficulties I had during these 2 years, and I am really grateful. Second, I would like to thank Raul for all the discussions we had throughout these years. I have learned a whole lot about radio astronomy and instrumentation thanks to him, and the great work he developed. Being able to work with someone as skilled as Raul is a unique, and I am thankful for this. I would like to thank Jon for teaching me how to code, and for having all the patience to cover a same topic with me lots of times. Thanks to Eamon, for helping on the first steps of the device to measure EM properties. Finally, thanks also for the entire MIST collaboration, for providing me valuable inputs and suggestions to make my work better.

This thesis is also dedicated to the friends I have made in the Physics Department, and in the MSI. You supported me when I most needed, and I will never forget that. These environments have definitely made a better physicist, and I always felt inspired by the works that are developed there. This is also to my friends in Montréal, for having made my life during the winter much happier, and made me feel like home even being far, far away.

Finally, I would like to thank all my family for the unconditional support. This is specially dedicated to Eliane and Leonardo, my mom and dad, who have been by my side during my entire life, even at distance, and during the hardest moments. Thank you for believing in me, for never giving up, and for being the best parents. Eu amo vocês.

É engraçado escrever essa dedicatória em inglês, deixando somente as últimas palavras em português. De muitas formas, eu acredito que ao escrever nessa língua, que não é a minha primeira

língua, acaba tirando um pouco de toda a parte da emoção que eu vivi durante os meus estudos no mestrado. Foram muitas. Muitos desafios, muitas superações, momentos difíceis, principalmente quando eu cheguei aqui em Montréal. Vendo as coisas sob uma nova perspectiva, eu vejo o quanto eu cresci. Os primeiros meses foram difíceis. O segundo ano passou num sopro. Eu sou muito grato às pessoas especiais que são muito próximas a mim, e que sempre tentam me fazer a cada dia melhor. Não sei o que vai acontecer daqui para frente na minha trajetória, mas se eu pudesse dizer algo para quando eu mesmo revisitar esta tese, é o seguinte: valeu a pena. Eu vivi o sonho.

Matheus

"O correr da vida embrulha tudo,
a vida é assim: esquenta e esfria,
aperta e daí afrouxa,
sossega e depois desinquieta.
O que ela quer da gente é coragem.
O que Deus quer é ver a gente
aprendendo a ser capaz
de ficar alegre a mais,
no meio da alegria,
e inda mais alegre
ainda no meio da tristeza!
A vida inventa!
A gente principia as coisas,
no não saber por que,
e desde aí perde o poder de continuação
porque a vida é mutirão de todos,
por todos remexida e temperada.
O mais importante e bonito, do mundo, é isto:
que as pessoas não estão sempre iguais,
ainda não foram terminadas,
mas que elas vão sempre mudando.
Afinam ou desafinam. Verdade maior.
Viver é muito perigoso; e não é não.
Nem sei explicar estas coisas.
Um sentir é o do sentente, mas outro é do sentidor."
Guimarães Rosa

The MIST Collaboration

McGill University H. Cynthia Chiang, Jonathan Sievers, Raul Monsalve (CO-P.I.), Matheus Pessôa, Ericka Hornecker, Ian Hendricksen, Christian Bye.

Universidad Católica de la Santísima Concepción Ricardo Bustos (P.I.), Mauricio Díaz.

Universidad de Chile Oscar Restrepo, Patricio Mena.

Table of Contents

List of Figures

List of Tables

Chapter 1

Introduction

> Stands at the sea, wonders at
> wondering: I, a universe of atoms
> an atom in the universe.
>
> Richard Feynman

Cosmology is the field dedicated to studying the whole universe and its components. Throughout history, different civilizations have provided explanations on the cosmos based on interactions with the environment, and natural phenomena. All the steps towards a comprehension of the universe have led to modern cosmology: the latest ideas in the field that can be put to test nowadays thanks to the emergence of new technologies and techniques that allow precise measurements and observations.

Some discoveries have revolutionized the way we have perceived and described the universe. One of the earliest ones was development of a theory that described gravity and allowed the interpretation of the motion astronomical objects, by Isaac Newton. The expansion of the Universe was discovered with measurements of radial velocities of extra-galactic nebulae [Hubble, 1929]. The development of the theory of general relativity (GR) allowed a description of the relationship between spacetime geometry and energy content. The measurements of an antenna excess noise by Wilson and Penzias, later identified as the cosmic microwave background (CMB) [Penzias and Wilson, 1965], which allowed new cosmological models to be tested. Recent CMB measurements probe cosmological parameters that allow a better description of the universe from its earliest stages up until today [Aghanim et al., 2020].

In this chapter, we will describe the cosmological framework in which this thesis is inserted. The 21-cm global signal, an essential tool for studying the universe in its early stages, will be described in detail with its evolution through cosmic history. Current 21–cm global signal experiments are also presented, as well as the only detection from the Cosmic Dawn that happened in 2018 and

raised questions about our current understanding of the universe. Further experimental proof is needed, and independent confirmations will allow cosmological constraints to be put to test.

1.1 Principles of Cosmology

The cosmological principle states that, at all times, the universe is expanding in all directions. On large scales, the universe is isotropic and homogeneous. To understand these concepts, we picture the distribution of galaxies in the universe. Homogeneity states that, within the whole universe, no matter where in space, the distribution of galaxies will follow the same pattern, and the universe will look the same. Isotropy states that, within the universe, at all viewing angles and directions, the observable universe is, again, the same. The expansion of the universe is obeys Hubble's law,

$$v = H_o d, \tag{1.1}$$

where the velocity v is linearly related to the distance d by Hubble's constant, $H_0 \approx 67\,\mathrm{km\,s^{-1}Mpc^{-1}}$. The value of H_0 is still debated in cosmology, since local observables and the CMB yield results that are in slight tension [Bernal et al., 2016]. The implication of expansion, expressed by this equation, brought important questions:i) if the universe is still expanding today, what happened in a moment prior to expansion? ii) is there a limit for the expansion of the universe? iii) what is the ultimate fate of our universe? To answer these questions, we need a description of the universe in terms of its dynamics, evolution, and its different components. I will start by describing the Standard Big Bang Model (SBB), how it answers some questions, and more importantly, what questions remained unsolved, which motivated new theories.

The SBB provides a depiction of the story of the universe and explains some fundamental questions: the expansion of the universe; the formation of elements in its early stages, in a process called Big Bang Nucleosynthesis (BBN), also explaining the abundances observed today for lithium, helium and deuterium; and the presence of background radiation with a distribution well-described by a blackbody spectrum, acknowledged as the CMB, the oldest light in the universe. In the model, at large scales the universe can be considered homogeneous and isotropic [Baumann, 2009]; matter can be described as a perfect fluid that obeys classical fluid dynamic equations [Brandenberger, 2004]; GR explains the overall dynamics of the universe by Einsten's field equations that govern the interplay between the metric, and the stress-energy tensor. The Friedmann-Robertson-Walker (FRW) metric

$$ds^2 = -dt^2 + a^2\left(\frac{dr^2}{1-\kappa r^2} + r^2(d\theta^2 + \sin^2\theta d\phi^2)\right), \tag{1.2}$$

describes the overall dynamics in a homogeneous and isotropic universe at large scales with a scale factor $a(t)$, where κ is a curvature. In an expanding universe, the distance to an object of interest is given by $d = a(t)d_0$, where d is the proper distance, d_0 is a reference distance at a time t_0. The scale factor is also defined in terms of the Hubble parameter as, $H \equiv \dot{a}/a$, where the dot represents a time derivative. In Equation 1.2, κ defines the curvature of spacetime: κ=0 indicates a flat universe, and $\kappa = \pm 1$ indicates a positively or negatively curved universe. Using Einstein's field equations, it is possible to write the Friedmann Equations from this metric as

$$\left(\frac{\dot{a}}{a}\right) - \frac{\kappa}{a^2} = \frac{8\pi G}{3}\rho, \tag{1.3}$$

$$\frac{\ddot{a}}{a} = -\frac{4\pi G}{3}(\rho + 3p), \tag{1.4}$$

where p represents the pressure, and ρ the energy densities of the different components. A combination of these produces a continuity equation from which the assumption of matter as being described by a classical fluid is used. The equation of state

$$p = \omega\rho, \tag{1.5}$$

allows the description of each constituent of the universe as a function of the scale factor $a(t)$: matter, radiation, and vacuum. For baryonic matter, we have $\omega = 0$, and the energy density evolves as $\rho_m(t) \propto a(t)^{-3}$; for radiation (photons and neutrinos, for example), $\rho_r(t) \propto a(t)^{-4}$. We can define a critical energy density ρ_c, which accounts for the matter density needed to make the curvature of the Universe approach the one of a flat universe, ($\kappa = 0$) [Baumann, 2009], as

$$\rho_c \equiv \frac{3H_0^2}{8\pi G}, \tag{1.6}$$

where $G = 6.674 \times 10^{11}$ m^3 kg^{-1} s^{-2} is Newton's gravitational constant. We can write the evolution of the scale factor explicitly as a function of the universe's components as

$$\left(\frac{\dot{a}}{a}\right)^2 \equiv H^2(t) = H_0^2\left[\frac{8}{3}\pi G\rho_i - \frac{\kappa}{a^2} + \frac{\Lambda}{3}\right] = H_0^2\left[\frac{\Omega_{\gamma,0}}{a^4} + \frac{\Omega_{m,0}}{a^3} + \frac{\Omega_{\kappa,0}}{a^2} + \Omega_{\Lambda,0}\right]. \tag{1.7}$$

In this equation, Ω_γ represents the present radiation density, Ω_m the present baryonic matter density, Ω_K the curvature, and Ω_Λ the present cosmological constant. To write these energy densities, we have defined $\Omega_i \equiv \frac{\rho_{i,0}}{\rho_c}$ for each i -th component to write in the most compact form, where $\rho_{i,0}$ represents the current energy density for each. The evolution of the universe can therefore be described by the epochs when each component dominated: at earlier times, radiation was the dominant component; later on, matter started to dominate and more recently, the cosmological

constant Λ took over. The timeline of the story of the universe is usually described in terms of a redshift parameter z, defined in terms of the scale factor

$$1 + z = \frac{a_0}{a(t)}, \tag{1.8}$$

where a_0 represents the present scale factor, which is equal to unity. As we increase in z, we are going back in time, to earlier epochs. The SBB model is not perfect [Brandenberger, 2000]. Cosmological parameters from the latest CMB measurements support the claim that the universe is spatially flat [Aghanim et al., 2020], but theoretically this would require a fine-tuning of initial conditions of orders up to 10^{-50}. This is called the flatness problem, as it cannot be explained by SBB. The horizon problem emerges from observations of the CMB, which point towards an isotropy across the sky. This implies that the particles were causally connected in the past, to have reached thermal equilibrium. However, they do not share the same horizon, and therefore cannot have been causally connected. A period of inflation was introduced, as a way to solve both flatness and horizon problems. During this phase, the universe expanded exponentially, and the scale factor evolved as,

$$a(t) \sim e^{Ht}. \tag{1.9}$$

According to inflation, the universe experienced an accelerated expansion process at approximately 10^{-35} s after the Big Bang. During the very early universe, to sustain a model which predicts an inflationary phase, the consideration that an ideal gas can describe the first instants of the universe breaks down, and quantum gravity needs to be introduced. Different inflationary theories have been discussed over the last decades [Brandenberger, 2011]. There is no experimental evidence that support these theories in a way to create a consensus within the cosmology community. Nevertheless, observational data from the CMB places contraints on different classes of these models.

In Figure 1.1, there is a depiction of the history of the universe. At high redshifts, after the Big Bang, the universe was in a hot, dense state. The four known forces of nature (electromagnetic, gravitational, weak nuclear force and strong nuclear force) might have been part of just one fundamental force. The first elementary particles and antiparticles were formed after the decoupling of gravity from the other three, and the universe consisted mostly of a quark-gluon plasma (QGP). Inflation took place, after which the QGP became widely spread throughout the expanded universe. As the universe kept expanding and cooling, the first hadrons (protons and electrons) were generated. In the first 3 minutes, the universe evolved from a soup of fundamental particles ($T \sim 10^{15}$ K) to an enviroment where the formation of the first atomic nuclei for hydrogen, helium and lithium occurred ($T \sim 10^{10}$) K [Baumann, 2009].

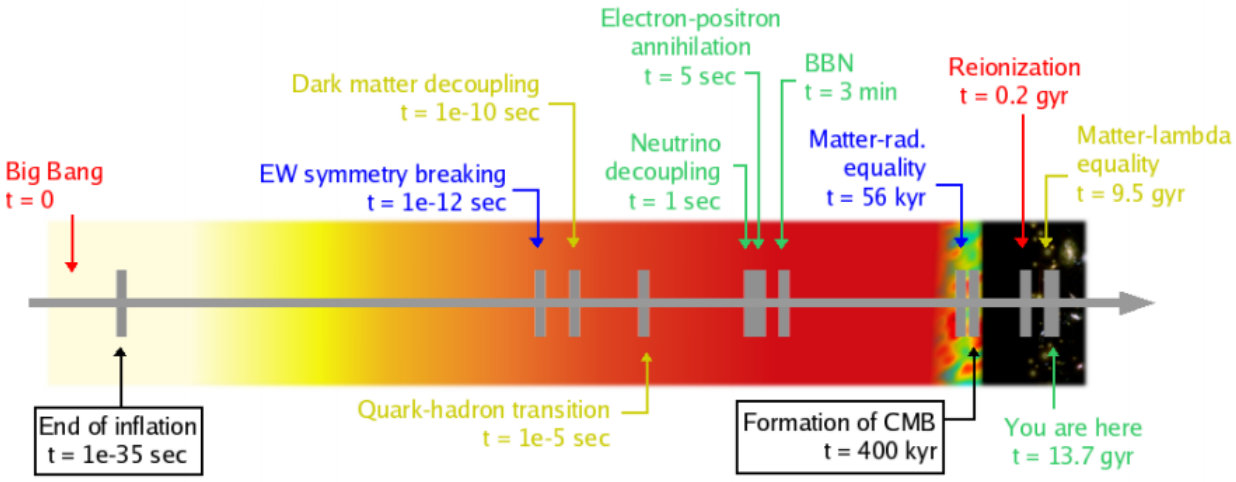

Figure 1.1: A brief story of the universe, ever since the big bang until its current stage. During the very early universe stage, all forces were combined into one. Their decoupling triggered the inflationary stage, thus explaining the large scale structures (LSS) we see today, and the isotropies in the CMB. 21–cm experiments try to map the following stage, since the Dark Ages until the EoR, a time in which the brightness temperature of the 21–cm line has suffered fluctuations due to the ignition of the first stars in the universe. Picture taken from [Chiang, 2009].

After the formation of the first atomic nuclei, there was a radiation-dominated phase when photons interacted with elementary particles that lasted until the period known as recombination, when the formation of neutrally charged atoms happened. This allowed light to travel freely through space and time, as the universe became transparent to this radiation. This observable radiation is the CMB, a red glow which can be described by a blackbody spectrum with $T \sim 2.73$ K.

The universe continued cooling down and started a new phase, known as the Dark Ages, since the CMB glow shifted to infrared and would be invisible to human eyes [Miralda-Escudé, 2003]. The luminous objects were created when the first stars ignited due to the collapse of overdense regions, during a period known as the Cosmic Dawn. The glow of the first stars along with increasing ultraviolet (UV) radiation later ionized the cosmic gas present in the intergalactic medium (IGM) completely, a period known as the Epoch of Reionization (EoR) [Zaroubi, 2013]. 21–cm radiation, emitted by hydrogen when it undergoes a spin-flip transition, is an important tool to study these early epochs of the universe.

1.2 21-cm Cosmology

The spin flip transition in neutral hydrogen is a phenomenon that allows us to study the evolution of the universe. Atomic hydrogen is composed of a proton and an electron that have intrinsic spins. In classical theory, the motion of the electron orbiting the proton is responsible for generating a magnetic field, which couples the proton and electron spins. The ground state of hydrogen is however dynamical; spin transitions are allowed and release energy in the form of radiation due to the close gap between energies in the 4 spin states of proton and electron (p^u, p^d, e^u, e^d) that compose this **hyperfine structure** of hydrogen. The process of exchanging energetically close spin states is called **hyperfine splitting**.

1.2.1 Hyperfine splitting of hydrogen

To understand how the hyperfine splitting of hydrogen happens, we first need to build the physical model, that involves both classical and quantum theories. On one hand, we will explain the electromagnetic process that allows the spin flip transition to occur, and then we discuss the quantum nature. We take an approach that starts with electromagnetic modelling to describe the interaction between proton and electron, and then move on to the quantum considerations, described in more detail in [Griffiths, 1982]. The discussion that follows is also highly based on this paper. We treat proton p and electron e as two perfect dipoles. As e orbits, a magnetic field $\mathbf{B}$ will be generated, and will interact with the magnetic moment of p, $\mathbf{m_p}$. The induced magnetic field is described by

$$\mathbf{B}(\mathbf{r}) = \frac{\mu_0}{4\pi}\frac{1}{r^3}[3(\mathbf{m_e}\cdot\hat{r})\hat{r} - \mathbf{m_e}] + \frac{2}{3}\mu_0\mathbf{m_e}\delta^3(\mathbf{r}), \tag{1.10}$$

where μ_0 represents the vacuum permeability, and $\delta(\mathbf{r})$ a delta function, and $\mathbf{r}$, a position vector. The interaction of $\mathbf{B}$ with $\mathbf{m_p}$ can be also considered as the Hamiltonian for the system, $H = -\mathbf{m_p}\mathbf{B}(\mathbf{r})$. Combined with Equation 1.10, we get

$$H = -\frac{\mu_0}{4\pi r^3}(\mathbf{m_p}\cdot\mathbf{m_e})(3\cos^2\theta - 1) - \frac{2}{3}\mu_0(\mathbf{m_p}\cdot\mathbf{m_e})\delta^3(\mathbf{r}). \tag{1.11}$$

From this interaction Hamiltonian, we reach a point where we need quantum physics. We can take the expectation value of this Hamiltonian in order to get the associated energy states, considering first-order perturbation theory. For hydrogen, the ground state energy can be described by

$$E = \int \psi_0 H \psi_0^* d\Omega, \tag{1.12}$$

where we take the integration over a spherical surface, with $d\Omega = r^2 \sin\theta d\theta d\phi$, and ψ_0 are the wavefunctions associated with the ground state. One important aspect of ψ_0 is that it is written in the spin basis, as, $\psi_0 = (\pi a^3)^{1/2} e^{r/a}|s\rangle$, where $a \approx 0.5$ Å is the Bohr radius. Plugging these terms in Equation 1.12, the integration over θ results in 0 for the first term in Equation 1.11, yielding

$$E = -\frac{2}{3}\frac{\mu_0}{\pi a^3}(\mathbf{m_p} \cdot \mathbf{m_e}). \tag{1.13}$$

Equation 1.13 is almost in the final form for evaluating the energy transition. The step we need to take now is to relate $\mathbf{m_p}$ and $\mathbf{m_e}$ which can be written as a function of their respective spins, and gyromagnetic ratios γ, yielding

$$E = \frac{2}{3}\frac{\mu_0}{4\pi a^3}\gamma_e\gamma_p\mathbf{S_p}\mathbf{S_e}, \tag{1.14}$$

where $\mathbf{S_i}$ represents the spins for the respective particles. With this interaction, $\mathbf{S_p}$ and $\mathbf{S_e}$ are no longer independently conserved, and the quantum numbers for the system are the eigenvalues of the total angular momentum. The product $\mathbf{S_p}\mathbf{S_e}$ yields two states: a singlet and a triplet, with different eigenvalues. The singlet state presents two antiparallel spins, and the triplet state presents two aligned spins; the transition is depicted in Figure 1.2. We also know that the gyromagnetic ration is related to the mass, proton charge q and g of the i^{th} particle as $\gamma = (q/2m_i)g_i$. Therefore, we can calculate the energy gap between the singlet and triplet states as

$$E_{gap} = \frac{2}{3}\frac{\mu_0\hbar^2\gamma_e\gamma_p}{\pi a^3} = 5.88 \times 10^{-6}\ \text{eV}. \tag{1.15}$$

The equivalent electromagnetic frequency is ~1420 MHz, which corresponds to a wavelength of 21 cm.

1.3 Theory behind the 21-cm global signal

1.3.1 Radiative Transfer equation

Photons from the CMB interact with the neutral hydrogen, and introduce features in the very low-frequency range of the CMB, which is well fitted blackbody radiation spectrum [Fixsen et al., 1996]. These features arise from neutral hydrogen spin transitions between the ground and first excited states. In order to quantify how many particles are there in the excited state (with n_1) compared to the ground state (with n_0), we define the spin temperature T_S via the relation [Furlanetto et al., 2006],

$$\frac{n_1}{n_0} = \frac{g_1}{g_0}e^{(-T_*/T_s)} = 3e^{(-T_*/T_s)}, \tag{1.16}$$

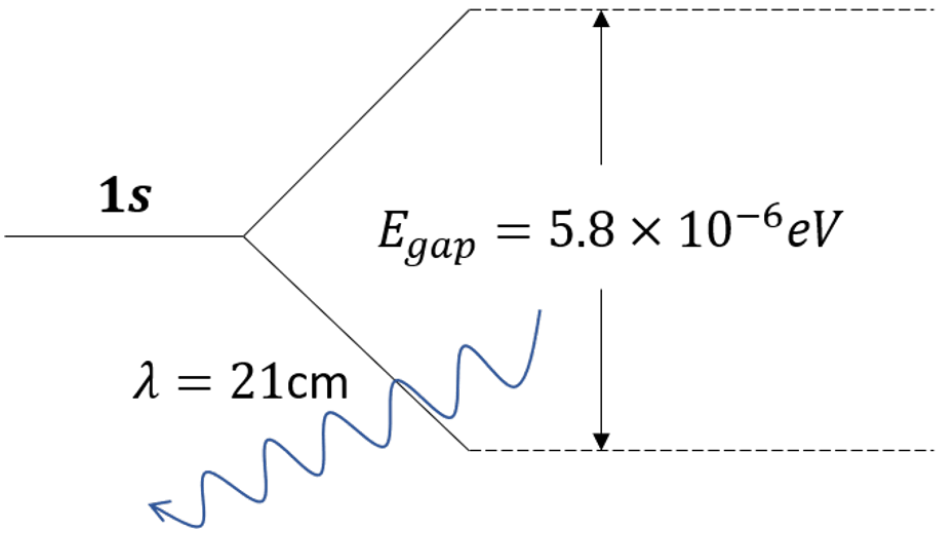

Figure 1.2: Depiction of the hyperfine splitting in the ground state of hydrogen. The transition between a state with parallel spin to antiparallel spin occurs, releasing radiation with $\nu = 1420\,\text{MHz}$, or $\lambda = 21$ cm. The four ground states related to the proton and electron spin states, are separated by this small energy gap that enables the transition.

where $T_* \equiv hc/\lambda_{21cm} = E_{pot}/k_B = 0.068\text{K}$. Further, we will consider the physical interaction with clouds of hydrogen and thus apply the principles of radiation transfer in order to reach a final form for the spin temperature as a function of redshift. We start by assuming that the background temperature T_γ has a blackbody distribution with intensity

$$I_\nu = \frac{2h\nu^3}{c^2}\frac{1}{e^{h\nu/k_B T_\gamma} - 1}, \tag{1.17}$$

where c is the speed of light, h is Planck's constant, and ν is the frequency. We can also define S_ν, a source function, as a blackbody with

$$S_\nu = \frac{2h\nu^3}{c^2}\frac{1}{e^{T_*/T_s} - 1}. \tag{1.18}$$

It is then possible to write a radiative transfer equation as

$$\frac{dI_\nu}{d\tau_\nu} = -I_\nu + S_\nu, \tag{1.19}$$

where τ_ν represents the optical depth, a quantity that defines the transparency of the medium to such radiations at given frequencies. For low frequencies, the expression for $S_\nu(T)$ can be expanded resulting in $T_b \approx \frac{I_\nu c^2}{2k_B\nu^2}$, and this is known as the Rayleigh-Jeans limit. In this case, for both T_γ and

T_s, we have

$$I_\nu = \frac{2k_B}{\lambda_{21cm}^2} T_b \tag{1.20}$$

$$S_\nu = \frac{2h\nu^3}{c^2}\frac{T_s}{T_*} = \frac{2kT_s}{\lambda_{21cm}^2}, \tag{1.21}$$

where λ_{21cm} represents the emission wavelength. These equations allow us to rewrite the transfer equation in terms of temperature brightness T_b, and the background temperature T_γ,

$$\frac{dT_b}{d\tau_\nu(\nu)} = -T_b + T_s. \tag{1.22}$$

To solve this equation, we take the limit when $\tau = 0$. In this scenario, we get $T_\gamma = T_{CMB}$. Solving this radiative transfer equation, we get

$$T_b(\nu) = T_S(1 - e^{-\tau_\nu}) + T_{CMB}(\nu)e^{-\tau_\nu}. \tag{1.23}$$

In the context of 21–cm global signal detection, the quantity of interest is the *differential brightness temperature*, the difference between the brightness temperature and the temperature of the CMB and takes into account the redshift z. This relation is expressed as

$$\delta T_b = \frac{T_b(z) - T_{CMB}}{(1+z)} = \frac{T_S - T_{CMB}(z)}{(1+z)}(1 - e^{-\nu}) \approx \frac{T_S - T_{CMB}(z)}{(1+z)}\tau_\nu. \tag{1.24}$$

When $T_S = T_{CMB}$, we have a perfect balance between emission and absorption for all frequencies [Wiklind et al., 2012]. We can write the differential optical depth $d\tau$ as

$$d\tau = \int dl\phi(\nu)n_0\sigma_{01}(1 - e^{-E_{10}/k_BT_S}) \approx \frac{3c^2A_{10}}{32\pi\nu^2}\left(\frac{h\nu}{k_BT_s}\right)\left(\frac{N_{HI}}{4}\phi(\nu)\right), \tag{1.25}$$

where A_{10} is Einstein's coefficient for the 21-cm line. Now, $\phi(\nu)$ can be rewritten as a function of redshift and $N_{HI} = x_{HI}n_H$, where n_H is the number density of hydrogen atoms, and x_{HI} the neutral fraction of those atoms. This yields [Breysse et al., 2018]

$$\tau_\nu = \frac{3c^2A_{10}}{32\pi\nu^2}\left(\frac{h\nu}{k_BT_s}\right)\frac{x_{NI}n_H}{(1+z)(dv_\parallel/dr_\parallel)}, \tag{1.26}$$

where the term $dv_{\parallel}/dr_{\parallel}$ corresponds to the acceleration of gas along the line of sight. In cosmological terms, δT_b becomes

$$\delta T_b = 27 x_{HI}(1+\delta_B)\left(\frac{\Omega_B h^2}{0.023}\right)\sqrt{\frac{0.15}{\Omega_m h^2}\frac{1+z}{10}}\left(1-\frac{T_\gamma}{T_S}\right) mK, \tag{1.27}$$

where x_{HI} is the neutral density and δ_B the density contrast of hydrogen gas.

1.3.2 Parameters that affect spin temperature

In Figure 1.4, shows the evolution of the 21–cm global signal through cosmic history, as a function of frequency and redshift, as well as a time evolution ever since the Big Bang. There are three processes that influence the number of particles in the ground and excited states (i.e., change T_s): radiative coupling with the CMB, coupling to Ly-α photon, and collisions caused by the gas kinetic temperature. In Figure 1.3, we present a scheme of the three processes.

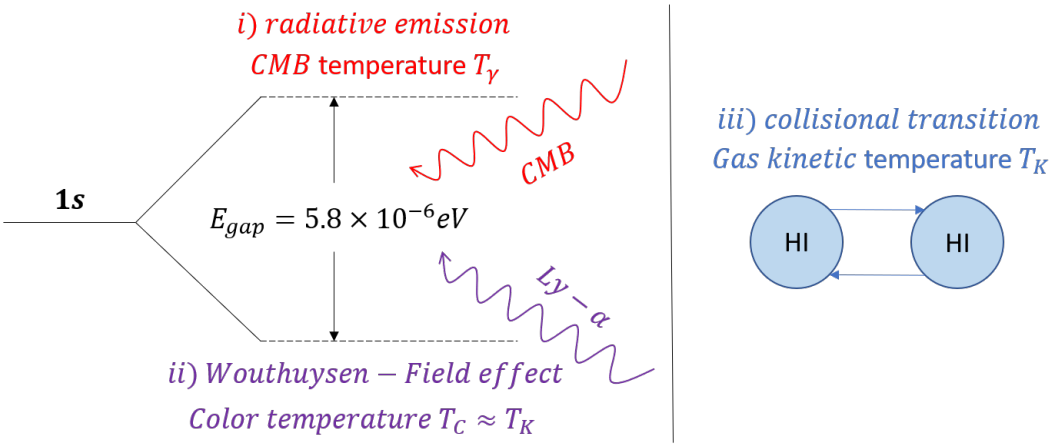

Figure 1.3: The three mechanisms that affect the spin temperature T_s: i) radiative emission, which brings T_s close to T_γ, ii) Wouthuysen-Field effect, which brings T_s to T_c, and iii) collisional transition, which brings T_s to T_K.

The way we can express the dynamics of these three processes acting on T_s is by writing a rate equation [Rybicki and Lightman, 2008]

$$\dot{n_0} = -n_0[P^\gamma_{01} + P^c_{01} + P^\alpha_{01}] + n_1[P^\gamma_{10} + P^c_{10} + P^\alpha_{10}], \tag{1.28}$$

where n_0 quantifies the number of particles in the ground state, n_1 quantifies the number of particles in the first excited state. P_{01} and P_{10} represents the excitation and de-excitation probabilities for each of the three processes, respectively.

Each of the processes can be dominant at a given time in cosmic history. In order to write out a detailed balance equation for each epoch, we consider that during each dominant phase, the dominant process maintains thermodynamic equilibrium with the spin temperature T_s, by the first law of thermodynamics. When there is equilibrium between any of the processes and T_s, there are no emissions, a fact that in Equation 1.28, is translated into no temporal change of states, i.e., $\dot{n_0} = 0$. When the spin temperature achieves equilibrium with T_γ, Equation 1.28 can be written as

$$n_0 P_{01}^{\gamma} = n_1 P_{10}^{\gamma} \rightarrow \frac{n_0 P_{01}^{\gamma}}{n_1 P_{10}^{\gamma}} = \frac{n_1}{n_0} = 3e^{-T_*/T_\gamma} \approx 3\left(1 - \frac{T_*}{T_\gamma}\right). \tag{1.29}$$

Analogously, if collisions or Ly-α dominate, Equation 1.28 can be written as either

$$\frac{n_1 P_{10}^{c}}{n_1 P_{10}^{c}} = \frac{n_1}{n_0} = 3e^{-T_*/T_s} \approx 3\left(1 - \frac{T_*}{T_K}\right), \tag{1.30}$$

or

$$\frac{n_1 P_{10}^{\alpha}}{n_1 P_{10}^{\alpha}} = \frac{n_1}{n_0} = 3e^{-T_*/T_s} \approx 3\left(1 - \frac{T_*}{T_\alpha}\right), \tag{1.31}$$

respectively. If all three processes happen simultaneously, we consider the same detailed balance equation, comparing the ground and the excited states in equilibrium,

$$n_0[P_{01}^{\gamma} + P_{01}^{c} + P_{01}^{\alpha}] = n_1[P_{10}^{\gamma} + P_{10}^{c} + P_{10}^{\alpha}]. \tag{1.32}$$

The spin temperature can be therefore written as [Breysse et al., 2018, Pritchard and Loeb, 2012],

$$T_s^{-1} = \frac{T_\gamma^{-1} + x_c T_K^{-1} + x_\alpha T_c^{-1}}{1 + x_c + x_\alpha}, \tag{1.33}$$

where $x_c = \frac{P_{10}^{c}}{P_{10}^{\gamma}}$ and $x_\alpha = \frac{P_{10}^{\alpha}}{P_{10}^{\gamma}}$ are the coupling coefficients from collisions and Ly-α emissions, respectively. x_c is calculated considering the scattering rate between hydrogen atoms, the scattering rate of electrons in hydrogen atoms, and the scattering rate of protons and hydrogen atoms, that are calculated using quantum mechanics. x_α is obtained considering the flux of Ly-α radiation produced, and its scattering rate by hydrogen atoms.

1.4 Cosmic history and the 21–cm global signal

- ($1100 \gtrsim z \gtrsim 200$): At very early times, T_K and T_γ are locked together, so $\delta T_b = 0$. The electrons drive T_K to T_{CMB}, and therefore $T_b = T_{CMB}$. The major physical process involved at these times is the Compton scattering by of electrons by photons.

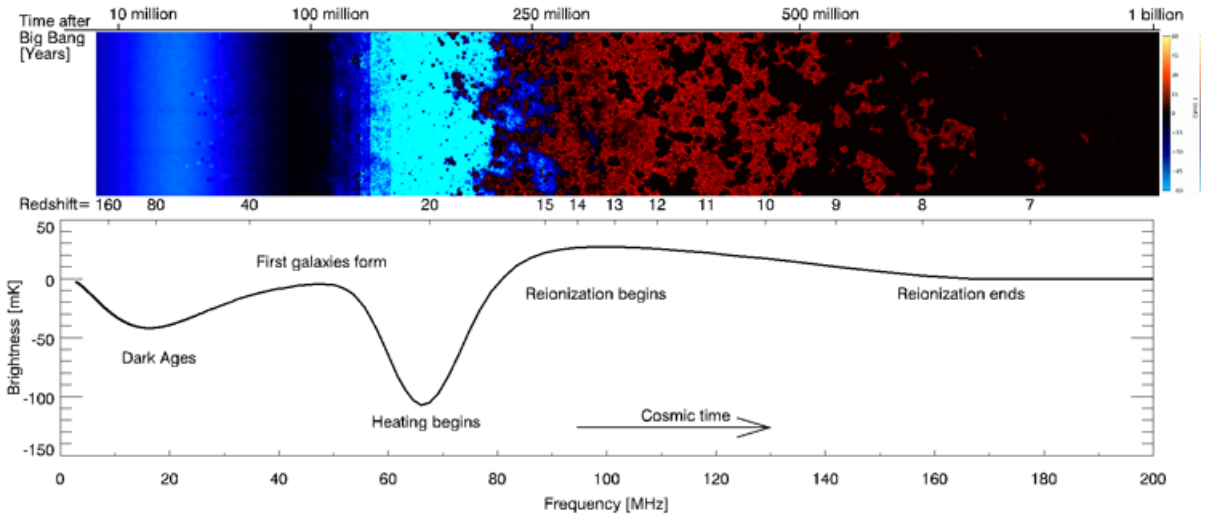

Figure 1.4: Top: Spatial structure of the universe as a function of time since the Big Bang. Bottom: Evolution of brightness temperature δT_b through cosmic history, as a function of frequency and redshift. Figure taken from [Pritchard and Loeb, 2012].

- $(200 \gtrsim z \gtrsim 30)$: This is the epoch known as the Dark Ages. As the universe expands, the temperature of the gas, T_K, drops faster than T_{CMB}. T_K and T_s are in equilibrium. The collisional coupling keeps T_s lower than T_{CMB}, and therefore we can observe an absorption of 21–cm radiation. At about $z \sim 80$, after the universe has expanded even more, the gas is too dilute and has few residual free electrons to maintain the equilibrium between T_K and T_s, bringing T_s back to T_{CMB} at $z \sim 80$ [Miralda-Escudé, 2003].

- $(30 \gtrsim z \gtrsim 15)$: This is the epoch known as the Cosmic Dawn when the first stars and galaxies in the universe were born. The appearance of these stars creates Ly-α photons, which can cause changes in the occupancy states of neutral hydrogen, via Wouthuysen-Field effect [Wouthuysen, 1952, Field, 1958]. During this time, $T_s = T_K$, and $T_K < T_{CMB}$, therefore reflecting an absorption feature in T_b. At later times, $(z \sim 20)$ active galactic nuclei (AGNs) produce X-rays that increase T_K. As T_K is still coupled to T_s, T_b is seen in emission.

- $(15 \gtrsim z \gtrsim 6)$: Epoch when the EoR starts, when neutral hydrogen vanishes. This happens due to the continous emission of UV photons in the IGM. After the EoR, the global signal ceases to exist, as neutral hydrogen atoms have been ionized.

1.5 Experiments to detect the redshifted 21–cm global signal

The brightness temperature described in Equation 1.27, can be detected as a sky-averaged global signal or via spatial fluctuations, as seen in the top panel of Figure 1.4. Examples of 21–cm global signalsingle antenna experiments are Mapper of the IGM Spin Temperature (MIST), Probing Radio Intensity at high-Z (PRIZM) [Philip et al., 2019], Large Aperture Experiment to Detect the Dark Ages (LEDA) [Price et al., 2018], Shaped Antenna measurement of background Radio Spectrum (SARAS-2 [Singh et al., 2018], and SARAS-3 [Nambissan et al., 2021]), Broadband Instrument for Global HydrOgen ReioNization Signal (BIGHORNS) [Sokolowski et al., 2015], Sonda Cosmológica de las Islas para la Detección de Hidrógeno Neutro (SCI-HI) [Voytek et al., 2014], Cosmic Twilight Polarimeter (CTP) [Nhan et al., 2018] and the Radio Experiment for the Analysis of Cosmic Hydrogen (REACH) [de Lera Acedo, 2019]. In table 1.1, some of the current experiments are presented, along with their location, operating frequencies, and antenna designs.

Multi-antenna experiments which try to make a 3D map using the 21–cm transition provide a spatial view of the early universe, such as Experiments such as Murchison Widefield Array (MWA), the Giant Metrewave Radio Telescope (GMRT) [Paciga et al., 2011], the Low Frequency Array (LOFAR) [van Haarlem et al., 2013], the Hydrogen Epoch of Reionization Array (HERA) [DeBoer et al., 2017], Long Wavelength Array (LWA) [Ellingson et al., 2009] and the Square Kilometre Array (SKA) [Klöckner et al., 2013].

The only reported experimental result that can be interpreted as the 21–cm global signal from Cosmic Dawn was done by the Experiment to Detect the Global EoR Signature (EDGES) [Bowman et al., 2018], located in the Murchinson Radioastronomy Observatory (MRO), in Western Australia, a radio quiet site. The experiment consists of three different instruments. The high-band one covers $90 - 200$ MHz ($14 < z < 6$), the mid-band covers $60 - 160$ MHz ($32 < z < 8$), and the low-band operates in the range $50 - 100$ MHz ($27 < z < 13$). The detection was successful in the low-band instrument, which consisted in a blade dipole antenna over a ground plane. The results show an absorption feature centered at 78 ± 1 MHz, and an amplitude of $0.5^{+0.5}_{-0.2}$ K, which is is approximately twice the theoretical value expected. The EDGES team went over a series of tests on the field, and confirmed with different instruments at the same site. Similar results were obtained even after several hardware modifications, with sky data that expanded over two years [Monsalve et al., 2019]. A summary of the detection is presented in Figure 1.5.

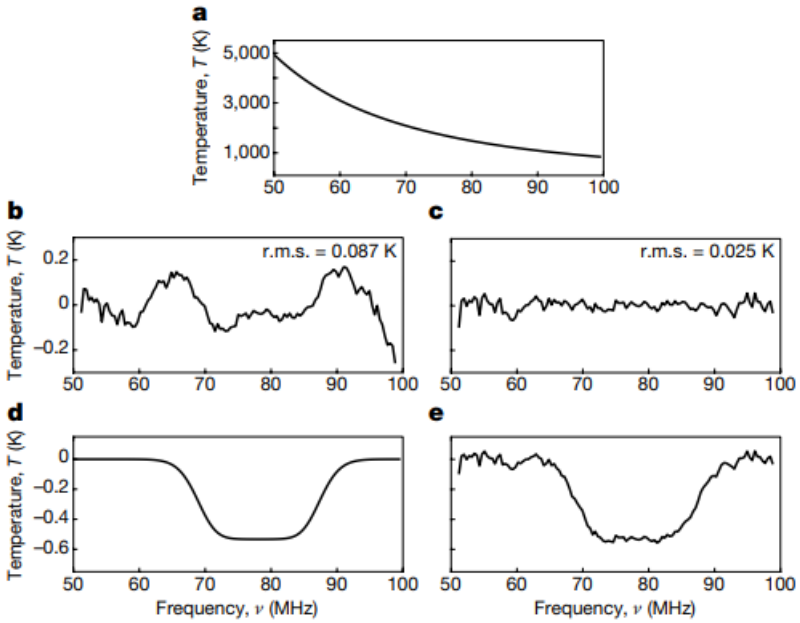

Figure 1.5: Summary of the detection made by EDGES. In a) the sky temperature as a function of frequency, dominated by Galactic synchrotron emission. In b), residuals after removing only the foreground model, and in c) after removing foreground and 21–cm models. In d) and e), the recovered 21–cm absorption feature, and the sum with the residuals from c), respectively. Figure taken from [Bowman et al., 2018]

Experiment	Location	Frequency [MHz]	Antenna design
EDGES	Western Australia	50-200	Blade dipole above GP
CTP	Virginia, USA	60-120	Dual-polarization dipole
PRIZM	Marion Island, South Africa	30-200	Four-square dual dipole
REACH	Karoo desert, South Africa	50-170	Wideband dipole/spiral
SARAS-3	Southern India	40-200	Monopole cone-disk
MIST	Atacama Desert	40-120	Blade dipole above soil
mini–MIST	MARS	40-120	Blade dipole above soil

Table 1.1: Some of the 21–cm current global signal experiments to detect signals from the Cosmic Dawn, locations, frequency of operation, and antenna design.

The EDGES team proposed an explanation for these result: a primordial gas colder than expected as a result of the interaction between dark matter and baryons, or the necessity for new physics to explain the divergence. According to the signal, Lyman-α photons were emitted 180 million years after the Big Bang, and was heated approximately 100 million years later [Bowman et al., 2018]. Multiple studies have been performed over the last few years proposing novel explanations for the difference in amplitude, from a theoretical perspective. Some propose that the detections from the Cosmic Dawn might also enlighten the mysteries of the presence of dark matter due to the interaction with the gas in the IGM [Fialkov et al., 2018]. Scattering with dark matter can happen via an excess radio background [Fialkov and Barkana, 2019] can also induce the shape of the amplitude of the brightness temperature, saturating the 21–cm global signal above the temperature of the CMB at a consistent redshift with the absorption feature detected by the EDGES experiment. New experiments will help confirm the EDGES detection and provide a better understanding of the physics of the early universe.

1.6 Thesis outline

The focus of this thesis is Mapper of the IGM Spin Temperature (MIST), and Mini-MIST, a more portable version of the instrument. Both 21–cm global signal experiments with the ultimate goal of detecting the absorption feature from the Cosmic Dawn epoch of the universe. In Chapter 2, I summarize the design drivers and overall architecture of MIST and Mini-MIST. In Chapter 3, I describe my work on the development of the MIST antenna, including simulations for optimizing the geometry, prototype construction, and preliminary test results. In Chapter 4, I describe the design and testing of a device to measure soil electromagnetic properties, which have important impacts on the MIST antenna performance. In Chapter 5, I present the perspectives for future work in MIST and Mini-MIST.

Chapter 2

The MIST and Mini-MIST experiments

> "(Emília) – A vida, senhor Visconde, é um pisca-pisca. A gente nasce, isto é, começa a piscar. Quem pára de piscar chegou ao fim, morreu. Piscar é abrir e fechar os olhos – viver é isso".
>
> Monteiro Lobato

The Mapper of the IGM Spin Temperature (MIST) is an experiment to measure the redshifted 21-cm global signal from neutral hydrogen from the Cosmic Dawn. MIST will be located in Northern Chile, in the Atacama Desert, and will experiment will operate in a frequency band of 40 – 120 MHz band, using a blade dipole antenna that sits directly above the ground, without an additional electromagnetic ground plane. Mini-MIST will be located at the McGill Arctic Research Station (MARS), and is a more portable version of the MIST instrument, with the primary differences being in the back-end hardware used for data acquisition. The MIST and Mini-MIST instruments are being developed by a collaboration between McGill University, Universidade Católica de la Santísima Concepción, Universidad de Chile, and the National Radio Astronomy Observatory (NRAO).

In this chapter, I will highlight some of the challenges faced in 21-cm global signal detection, which motivates the remote locations to perform the experiments, and instrument design choices. I will also describe the full signal chain, from the detection and conditioning of the signal at the front end, to the digitization and analysis at the back-end.

2.1 Challenges in the 21-cm global signal detection

The detection of the global 21-cm signature requires a measurement of total power, and the instrument is therefore highly sensitive to: RFI contamination, strong Galactic foreground emissions from the Milky Way ($\sim 10^3$ K), ionospheric effects, and instrumental systematics. A successful detection relies on careful antenna design and calibration procedures such as the ones presented in [Rogers and Bowman, 2012] and [Monsalve et al., 2017a]. I will briefly go over some of these aspects over the following subsections.

2.1.1 Radiometer equation

The spectrum of an emitting source was presented in Equation 1.18, using the approximation of a blackbody spectrum. The received power P by an antenna detecting this source can be obtained by integrating the source function over a solid angle, and over the area of the antenna, yielding

$$P = k_B \, \Delta\nu \, T_{src}, \tag{2.1}$$

where T_{src} represents the temperature of the source, $\Delta\nu$ the bandwidth, and k_B is Boltzmann's constant. Generally speaking, this equation applies to any noise temperature, such as the temperature measured by the antenna T_{ant}, and the noise temperature of the receiver T_{rx} The system noise temperature T_{sys}, can be written as

$$T_{sys} = T_{ant} + T_{rx}. \tag{2.2}$$

The temperature of the signal is lower than T_{sys}, so in this case, it is necessary to attenuate the statistical errors in order to perform a detection. The RMS uncertainty σ_T for a single noise measurement is given by

$$\sigma_T = \frac{T_{sys}}{\sqrt{\Delta\nu \, \tau}}, \tag{2.3}$$

where τ is the integration time. Solving for integration time, Equation 2.3 yields

$$\tau = \frac{T_{sys}^2}{\sigma_T^2 \, \Delta\nu}. \tag{2.4}$$

For 21-cm experiments, we can make an order-of magnitude estimation for how much integration time is needed to measure the cosmic dawn feature with a signal-to-noise ratio of ~ 1. $T_{sys} \sim 10^4$ K (set by Galactic synchrotron emissions), observing at a bandwidth of $\Delta\nu = 1$ MHz (to give enough frequency resolution over the width of the absorption feature), the time required for a sensitivity of 100 mK is $\tau \sim 3$ h. This does not account for systematic effects that do not integrate down with time. Among systematic effects we can include impedance mismatches, noise

from the receiver and RFI, or anything that can introduce spurious spectral structure. This is why a careful characterization of all components of the instrument is necessary for a successful 21-cm global signal detection.

2.1.2 Foreground emission

One of the greatest challenges to overcome in a 21-cm global signal experiment is the presence of a strong foreground radiation at the frequencies of interest. These foreground fluctuations are non-uniform across the sky, as we can see in Figure 2.1. The strip at the center represents the synchrotron emissions from the Milky Way, which dominate the sky at lower frequencies. At higher frequencies, synchrotron emissions no longer dominate, and experience a drop as a function of frequency.

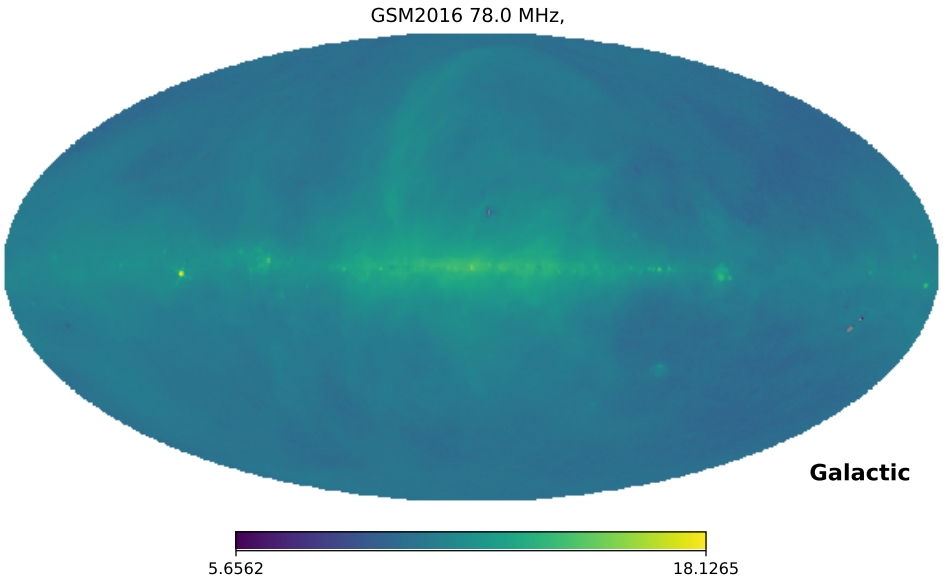

Figure 2.1: Galactic and extragalactic sky emissions at $\nu = 78$ MHz. Plot made using PyGSM 2016 [Zheng et al., 2017].

2.1.3 Radio-frequency interference (RFI)

Radio-frequency interference (RFI) can be orders of magnitude higher even than foreground emissions. This is due to the large number of broadcasting sources that operate transmitting over the bandwidth that overlaps with the one of the 21-cm global signal experiments ($50 < \nu < 100$ MHz), such as radios, satellites, transmission lines and TV stations. Self-generated RFI from the front-

and back-end electronics in a global signal experiment can also introduce spurious spectral features that need to be mitigated and characterized.

RFI spectral features can be constant as a function of time, or time-varying, depending on the source. When assessing a candidate observing site for a global signal experiment, the RFI environment needs to be surveyed to characterize these features. In RFI surveys, it is possible to identify the main spectral features and characterize them for further extraction in data analysis using proper algorithms to flag the interference that range from Principal Component Analysis (PCA) to machine learning techniques [Liu and Shaw, 2020].

2.2 MARI site and RFI survey

Figure 2.2: Location of the MARI site, marked with an X on the map. The site is located 135 Km east of San Pedro de Atacama, at 1 hour 40 minute drive from San Pedro de Atacama, in Northern Chile. Picture ceded by Ricardo Bustos.

MIST will be located in the Atacama Desert, in Chile, at the Medidor Autónomo de Radio Interferencia (MARI) site (Latitude:23° 09' 25.7" S; Longitude: 67° 13' 53.4" W; Altitude: 4380 masl), chosen after an RFI survey. The MARI site is a radio quiet site located 135 km east of San Pedro de Atacama, a 1 hour 40 minute drive from San Pedro de Atacama. The site is 60 km east of the Chajnantor area, where the Atacama Large Millimeter Array (ALMA) [Otárola et al., 2014] is located.

The MARI radio survey was made during 2015-2018 to characterize the region in terms of RFI and environmental conditions. Data were obtained in May, July, and November, except for periods when the weather was bad. Figure 2.3 shows the raw waterfall plot for different frequency

channels, and for the three months of observation, with antenna temperature being the color scale. In these plots, x corresponds to the frequency, y corresponds to date, and the color scale represents the antenna temperature, in K. The main feature in these waterfall plots is the diurnal motion of the Galaxy. During Galactic transit, we see the highest values for antenna temperature. When the Galactic center is below the horizon, the antenna temperature decreases significantly.

Figure 2.4 shows the averaged antenna temperature as a function of frequency, which dominated at lower frequencies by Galactic synchrotron emissions. There are not any strong, persistent features from FM the high 100 MHz band, for three different observation months. The occupancy per channel is low for low-frequencies, where the 21-cm global signal is contained, indicating that MARI site is a competitive site to perform cosmological observations from the early universe. It is also a site that offers operational advantages, as, logistically, it can be accessed from direct roads. Usually, there is a trade-off between accessibility and RF-quietness; although there are some sites that are more RF-quiet than MARI, they are typically more difficult to access.

2.3 MARS site and RFI survey

The McGill Arctic Research Station (MARS), in Figure 2.5, is located in the high-Arctic (79°26'N 90°46'W) at the Axel Heiberg Island, and is the site where the Mini-MIST instrument will be deployed during the summer of 2022. The site is 120 km from Eureka, the nearest persistent radio transmitters that could interfere in low-frequency measurements. Other transmitters are located farther, such as Grise Fjord (360 km), Resolute Bay (540 km), and Alert (590 km). Being at a high latitude, MARS is also favorable in terms of atmospheric conditions, as the ionosphere is weakly ionized during the Arctic winter [Dyson et al., 2020].

The survey in MARS was made by a single pathfinder antenna station that was developed for the Array of Long Baseline Antennas for Taking Radio Observations from the Sub-Antarctic [Chiang et al., 2020]. RFI was measured in 6 different sites across MARS from July 9-21, 2019, generating over 106 h of data. These measurements are summarized in Figure 2.6. In the frequency range of 10-20 MHz, high RFI occupies over 35% of the channels, which were ignored in the overall occupancy calculation. The occupancy in the 0-120 MHz frequency range was 1.6% for east-west polarized data, and about 2.0% for north-south polarized data. Overall, these results show another competitive site for making cosmological observations in the search for the 21-cm global signal, as the frequencies within the 20-90 MHz band show with low mean occupancy, of less than 5 %.

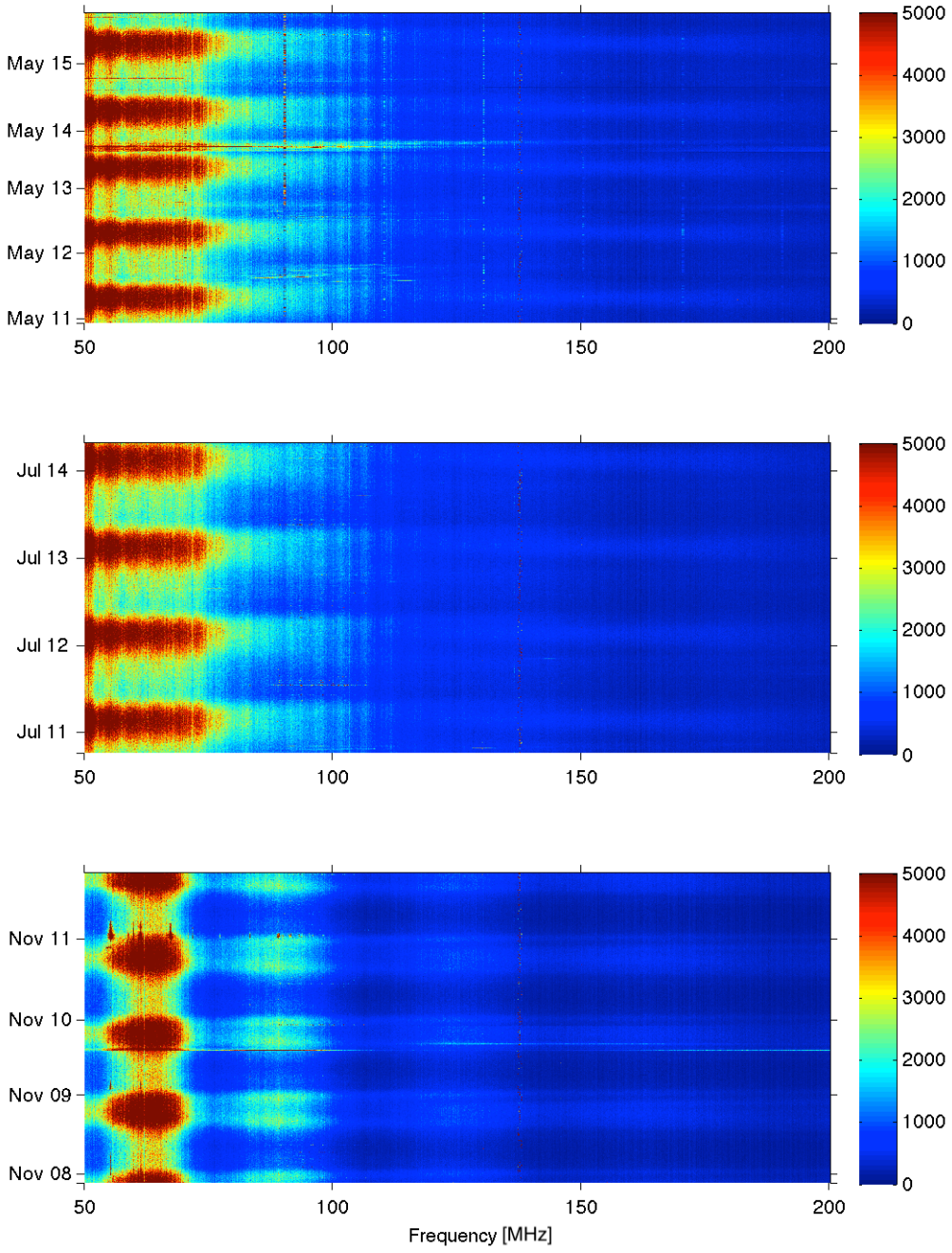

Figure 2.3: Waterfall plots for the antenna temperature (color scale, in K) at different dates, for the three months when observations were made. Picture ceded by Ricardo Bustos.

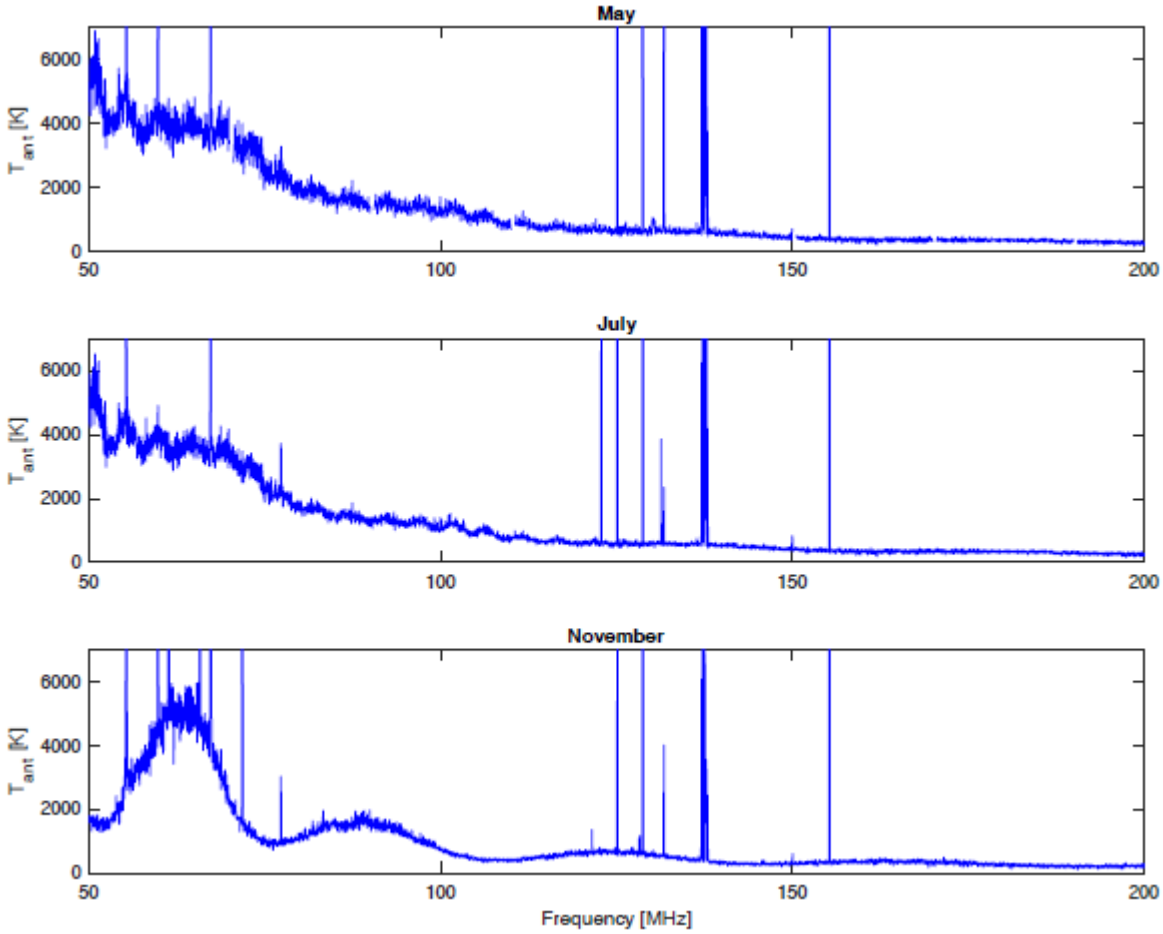

Figure 2.4: Antenna temperature as a function of frequency for three observation months: May, July, and November. The low-frequency end is dominated by galactic emissions, bringing the antenna temperature to the order of 10^3 K. The occupancy level for the low-frequency end is small, indicating MARI as a competitive observation site to perform observations. Picture ceded by Ricardo Bustos.

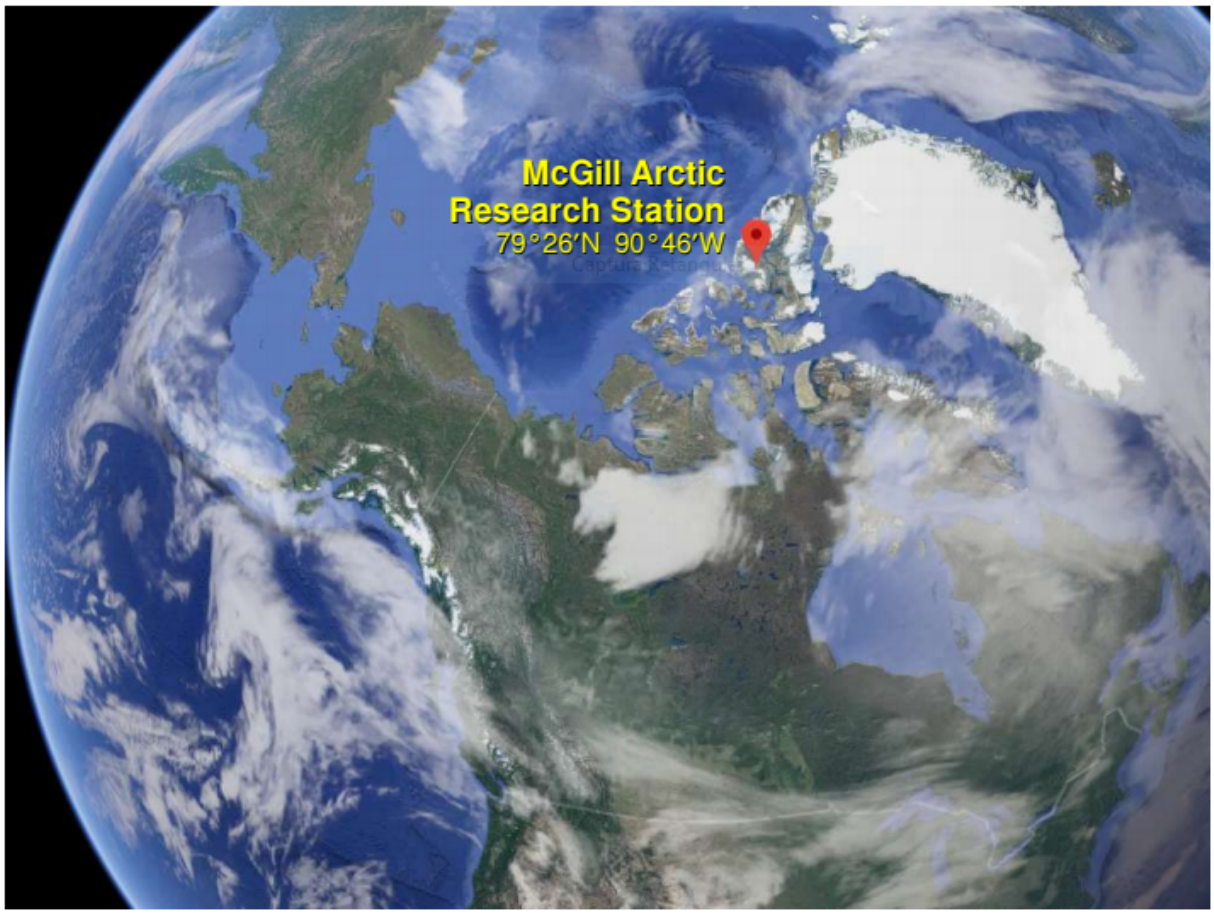

Figure 2.5: A view of the McGill Arctic Research Station(MARS), located at 79°26'N 90°46'W, on the Axel Heiberg Island, in the high Arctic. Picture taken from Tankiso Moso's MSc. thesis.

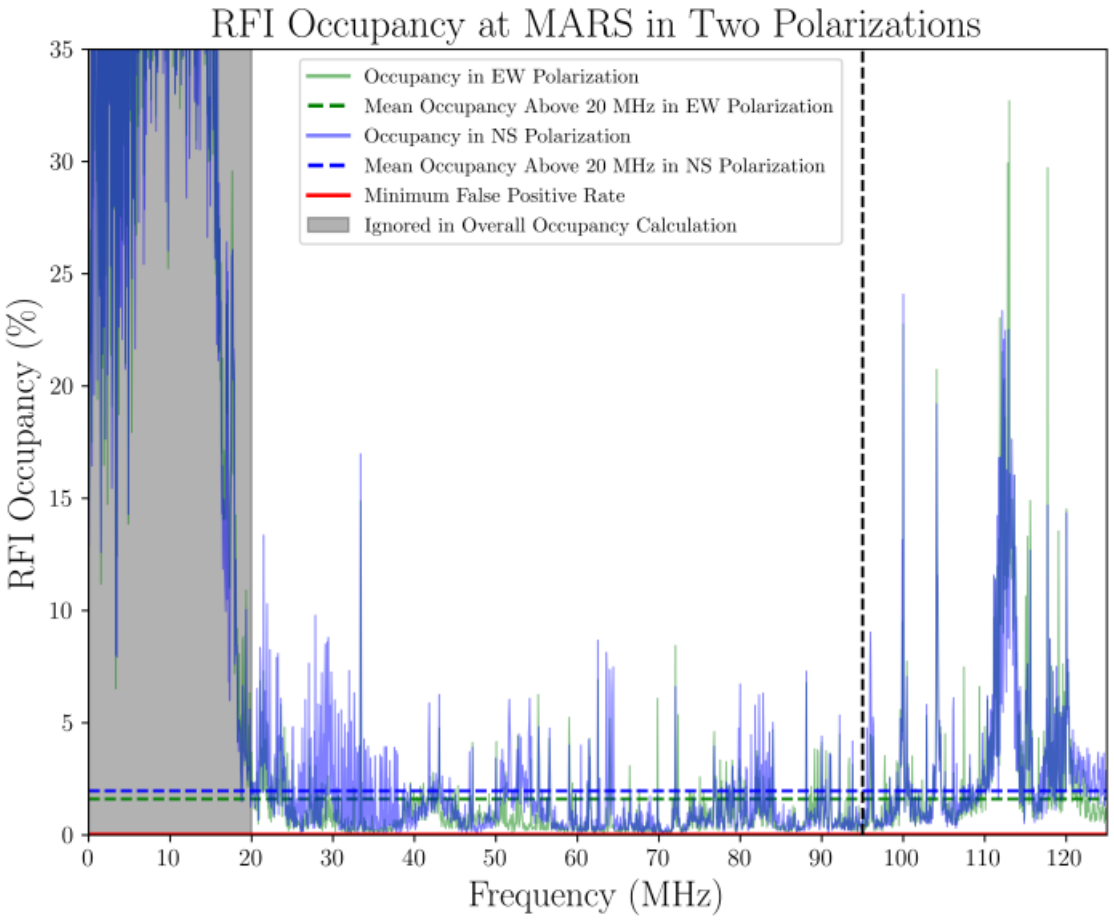

Figure 2.6: RFI occupancy levels in the 0-120 MHz band. Up to 20 MHz, the data was ignored for the calculation of the overall RFI occupancy, since at this frequency range RFI represented over than 35% of those frequencies. For frequencies higher than 20 MHz, we see a low occupancy with RFI mean of less than 5 % in NS polarization, indicating a competitive site for cosmological observations of the 21-cm global signal. Picture taken from [Dyson et al., 2020].

2.4 MIST and Mini-MIST instruments

The designs of MIST and Mini-MIST were driven by the minimization of instrumental systematics and the ability to perform in-situ calibrations. Each instrument will make use of the same calibration scheme used by EDGES [Bowman et al., 2018], but have differences in the antenna design that will be explored in Chapter 3, and in the components used for front-end and back-end electronics, since Mini-MIST is a smaller, and more portable version of the MIST instrument. The complete block diagram for Mini-MIST is presented, and briefly discussed. The calibration procedures are also explained, highlighting important details that will guide the efforts made in antenna design.

2.4.1 Front end and back end

The instruments are divided into two parts: the front end, and the back end. On the front end, antenna receives, conditions, and amplifies the signal. On the back end, the processing continues, and signal is digitized before being stored in a PC. Back-end electronics need to be physically isolated from the front end so that they can be shielded, thus reducing contamination from self-generated RFI.

Both MIST and Mini-MIST instruments were designed to operate in extreme environmental conditions, where the ambient temperature can change significantly across a day, or over an observation season. In MARS, it will be remotely monitored while performing measurements during the Arctic winter. The instrument's components were chosen to compose the system to operate efficiently over these conditions considering power consumption and overall functioning.

In comparison to MIST, Mini-MIST has the additional requirement of being easy to assemble and transport. Mini-MIST is therefore:

- 43% smaller than MIST compared in terms of area covered by the panels;
- Low weight, and has modular electronics;
- Low power, and with efficient use.

The overall scheme for Mini-MIST is presented in Figure 2.7, in more detail. The first step in the signal chain the detection of the signal by the antenna, which happens at the input, and proceeds to the front end, which contains the most sensitive components. Then, the signal passes through a switch board, goes through low noise amplifiers (LNAs) which amplify the signal, a 25 MHz high pass filter, attenuators, and another low pass filter of 150 MHz. The filters are used to restrict the frequencies of interest for our experiment, and the attenuators help in the impedance matching of the system.

In the back end, the signal passes through a 400 MS/s analog-to-digital converter (ADC) that samples with 14 bit associated with a field-programmable gate array (FPGA), where the signal is digitized before being sent to a PC. On the PC, the Fourier Transforms are performed to obtain spectra using a 4-tap polyphase filter bank (PFB) method programmed on the GPU, in CUDA C++. The purpose of applying this method is to diminish spectral leakage in the spectra which can contaminate measured data.The overall scheme for Mini-MIST is presented in Figure 2.7, in more detail.

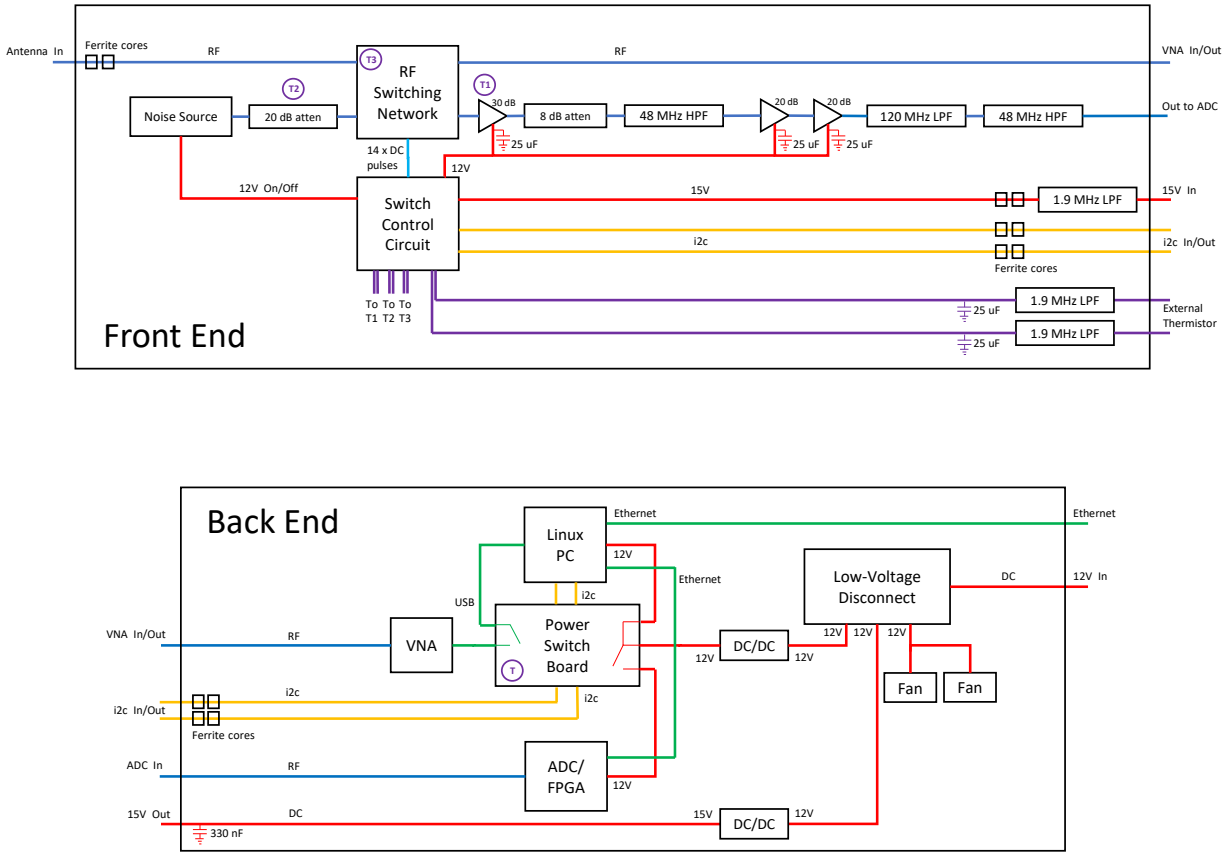

Figure 2.7: Front-end and back-end parts for Mini-MIST. They are isolated in order to reduce RFI contamination. The front end contains the more sensitive components: attenuators, high pass filters, and the switch board that continously controls the system's calibration while taking observations with the antenna. The back end of the instrument is responsible for digitizing, computing the spectra, and storing the signal.

The instrument undergoes continuous calibration while taking sky data, and the radio frequency (RF) switch board controlled by the circuit is the responsible for managing all steps necessary for

the calibration process, directing the signal towards different electrical paths it can take. The exact calibration scheme for MIST and mini-MIST has not yet been determined. Here, I briefly describe some of the options for calibration, according to the literature of previous experiments.

During measurements, the control circuit converts the signal into an I2C format into control voltages that then are sent to the switches. For the calibration, the switch board gets sky data and switches cycles through three different positions to select a signal from the sky, hot load, or ambient load to send downstream. During calibration, all the reflections (S11) of the front-end components are measured using the vector network analyzer (VNA) that is in the back-end. This process happens regularly, as the impedance matching between all elements is not perfect, and it is important to account for such effects for an accurate calibration. The switch board is additionally equipped with thermometry circuitry and is connected to thermistors placed on the LNA, switch board, attenuators, and amplifiers. The thermistors are represented in Figure 2.7 as purple circles.

2.4.2 Calibration procedures

A careful characterization of the instrument is essential for a successful 21-cm redshifted global signal detection, as foregrounds can couple to instrumental systematics. MIST and Mini-MIST calibration follows the same scheme as EDGES [Monsalve et al., 2017a], which can be summarized in three different parts. The first one is converting the temperature measured by the antenna to a temperature scale. After the conversion, the second part is the removal of losses, which is followed by the third step, which consists of the compensation for beam chromaticity.

The antenna temperature, T_{ant}, can be written as [Rogers and Bowman, 2012]

$$T_{ant} = T_{sky}(1 - |\Gamma|^2) + \ldots, \tag{2.5}$$

where T_{sky} represents the sky temperature, and Γ is the return loss from the antenna. The dots in Equation 2.5 represent other terms that affect the antenna temperature, such as the additional effects of impedance mismatch, and reflections between the low-noise amplifiers (LNA) and the antenna. From this equation, we see how Γ is an important parameter for the measurements, since it affects directly the observed temperature of the sky. A high Γ indicates a greater power loss, and a subsequent T_{ant} that can largely differ from the desired T_{sky}. Therefore, minimizing Γ brings T_{sky} closer to T_{ant}, one of the desirable features of the instrument.

In the laboratory, the calibration of the instrument can happen with four different calibrators: an ambient load, a hot load, a long open cable, and an long short-circuited cable. The ambient and hot load, which have controlled temperatures of 300 K and 400 K respectively, are used to provide temperature references. Ambient and hot references are measured in terms of noise temperature, and related to the actual physical temperatures, which are measured through thermistors. Due

to impedance mismatches, open and shorted cables produce ripples in the spectrum which can be used to estimate noise wave parameters. The calibration using these elements are important to determine the conversion function of the noise temperature measured by the instrument to an antenna temperature. During such measurements, in the back-end, the reflection coefficients of the calibrators are also measured by a VNA, as they also appear in the expanded for of Equation 2.5. The VNA is also calibrated periodically, by being connected to open, short, and 50 Ω standards in the back-end.

A further test that can be done for the MIST and Mini-MIST instruments is with an external noise source at the end of a transmission line that produces a spectrum that is similar to the sky foreground. Reflections of this external noise source will mimic the ones of an antenna, therefore validating the calibration for future field measurements. The calibrated spectrum of the noise source will be fitted with a foreground model that describes the sky temperature as a function of frequency, and the residuals of this fit will be evaluated in order to verify the performance of the instrument [Bowman et al., 2018].

With the calibrated instrument, it is possible to proceed to field measurements. During regular observations, the switch will cycle through the antenna, hot load, and ambient load and compute sky spectrum, during 30 minutes. In parallel to measuring the temperature levels for the four calibrators, in the back-end, their reflection coefficients are also measured by a VNA. After these measurements occur, the switches are reconfigured to measure reflection coefficients for the LNAs, for the front-end, and for the antenna, during three minutes. The corrections in the integrated spectra happen using Equation 2.5 in its expanded form [Monsalve et al., 2017a, Rogers and Bowman, 2012].

Chapter 3

Antenna design and testing

"Uma luz azul me guia com a
firmeza e os lampejos do farol".

Tim Maia

This chapter describes the antenna design process for the MIST and Mini-MIST experiments. For MIST and Mini-MIST, our goal is to deploy the antenna over soil without a ground plane, and therefore soil characterization becomes essential for simulations, and experimental measurements on the field. To build confidence in the accuracy of our simulations, we started by exploring different EM software packages, such as FEKO, WIPL-D, and NEC, to verify the overall agreement in terms of Γ, and in terms of beam gain. These results pointed towards the utilization of FEKO for our purposes. Based on the simulations and optimizations performed using this software, we defined appropriate dimensions, and proceeded to build a prototype antenna that was tested at the McGill University campus.

3.1 The receiving antenna above soil

The blade dipole built by EDGES [Bowman et al., 2018] served as an inspiration for the design of the MIST and Mini-MIST antennas. In our case however, we do not make use of a ground plane, to avoid any sort of EM-induced spectral features that might mimic a detection of a 21-cm global signal absorption feature, as explained by [Bradley et al., 2019]; in this paper, discontinuities in the ground plane are possibly the reason for the accidental creation of a short section of a transmission line, that might cause resonating waves at specific frequencies with a given shape. This can cause a resonant patch antenna artifact, which can qualitative mimic absorption features.

One of the drawbacks of not using a ground plane is the necessity of characterizing soil EM properties, and the increase of ground loss, as the EM waves are not being reflected back by a metal surface and can propagate through soil. To solve the first problem, a device to measure EM properties of soil is necessary to, and to account for the ground loss, a longer observation time is needed. This can be explained first by looking at Equation 2.4, and noting the dependence of τ with respect to T_{sys}. T_{sys} is dominated by T_{ant}, the antenna temperature without losses, which is calculated as

$$T_{ant} = \frac{\int_{\phi=0}^{2\pi}\int_{\theta=0}^{\pi} B(\theta,\phi)T_{sky}(\theta,\phi)\sin\theta\, d\theta\, d\phi}{\int_{\phi=0}^{2\pi}\int_{\theta=0}^{\pi} B(\theta,\phi)\sin\theta\, d\theta\, d\phi}, \tag{3.1}$$

where $B(\theta,\phi)$ is the antenna beam gain, and $T_{sky}(\theta,\phi)$ is the temperature of the sky. Both terms also vary as a function of frequency, but this was omitted for the sake of notation. The antenna temperature affected by losses T_{ant}^{L} is [Monsalve et al., 2017b]

$$T_{ant}^{L} = LT_{ant} + (1-L)T_{amb}, \tag{3.2}$$

where T_{amb} is the ambient temperature, and $L = L_a L_b L_c L_g$ is a combined loss coefficient which takes into account the effect of losses in the antenna panels L_a, the balun L_b, and connector to the receiver L_c, as well as ground losses L_g. Isolating the term T_{ant} and substituting it back into Equation 2.4 yields

$$\tau = \frac{T_{ant}^{L} - (1-L)T_{amb}}{L}\frac{1}{\sigma_T^2\,\Delta\nu}. \tag{3.3}$$

L is a coefficient that ranges from 0 to 1, where 1 represents no loss. Therefore, increasing losses (decreasing L) increases the integration time needed to achieve the desired sensitivity level for our instrument.

Our design of the blade dipole antenna, illustrated in Figure 3.1, consists of two panels with length l and width w, separated by s, and suspended over soil at a height h by a fiberglass support structure. The soil is characterized by two quantities: the conductivity σ, and the permittivity ϵ. The default soil parameters used for the simulations over infinite soil are $\sigma = 0.02$ Sm^{-1}, $\epsilon_r = 3.5$, as suggested by [Sutinjo et al., 2015].

To optimize antenna performance, we addressed the most important effects that can impact the science results: influence of soil parameters and antenna dimensions. In the simulations, we did not include the fiberglass supporting structure, since the effects are expected to be sub-dominant; however, the structure will be included in future simulations as the antenna design is refined. Other scientific works, such as the one presented in [Bernardi et al., 2015], have found that the addition of the fiberglass structure did not produce significant changes in overall antenna performance.

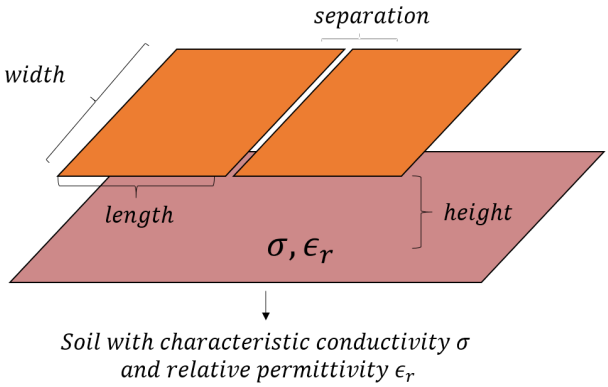

Figure 3.1: Schematic of the blade antenna with two panels with parametrized dimensions as shown, and above soil with characteristic conductivity and permittivity.

Antenna performance is assessed and optimized in terms of (Γ), beam chromaticity, and ground loss. The main objectives in our antenna design are:

- minimization of Γ in the frequency range of $40 - 120$ MHz;
- minimize chromaticity in the antenna beam;
- minimize ground loss.

In order to evaluate different antenna designs and dimensions, we performed EM simulations using FEKO, WIPL-D, and NEC. We started our analysis by choosing a software that we believed could provide the most accurate modelling of soil.

3.2 Influence of meshing in antenna simulations

To explore the effect of meshing, we began with a baseline simulation of a blade antenna with dimensions shown in Table 3.1, for an antenna above infinite soil with $\sigma = 0.02$ Sm^{-1}, and $\epsilon_r = 3.5$, in the frequency range $50 - 110$ MHz.

EM solvers employ several different numerical methods. For a time-domain problem, we can use finite difference time domain method (FTDT). For static systems, we can use finite elements (FE), multilevel fast multipole method (MLFMM), or the Method of Moments (MoM). For MIST and Mini-MIST, which are static problems with open boundaries, MoM is adequate, and therefore it was used to make the simulations.

In FEKO, WIPL-D, and NEC, we used MoM, as the model is only composed of an antenna, and infinite soil beneath it, with its dielectric properties. In MoM, each solid surface is divided into smaller elements that are solved individually in terms of voltage and current, and then summed over

to get the generalized behavior for the entire surface. The number of elements used is also called the number of unknowns, and in MoM,the number of unknowns solved for in each simulation can be controlled by changing the maximum frequency, f_{max}, used in the simulations. An essential part in EM simulations– meshing, is highly affected by the number of unknowns. Meshing is the process involved in the discretization of a surface where the currents are defined and computed into small individual elements that are then summed, to get the behavior of the electric and magnetic fields, by the superposition principle. Default configurations of the softwares determine the meshing automatically for the highest frequency in the simulation (smallest wavelength).

The frequency range of MIST and Mini-MIST is $1-200$ MHz. To explore the effect of meshing I ran simulations with f_{max} varying between 200 MHz and 1000 MHz in steps of 100 MHz. The variation of the number of unknowns is presented in Figure 3.2 and we can see a general increasing trend.

	Antenna dimensions [m]
Height	0.66
Separation	0.04
Length	0.98
Width	1.26

Table 3.1: Initial dimensions for the blade dipole antenna.

The influence of meshing on Γ can be noticed when plotting the entire bandwidth of interest, $1-200$ MHz, presented in Figure 3.3. We can choose a reference value for the maximum frequency as being $f_{ref} = 1000$ MHz. Then, in Figure 3.4 we plot the difference in the magnitude of Γ for all the values of f_{max}, relative to the case with f_{ref}=1000 MHz. We chose $f_{max} = 500$ MHz in our initial exploratory simulations, since it provided a balance between precision and computational time– using highest frequencies produced more precise results, but were much more computationally expensive to obtain. These results suggest that for a better agreement with experimental results, the highest frequency used in the simulations is an important parameter to be considered, as it can affect the value of Γ, as shown in Figure 3.4. Differences in Γ in simulations can also be translated into antenna temperature T_{ant}, as shown by Equation 2.5. Considering $T_{sky} = 3000$ K, a reasonable assumption for low frequencies, a difference as low as 0.01 in magnitude of Γ yields a difference of 460 mK, which is at the same order of magnitude of the global signal from the hyperfine splitting of neutral hydrogen. Residual differences of 3 dB, such as shown by setting a low value for f_{max} in the simulations, result in a difference of approximately 123 K, which is orders of magnitude larger than the one expected for the hydrogen signature. This indicates the importance of rigorously assessing the robustness and precision of simulation results. It is therefore also important to have precise high-resolution measurements of Γ experimentally.

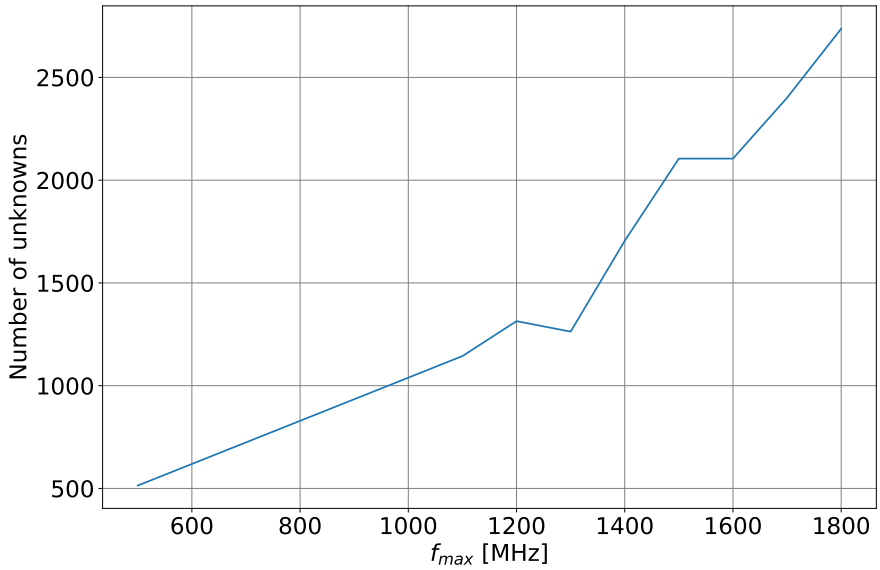

Figure 3.2: Number of unknowns as a function of frequency for an blade dipole antenna simulated with the WIPL-D software.

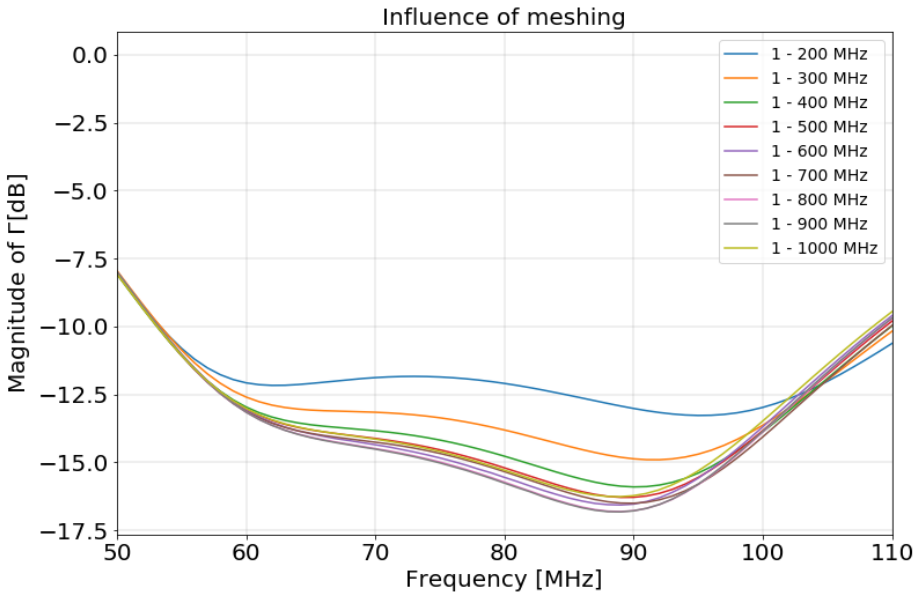

Figure 3.3: Influence of meshing in the magnitude of Γ in WIPL-D, for different f_{max}. In these simulations, we used $\sigma = 0.02$ Sm^{-1}, and $\epsilon_r = 3.5$.

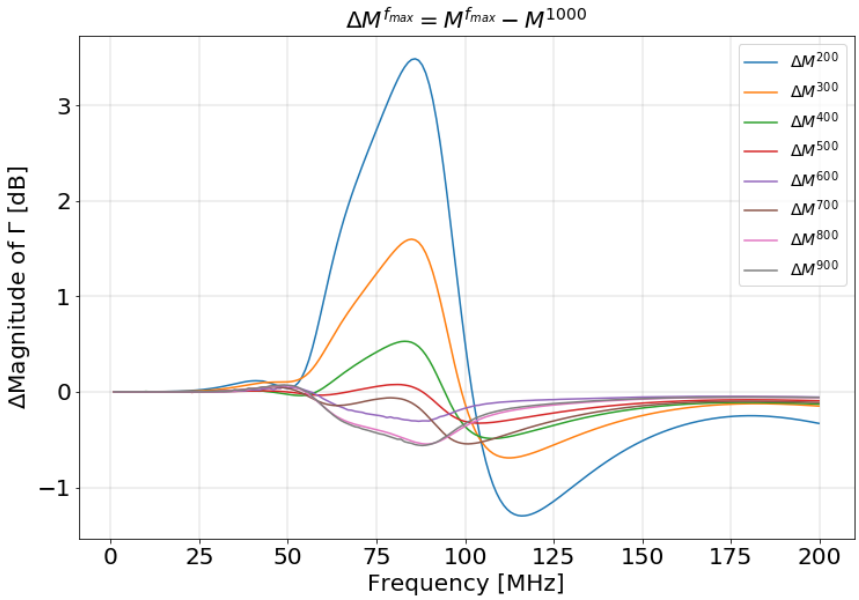

Figure 3.4: Difference in the magnitude of Γ for the different values of f_{max} relative to the case with $f_{max} = 1000$ MHz.

Changes in the number of unknowns also change how the beam gain at a single frequency varies. As a metric, we use the difference between two beams at 120 MHz obtained from simulations in which f_{max} is different. This frequency was chosen because at the highest end, the beam starts to present instabilities, and therefore looking at 120 MHz is a good metric because it's conservative and gives a worst-case picture. For investigating how the beam behaves in both θ and ϕ directions, we define ΔG as

$$\Delta G = G_F^{f_{max}} - G_F^{f_{ref}}, \tag{3.4}$$

where the subscript F indicates the frequency at which the gain is evaluated ($F = 120$ MHz), f_{max} the maximum frequency used in the simulation (which was varied), and f_{ref} the reference frequency, taken as 1000 MHz.

Results are shown in Figure 3.5, and noticeably the largest absolute impact of changing the meshing happens towards the zenith, located at $\theta = 0°$. The meshing has an important influence in this region, since there is a lower gain for the lower f_{max} values compared to f_{ref}. As we increase f_{max}, ΔG is reduced, and for this reason there differences are one order of magnitude smaller, as shown in the middle and bottom plots, adequately adapted for these values. Gain plots for f_{max} higher or equal to 500MHz show differences is at the order of $\pm 10^{-2}$ in gain when compared to the reference case. Other comparison plots that not presented here were also made using $f_{max} = 600$ MHz, $f_{max} = 800$ MHz, and $f_{max} = 900$ MHz, and the ΔG is still within ± 0.0100.

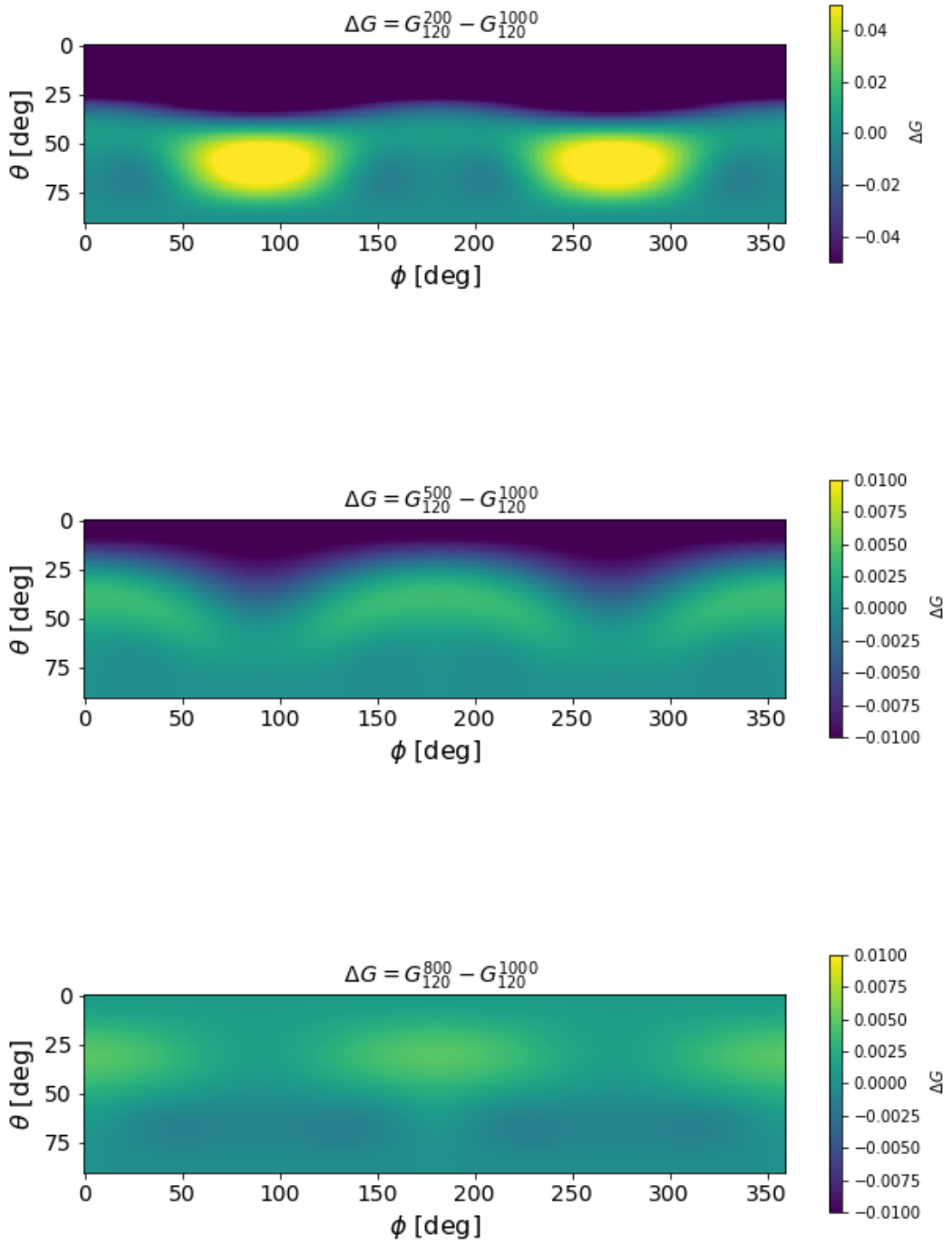

Figure 3.5: ΔG results comparing meshings with $f_{max} = 200, 500$, and 800 MHz to $f_{ref} = 1000$ MHz, all at $F = 120$ MHz. f_{max} was varied from 200 MHz to 900 MHz, but we chose to look at this subset of frequencies.

3.3 Comparing different EM softwares

In this section, we first compared FEKO and WIPL-D simulations of a dipole antenna sitting above an infinite PEC ground plane and above infinite soil. Since results over infinite soil did not agree, we brought a third EM sotware package, NEC, to evaluate simulations for an even simpler antenna model in free space, with an infinite PEC ground plane, and above infinite soil. These comparisons helped us chose the best software for our applications.

3.3.1 FEKO and WIPL-D blade antenna simulations over a PEC ground plane and over soil

Ground planes are metallic structures, often modeled as perfect electric conductors (PEC) which increase the overall gain of an antenna. The EDGES setup [Bowman et al., 2018], for example, included 10×10 m, and 30×30 m ground planes for the low-band instrument.

To evaluate the antenna gain patterns and Γ, we first made simulations in FEKO, and WIPL-D, for the antenna with dimensions presented in Table 3.1 above an infinite PEC ground plane, with a maximum frequency of $f_{max} = 500$ MHz, and double precision. In Figure 3.6, we present the comparison between both solvers in terms of the magnitude of Γ as a function of frequency. Noticeably, there is a difference between the two softwares in terms of Γ, as we can see in Figure 3.6. For the WIPL-D simulation, the minimum value of the reflection loss happens at approximately 98 MHz, at a magnitude of -23 dB. The FEKO simulation shows a minimum of -27 dB, centered at 94 MHz. In terms of the beam gain, the differences are lower than 10^{-2} in terms of the derivative of gain.

We simulated the antenna with the same dimensions over infinite soil with $\sigma = 0.02 \mathrm{Sm}^{-1}$, and $\epsilon_r = 3.5$, keeping double precision, and $f_{max} = 500$ MHz in both softwares. This value for f_{max} was chosen because we ran into computational limits while trying to push f_{max} to higher frequencies to compute the beams in FEKO.

The results are presented in Figure 3.7. We notice that once again, the results for both softwares do not agree. The overall behavior in magnitude of Γ is remarkably different between the two softwares. Resuls show a difference of 4 dB at lower frequencies, which diminishes to 1 dB at the minimum value, where it stabilizes and continues for the rest of the band.

The difference between each value of gain across frequency $\Delta G/\Delta f$ is calculated as

$$\frac{\Delta G}{\Delta f} = G_{f+1} - G_f, \tag{3.5}$$

and will be used for what we call derivative plots. Derivative plots will be usual in our further explorations and presentation of antenna beam patterns with changing soil properties, as they allow

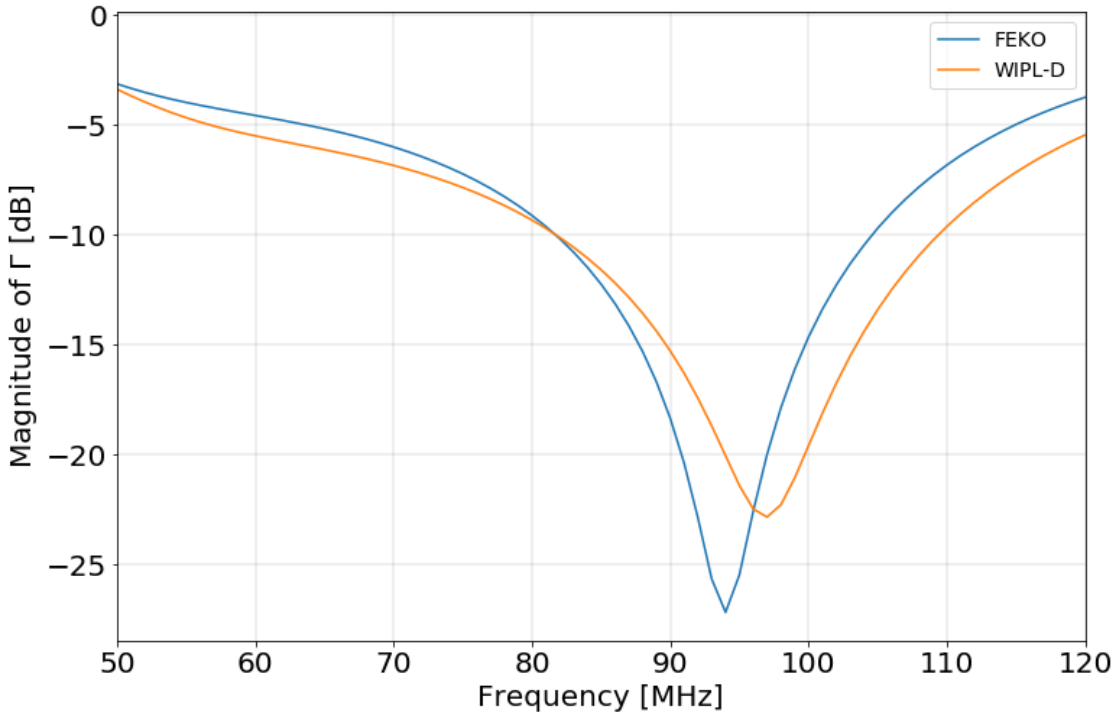

Figure 3.6: Magnitude of Γ in dB as a function of frequency for both solvers, with $f_{max} = 500$ MHz, for the blade antenna above an infinite PEC ground plane.

us to evaluate the chromaticity of the beam. A beam chromaticity evaluation is important, as we mentioned, since chromatic beams might mimic or confuse the detection of the 21-cm global signal.

In Figure 3.8, the results of beam gain across frequency using FEKO, and in Figure 3.9, the results of beam gain across frequency using WIPL-D. On the left side of these plots, we see the beam gain at three different values of ϕ, and on the right side, the derivative plots. These beams present a smooth behavior as a function of frequency, with a gain towards the zenith, $\theta = 0°$.

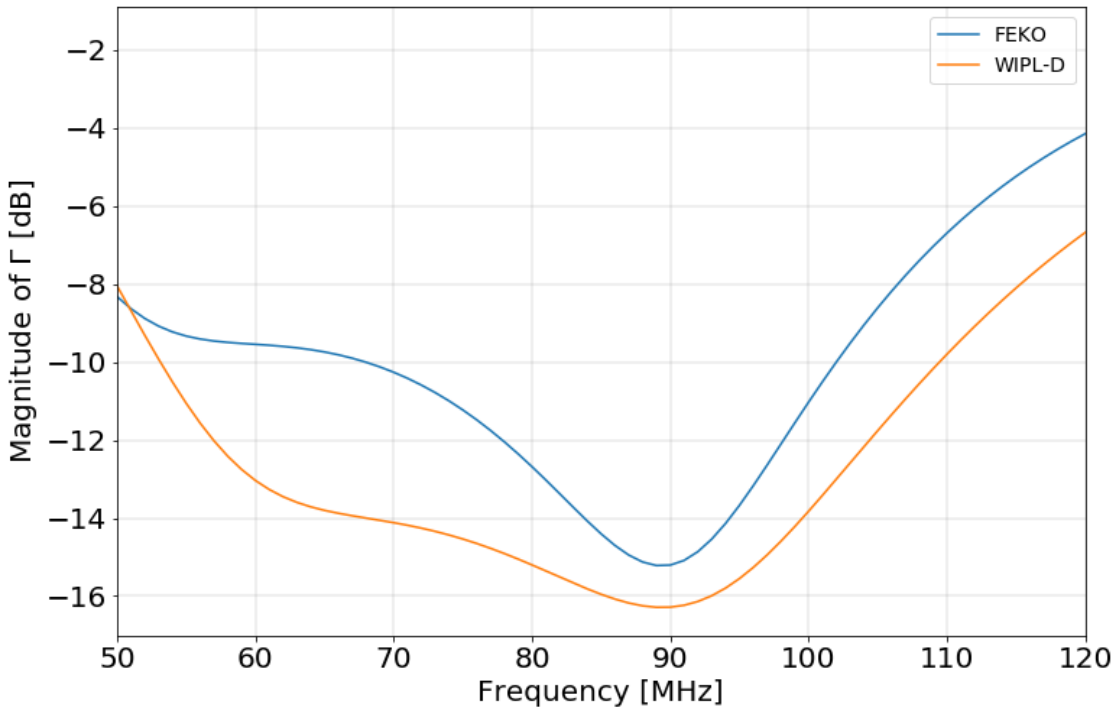

Figure 3.7: Magnitude of Γ in dB as a function of frequency for both solvers, with $f_{max} = 500\,\text{MHz}$, for the blade antenna above infinite soil.

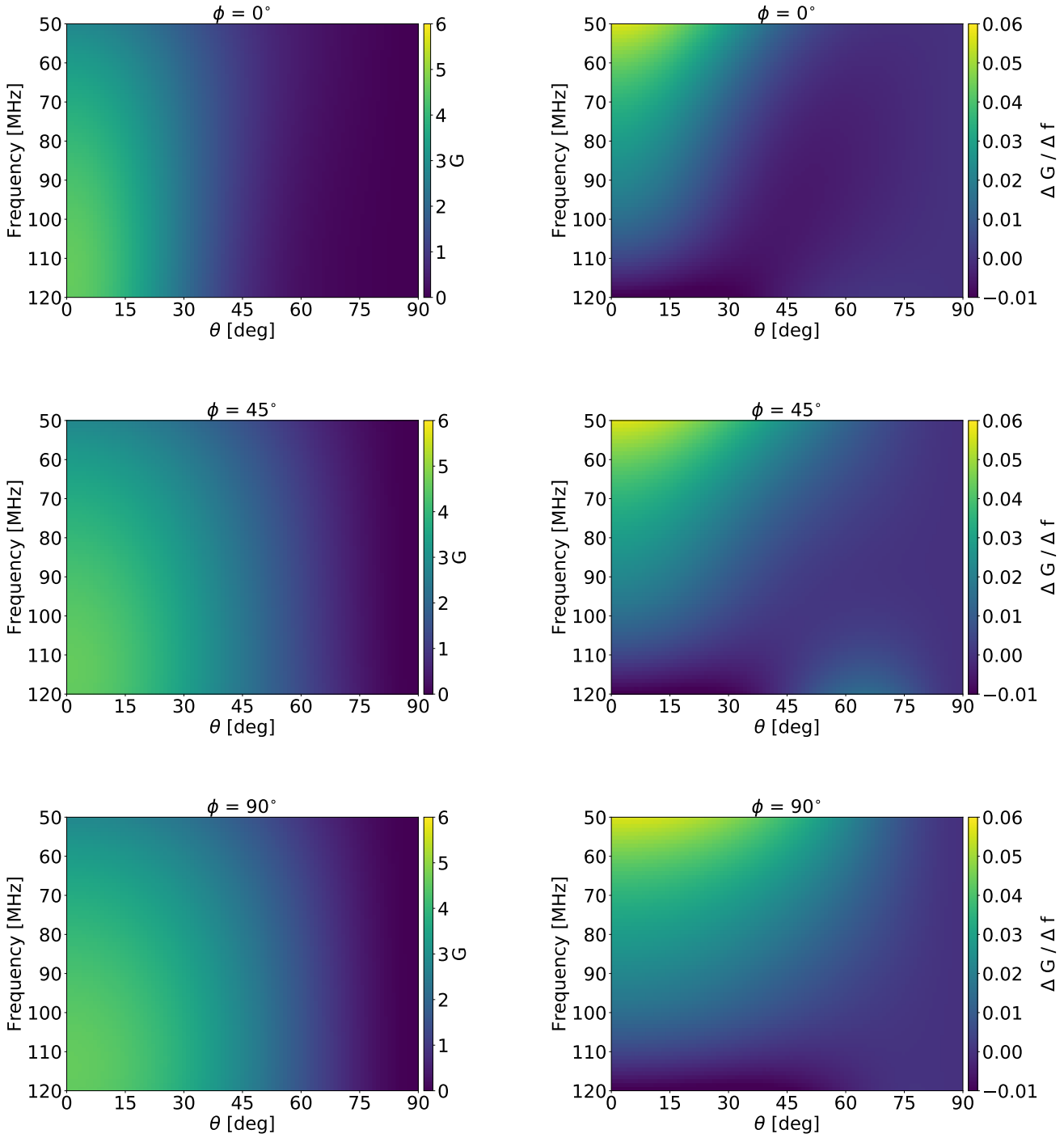

Figure 3.8: Left: Gain for the blade antenna above infinite soil with $\epsilon_r = 3.5$ and $\sigma = 0.02$ Sm^{-1}, at $\phi = 0°$, $\phi = 45°$, and $\phi = 90°$, simulated in FEKO. Right: Gain derivative as a function of frequency for the same three values of ϕ.

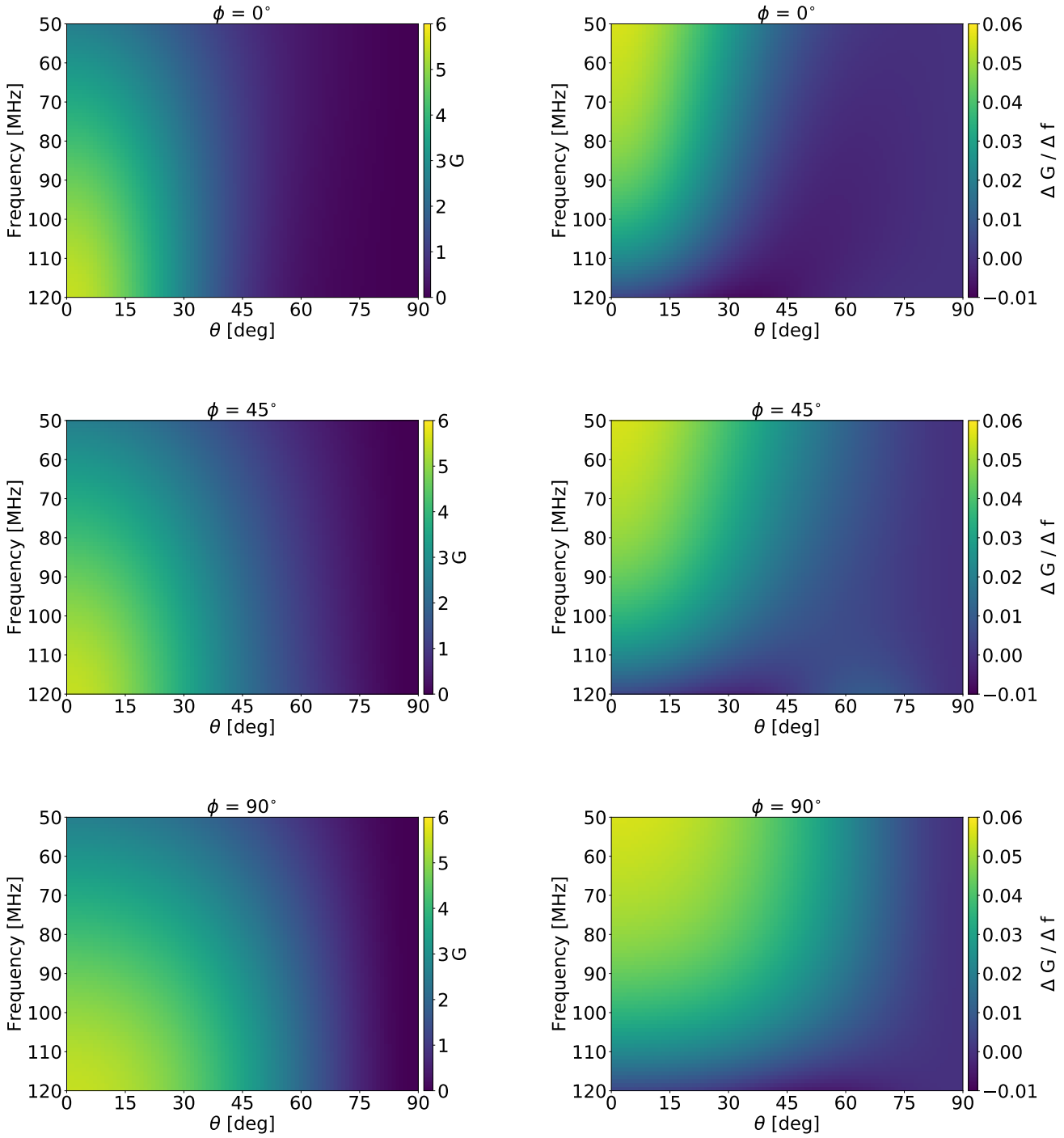

Figure 3.9: Left: Gain for the blade antenna above infinite soil with $\epsilon_r = 3.5$ and $\sigma = 0.02$ Sm^{-1}, at $\phi = 0°$, $\phi = 45°$, and $\phi = 90°$, simulated in WIPL-D. Right: Gain derivative as a function of frequency for the same three values of ϕ.

Results for the beam gain, and beam chromaticity also show an inconsistency between the two softwares, as we see in In Figures 3.8 and 3.9. In WIPL-D, results point to greater chromaticities are spread across θ, compared to FEKO.

3.4 FEKO, WIPL-D, and NEC simulations for wire dipole antenna

We saw disagreements between FEKO and WIPL-D, and therefore we performed new simulations using a third software, NEC which also solves the models numerically using MoM. We also chose to investigate an even simpler model: a wire dipole antenna, in order to check if the fundamental way that each software deals with PEC ground planes, soil, or free space, is different.

Simulations were made in free space, above an infinite PEC ground plane, and above infinite soil. The length of the wire dipole used was $l = 1.26$ m, with a PEC wire of radius 1 mm. The soil parameters were $\sigma = 0.02$ Sm^{-1} and $\epsilon_r = 3.5$. In all solvers, we used $f_{max} = 200$ MHz.

The comparisons of Γ between FEKO, WIPL-D, and NEC agree when the antenna is simulated in free space (Figure 3.10a), and when it is simulated above an infinite PEC ground plane (Figure 3.10b), but they do not agree over infinite soil, (Figure 3.10c). In fact, the WIPL-D results are the same for free space as for infinite soil, therefore indicating that it does not solve properly over two different media as the other software packages used.

Figure 3.11 shows the gain calculated by FEKO; the results from WIPL-D and NEC look qualitatively similar. The gain differences between WIPL-D and FEKO are highlighted in 3.12. Figure 3.12, presents results for difference in beam gain comparing WIPL-D and FEKO across θ and ϕ for the wire dipole antenna in free space, above infinite PEC ground plane, and above infinite soil, at $f = 119$ MHz. For free space, and for infinite PEC ground plane, the agreement is good, and the difference is of approximately 1 %. However, for infinite soil, we see significant differences for the beam gain, that can reach up to 16% at some specific zenith angles.

The complete comparison between the three software packages is presented in Memo 25, written for the MIST collaboration. We conclude from these investigations, that WIPL-D fails to accurately model the impact of soil. We therefore selected FEKO to guide our future efforts in antenna design. I would also like do acknowledge the help of Tristan Ménard in performing the NEC simulations for this part.

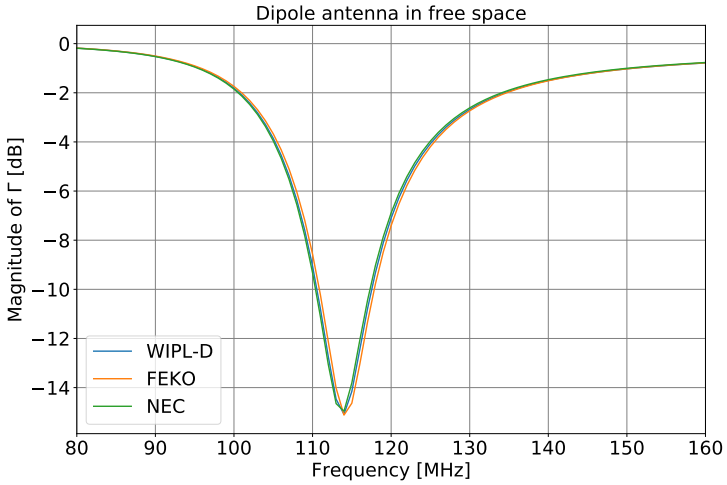

(a)

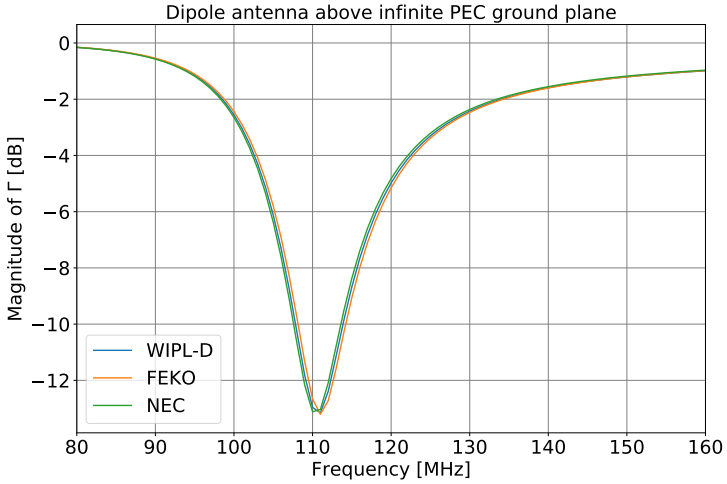

(b)

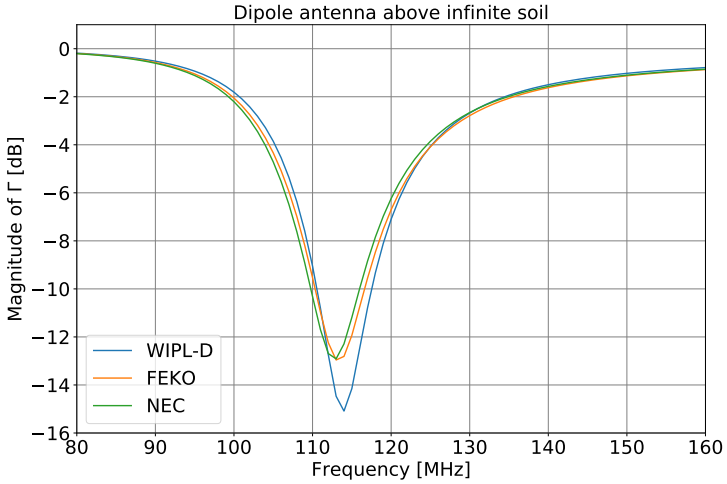

(c)

Figure 3.10: Magnitude of Γ in dB as a function of frequency for the wire dipole antenna in (a) free space, (b) above an infinite PEC ground plane, (c) above infinite soil, simulated in FEKO, WIPL-D and NEC, with f_{max} = 200 MHz.

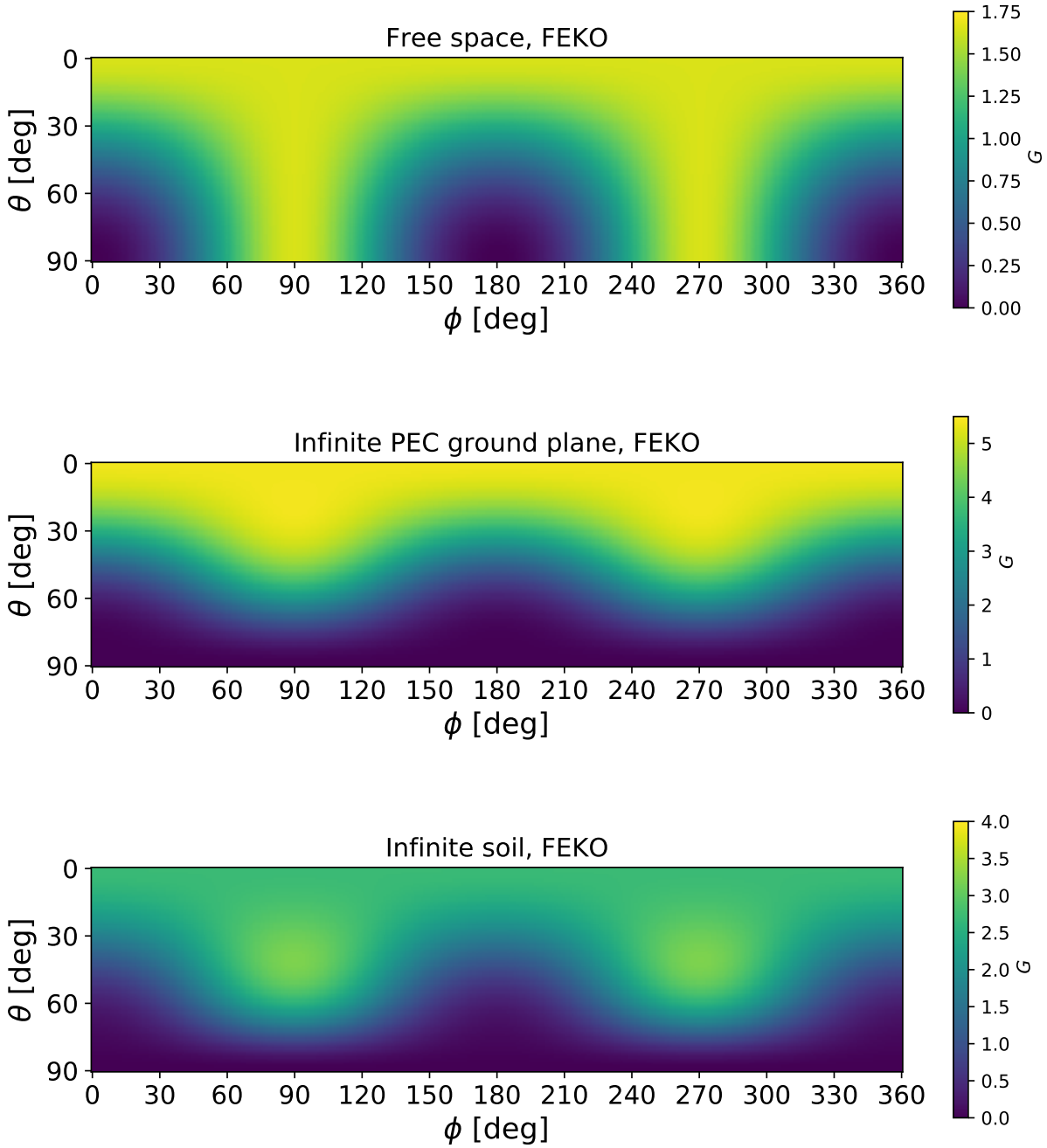

Figure 3.11: Beam gain G across θ and ϕ for the wire dipole antenna above free space (top), infinite PEC ground plane (middle), and above infinite soil (bottom), at $f = 119$ MHz, simulated in FEKO. Results from other packages look qualitatively similar.

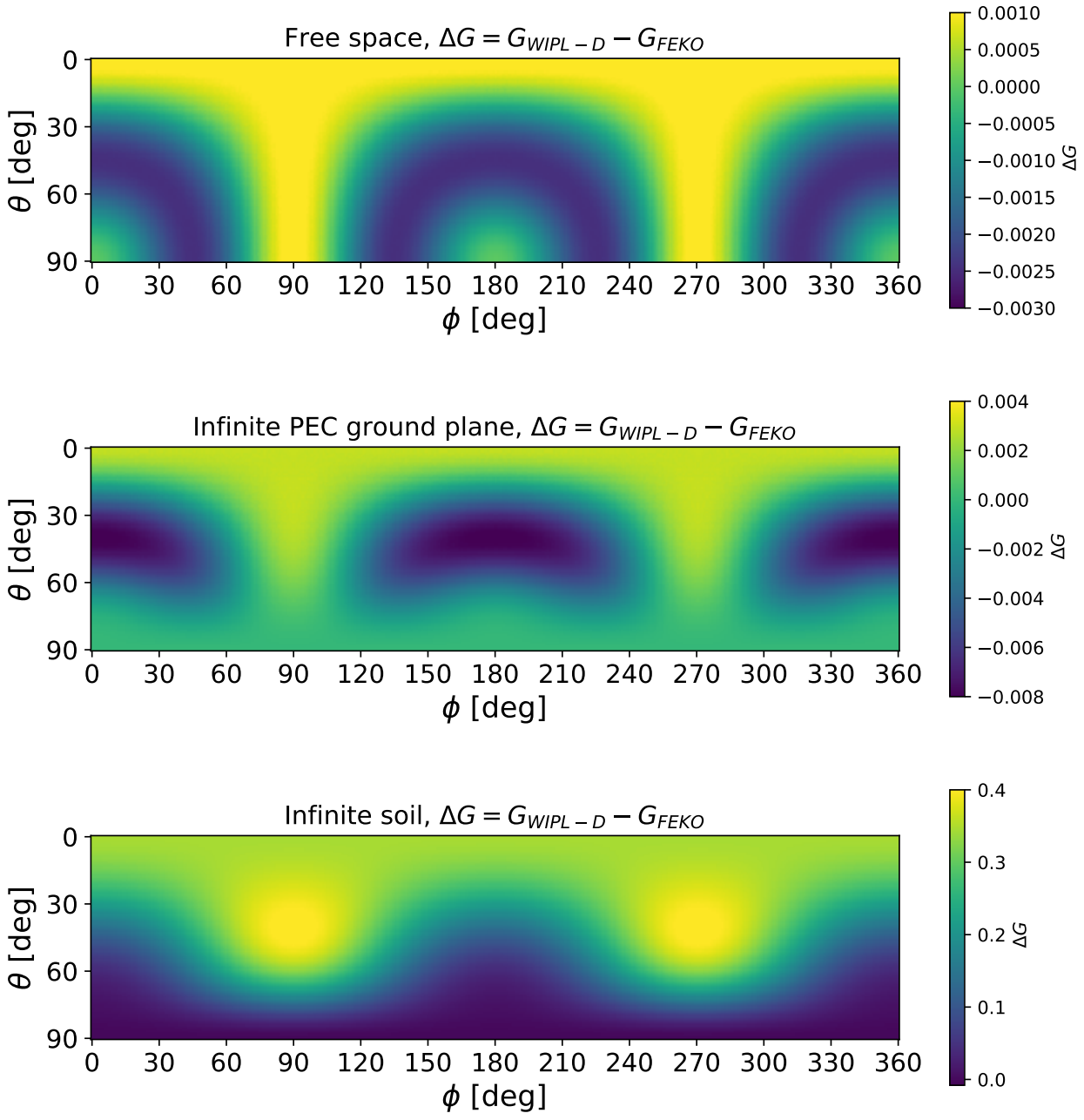

Figure 3.12: Top: Beam gain ΔG across θ and ϕ for the wire dipole antenna above an infinite PEC ground plane at $f = 119$ MHz, simulated in WIPL-D. Middle: ΔG across θ and ϕ for the wire dipole antenna above an infinite PEC ground plane at $f = 119$ MHz, simulated in FEKO. Bottom: ΔG comparing results from the two solvers.

3.5 MIST Prototype antenna

3.5.1 Optimization and investigating perforated panels

After defining that FEKO was the best choice to investigate the antenna performance, we performed several manual optimizations in antenna dimensions, investigating how changes in length, height, width, and separation between angles, changed the overall behavior of Γ, and beam gain. The optimization objective was a minimum of $\Gamma = -10$ dB across the widest bandwidth possible. After the optimizations, the new dimensions for the antenna are presented in Table 3.2.

	Antenna dimensions [m]
Height	0.75
Separation	0.02
Length	1.18
Width	1.40

Table 3.2: Optimized dimensions for the MIST dipole antenna.

These dimensions were chosen for the construction of a prototype antenna, as it is optimized for 50 MHz in terms of Γ, as shown in the solid blue line in Figure 3.13. The gain pattern is presented in Figure 3.14.

Since we plan to deploy the antenna at remote locations in order to avoid RFI, it is important to consider the weight of the panels, for logistic reasons. One way to maintain the antenna dimensions and diminish the weight, is to consider perforated panels, and therefore we investigated these effects in the simulations.

The first antenna with perforated panels investigated has 238 holes with radius r = 0.02 m and separated by 0.08 m in each panel, representing a total area of $A_1 = 0.30$ m^2, as the total area of each panel is approximately $A_t = 1.65$ m^2. The total open area A_o is 18%. The second model we present has 391 holes with radius r = 0.02 m and separated by 0.05 m in each panel, giving a total area of $A_2 = 0.49$ m^2. The total open area is $A_o = 30\%$. Values for A_1 and A_2 were chosen to be approximately the same as in the panels available on the market. We present a comparison between blade antennas with perforated panels and solid PEC panels. These antennas were simulated in FEKO above infinite soil with $\epsilon_r = 3.5$ and $\sigma = 0.02$ Sm^{-1}, $f_{max} = 120$ MHz in the two cases, with standard meshing. It is important to mention that even though the maximum frequency was the same, simulations for the perforated plates had a finer meshing, as more triangles of a same size were needed to fill the surface of the antenna plates. This being the case, even for $f_{max} = 120$ MHz, we also reached the edge of our computational capabilities, and could not investigate higher frequencies.

The results for Γ for the antenna with solid panels and the ones with perforated panels and different open areas are presented in Figure 3.13, and noticeably, an A_o = 18 % increased the magnitude of Γ at lower frequencies, while keeping a level lower than -15 dB until ~ 83 MHz. With A_o = 30 %, most noticeably the reflections in the 50-60 MHz decreased, but increased as a function of frequency, achieving a higher magnitude of Γ than the solid case for frequencies above 70 MHz. Figure 3.14 presents the beam pattern for the antenna with solid panels, for reference. Figure 3.15 shows the comparison of the reference to the antenna with perforated panels and A_o = 18%, and Figure 3.16 the comparison to the antenna with perforated panels and A_o = 30%. Noticeably, the differences in gain are not significant, and account for for a maximum of 2 % of the gain; differences in the derivatives are also minimal, of about ±3 % for $\Delta G/\Delta f$ when comparing the two perforated cases with the solid reference.

During these simulations, the number of mesh cells was not kept constant, as mentioned before, due to the number of mesh triangles needed to cover the surface of the panels in each case. We cannot affirm that the differences in Γ and in beam gain pattern are due to the perforations explicitly, instead of being due to the difference in mesh cells. In order to address this issue in more detail changing the size of the triangles would be needed. Although the details of the Γ results for the perforated panels are not fully understood at this point, and the differences with respect to solid panels may therefore be either physical or numerical, we decided to take the conservative approach of proceeding with solid panels for the prototype. This is an important design decision, as it accounts for a way to diminish the uncertainties in the construction of our antenna. For example, differences in the positioning of the holes or in their diameter could cause important influences in Γ that would be hard to model in our simulations.

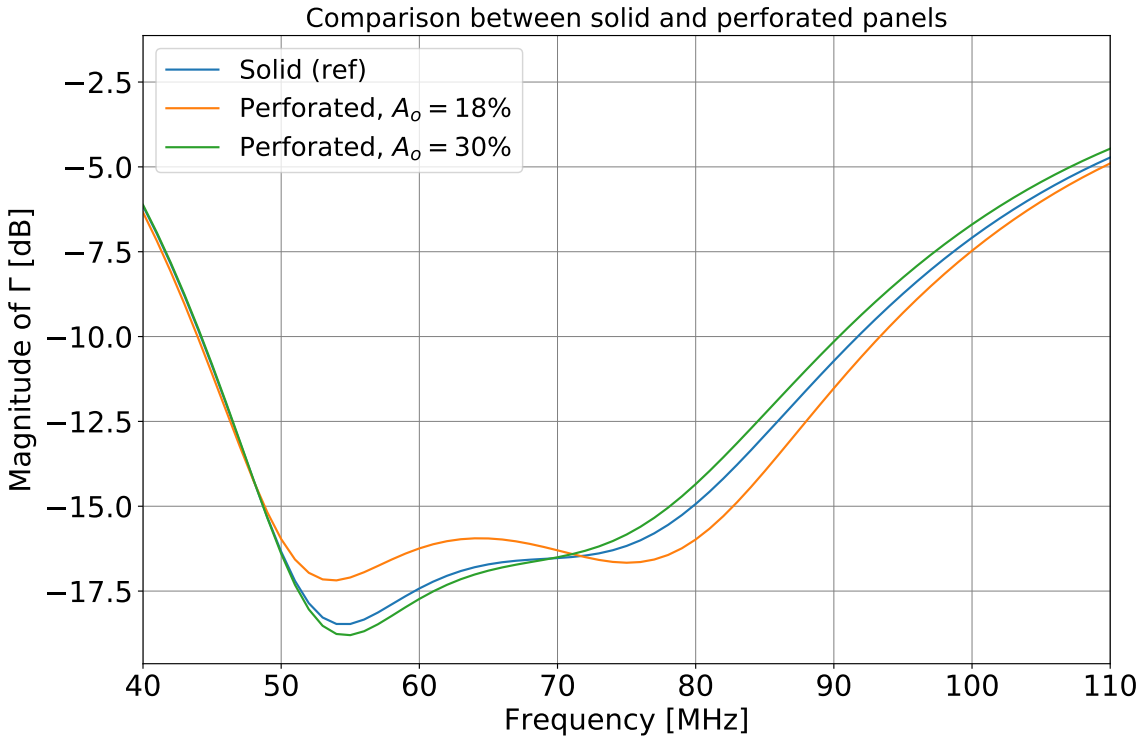

Figure 3.13: Results for Γ in the blade antenna with solid panels and perforated panels. The Γ minimum shifts towards lower magnitudes for the perforated cases. The magnitude of Γ starts increasing at lower frequencies, around 80 MHz for $A_o = 18\%$, and at 70 MHz for $A_o = 30\%$, while the increase starts at around 84 MHz for the solid panels.

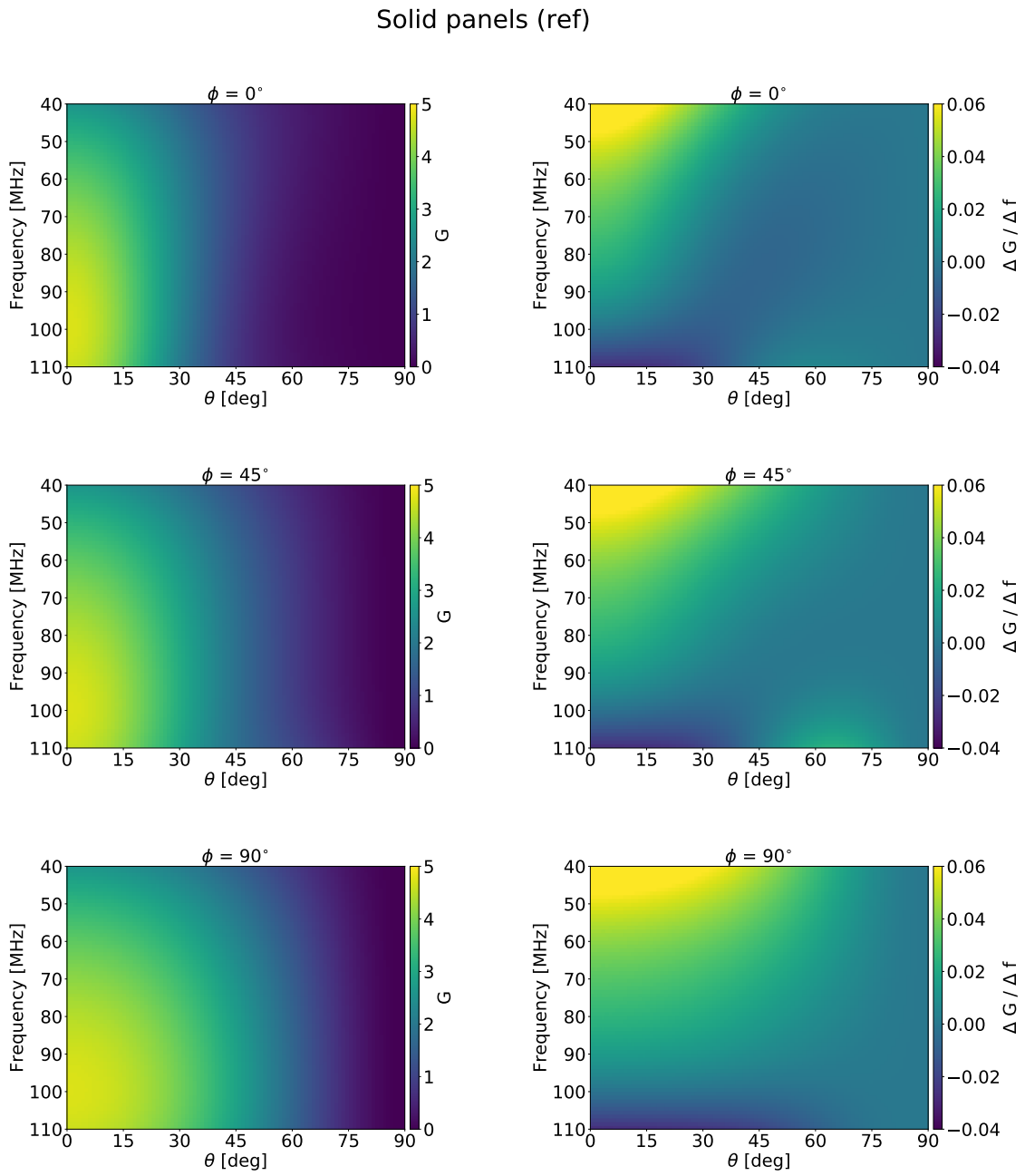

Figure 3.14: Left: Beam gain for the blade antenna with solid panels above infinite soil with $\epsilon_r = 3.5$ and $\sigma = 0.02$ S/m, at $\phi = 0°$, $\phi = 45°$, and $\phi = 90°$ for $f_{max} = 120$ MHz, simulated in FEKO. Right: Comparison of the gain derivative as a function of frequency for the same three values of ϕ.

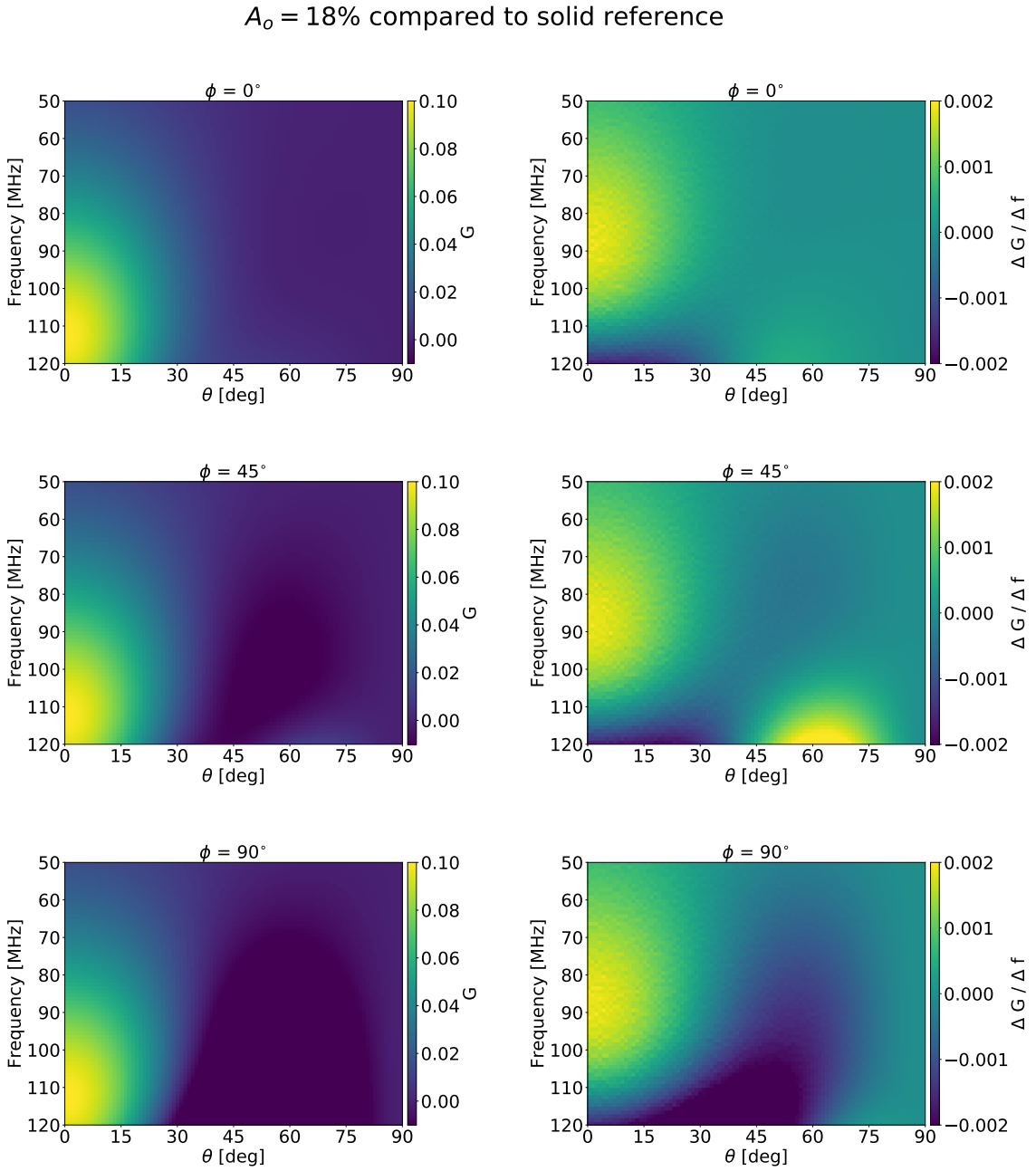

Figure 3.15: Left: Beam gain comparison between the blade antenna with $A_o = 18\%$ and the solid reference. Simulations were made above infinite soil with $\epsilon_r = 3.5$ and $\sigma = 0.02$ S/m, at $\phi = 0°$, $\phi = 45°$, and $\phi = 90°$ for $f_{max} = 120$ MHz, simulated in FEKO. Right: Comparison of the gain derivative as a function of frequency for the same three values of ϕ.

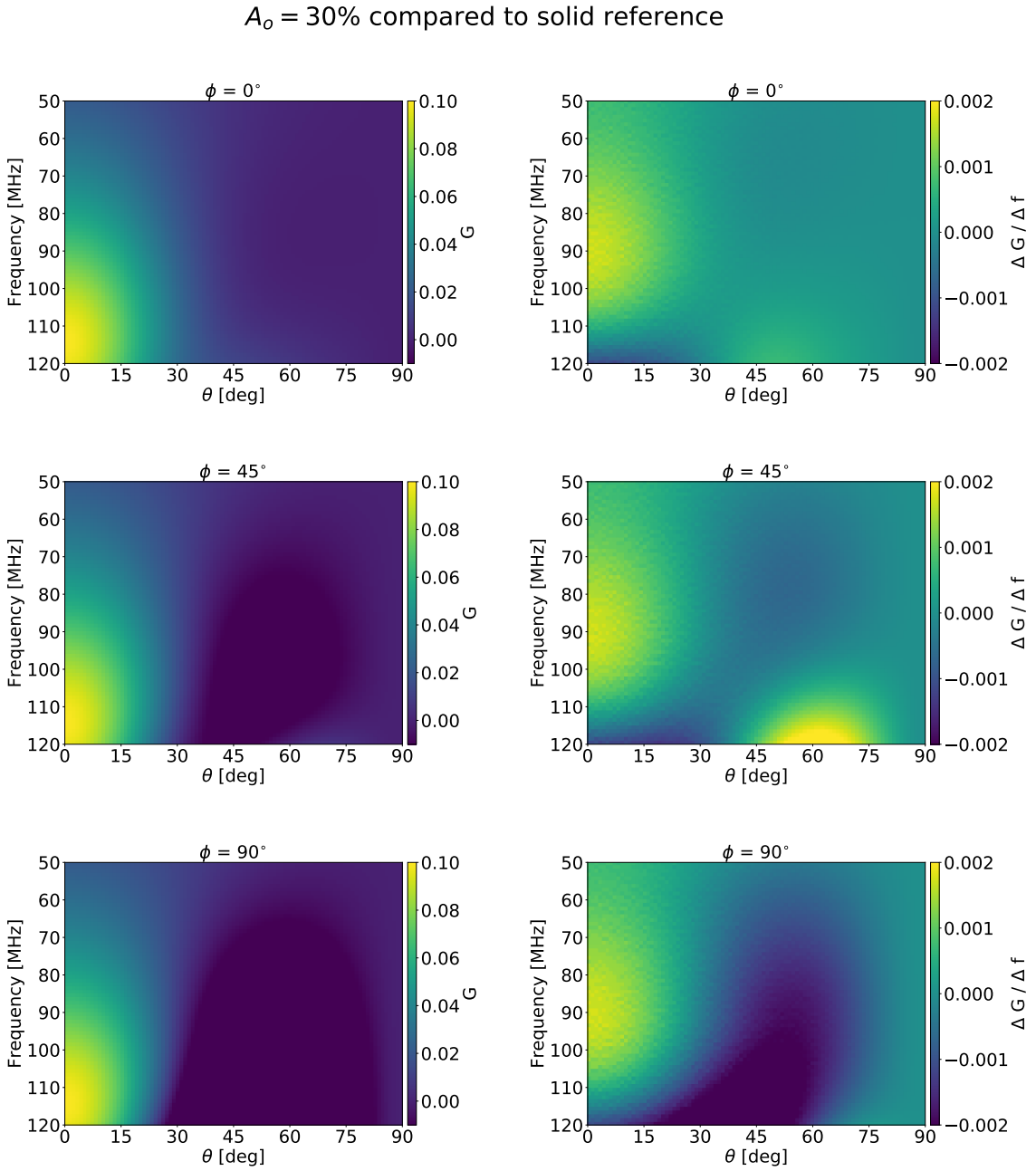

Figure 3.16: Left: Beam gain comparison between the blade antenna with $A_o = 30\%$ and the solid reference. Simulations were made above infinite soil with $\epsilon_r = 3.5$ and $\sigma = 0.02$ S/m, at $\phi = 0°$, $\phi = 45°$, and $\phi = 90°$ for $f_{max} = 120$ MHz, simulated in FEKO. Right: Comparison of the gain derivative as a function of frequency for the same three values of ϕ.

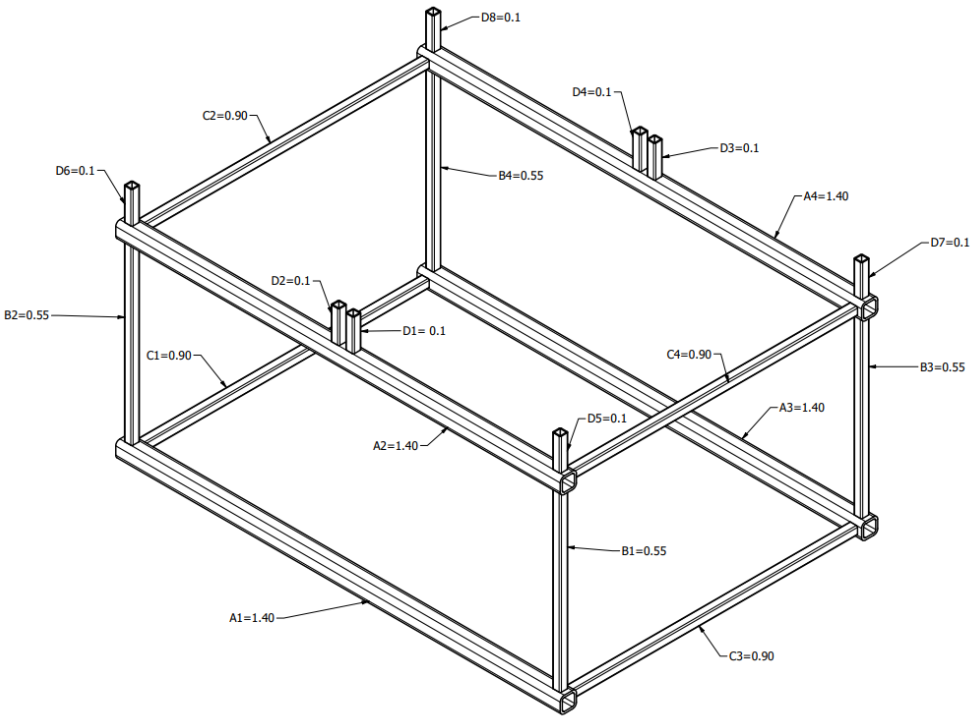

Figure 3.17: Schematics for the construction of the framework for the blade antenna. These are the drawings considering the fiberglass square tubes; the threaded rods were placed accordingly to what is described in Memo 33.

3.5.2 Antenna support structure design and material

The design of the antenna support structure was made using Autodesk Inventor, and the assembly drawing is shown in Figure 3.17. To build the antenna support structure, we used fiberglass tubes and nylon threaded rods, in order to avoid any other EM interference in the measurements. In Table 3.3, we present all the specific items that compose the antenna support structure, and the quantities bought from McMaster.

Item	Quantity	Width (in)	Length (ft)	Link
2-inch tubes	4	2	5	8548K23
1-inch tubes	5	1	5	8548K21
Threaded rods	5	0.5	6	98831A710
Pack with 50 Nuts	**1**	**-**	-	94812A930

Table 3.3: Specific items used for the construction of the antenna support structure.

3.5.3 Experimental setup and results

The site we chose for initial testing a prototype of our antenna was the front lawn at McGill University. This site was chosen due to its reasonably large extent of flat terrain, and because we would be able to test the antenna over soil. This experiment had the objective of mechanically testing the antenna structure, in order to verify its stability, and to test the Γ parameter, and compare it to simulations. The setup consisted of the blade antenna that was assembled over soil, with the dimensions described in Table 3.1.

The structure of the antenna showed reasonable mechanical stability in these initial tests. Although the antenna support structure successfully withstood the weight of the panels, the structure was not sufficiently rigid and could possibly be deflected under windy conditions on the field. Curvature in the panels due to their weight was also observed, and it is a necessary improvement for further designs.

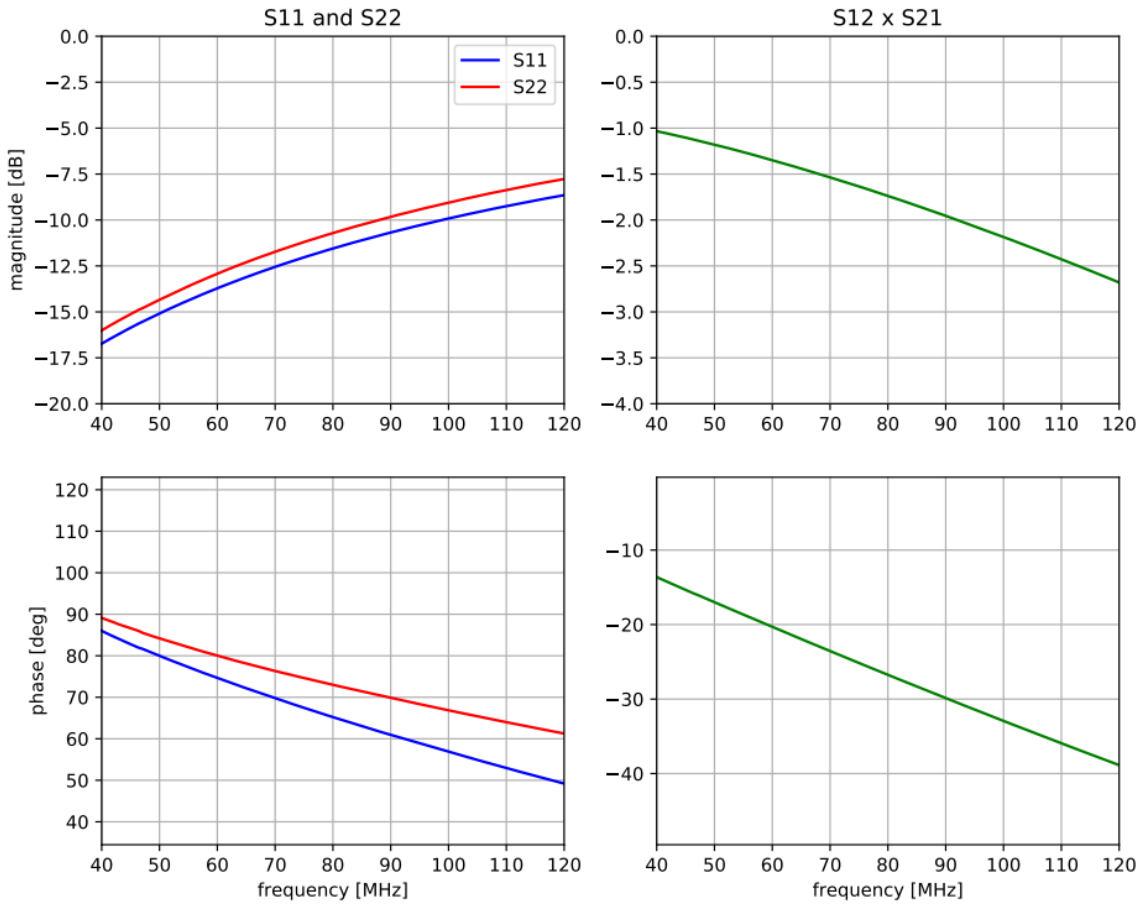

Figure 3.18: S-parameters of the balun assembly based on the Mini-Circuits TX1-1+ transformer.

In order to measure the antenna Γ, we used a balun. The balun was based on a 50-ohm 1:1 surface-mount transformer (Mini-Circuits TX1-1+), which is soldered on a small PCB . In the assembly, to one side of the transformer (the balanced input) we soldered two short wires that connect to the antenna panels. The other side of the transformer (the unbalanced output) leads to an SMA connector. The balun parameters, Γ (S11), S22, S12, and S21, are presented in 3.18, and in a Smith chart as shown in Figure 3.19.

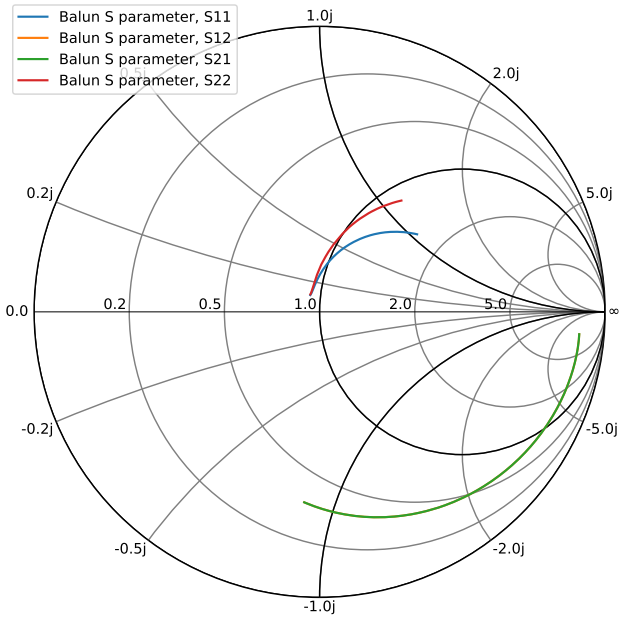

Figure 3.19: Smith chart displaying the S-parameters of the balun assembly based on the Mini-Circuits TX1-1+ transformer.

In Figure 3.20, we present the experimental setup. Variations were applied, and Γ values were recorded for each. The following variations were explored: measurements with the Nano VNA and the Copper Mountain R60 VNA; antenna orientation (East-West, to North-South); influence of which surface of the panel was being used (flipped, and non-flipped); antenna height (nominal value, of 75 cm, 84 cm, and 87 cm); addition of a metal box (width = 30 cm, length = 40 cm, height = 30 cm) beneath the antenna. The measurements reported were made in November 7th, 2020, and at this date, we had not yet developed a method to measure the soil parameters. Therefore, rather than using experimentally determined soil parameters, we ran simulations with different combinations of soil parameters to obtain the better agreement with the experimental data.

Figure 3.20: (a), the site where we took the measurements, with the materials used: toolbox, VNAs, and other tools; (b) the antenna in East-West orientation; (c) the antenna with added height (of approximately 8 cm), and one flipped panel; (d) antenna compared to myself in terms of size.

In Figure 3.21, we present all experimental results obtained. We see a notable dip centered at 68 MHz. In (a), we compare the Nano VNA results with the ones obtained by the Copper Mountain R60, and measurements are consistent. In (b), we change the orientations of the panels from North-South to East-West, and observe no significant difference in the behavior of Γ. Flipping one of the panels also did not produce a significant change at the frequency where the dip is centered, as we see in (c). The most notable difference, in this case, is the amplitude of Γ, that increased to higher values by 8 dB, though maintaining the same structure and behavior across the frequency range 30-120 MHz.

We increased the height between the panels and the surface of the soil by introducing wooden structures beneath the horizontal fiberglass tubes at the bottom of the antenna structure. We were able to obtain two different heights, of 84 cm, and 87 cm, respectively, which are presented in (d), compared to the nominal height of 75 cm. We notice a trend in these results: increasing the

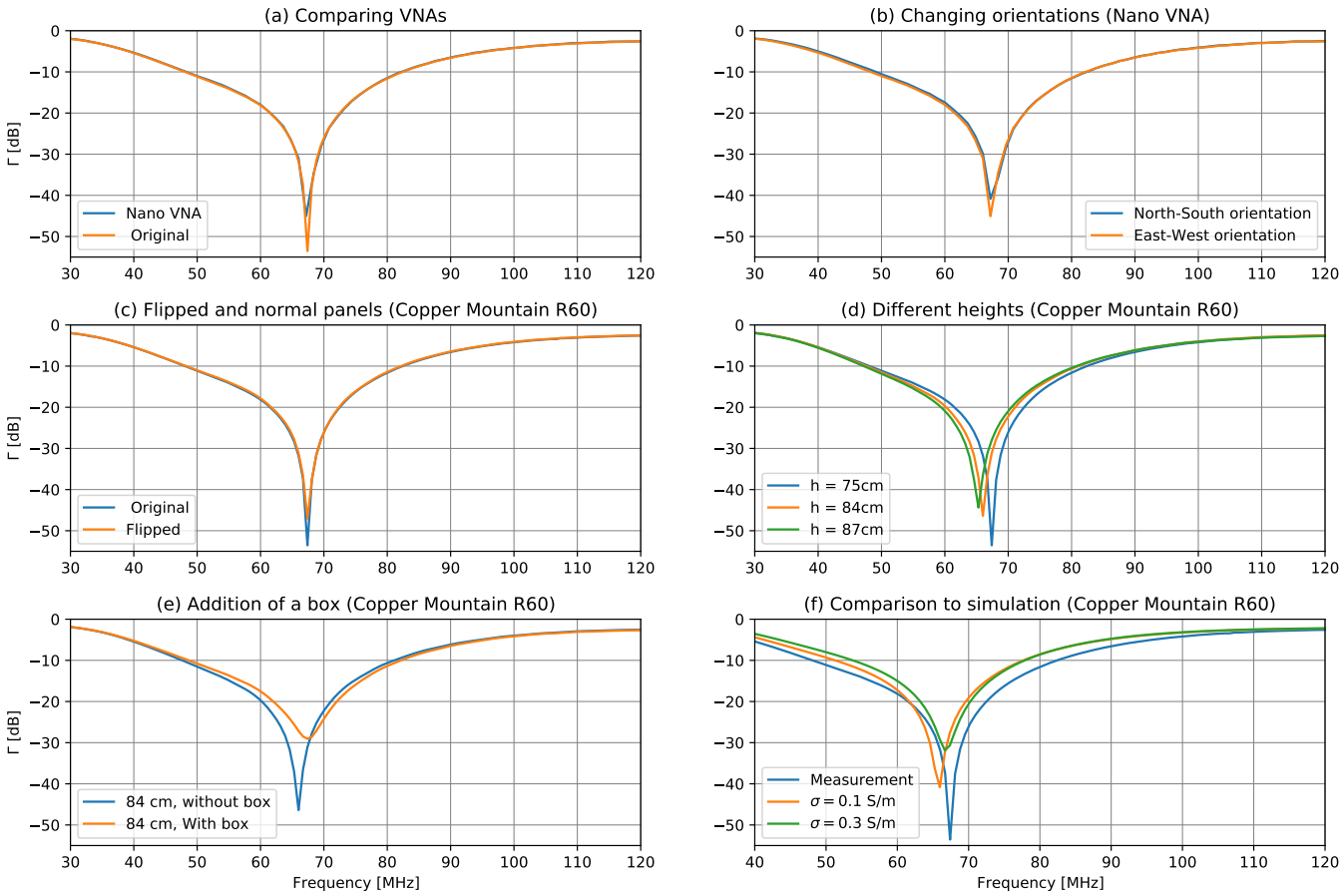

Figure 3.21: Complete set of measurements taken at the McGill front lawn, in November 7th, 2020, showing the magnitude of Γ as a function of frequency. (a) a comparison between two different VNAs, the Nano VNA, and the Copper Mountain R60; (b): effect of changing the orientation of the antennas from North-South to East-West; (c) influence of flipping one of the panels; (d) testing the antenna at different heights; (e) comparison of experimental results to FEKO simulations with different soil parameters, $\sigma = 0.1$ Sm^{-1}, $\sigma = 0.3$ Sm^{-1}, with $\epsilon_r = 3.5$.

height of the antenna brought the lowest point in Γ to lower frequencies, while also diminishing the amplitude by approximately 8 dB, which is consistent with simulations.

When the instrument is fully assembled and operational, the readout electronics will be housed in a metal box beneath the panels, within the antenna support structure. The presence of the electronics enclosure is expected to impact the antenna performance, and the results for adding

the box is presented in (e). We notice that the addition increased the reflections by approximately 20 dB, and also translated the dip to slightly higher frequencies.

In (f), we present a comparison of the experimental results obtained with the Copper Mountain R60 VNA, with antenna simulations made in FEKO, with $\sigma = 0.1$ S/m, $\sigma = 0.3$ S/m, and $\epsilon_r = 3.5$ for both cases. These values were obtained after an extensive exploration and combination of different soil parameters. These simulations were made with a panel thickness of 3 mm, and $f_{max} = 500$ MHz, with a resolution of 1 MHz. During our explorations, we found that including the thickness is **crucial** for a better agreement with the experimental results. The curves presented in (f) were obtained by embedding the S-parameters of the balun using

$$\Gamma' = S_{11} + \frac{S_{12}S_{21}}{1 - S_{22}\Gamma}, \tag{3.6}$$

where Γ' is the intrinsic reflection coefficient of the antenna relative to the reference impedance of 50, S_{11}, S_{12}, and S_{21} are the S-parameters for the balun at the reference plane [Monsalve et al., 2016].

3.5.4 Evaluation of ground loss

One of the drawbacks of using an antenna over soil is the increase of ground loss, which affects the measured sky temperature [Monsalve et al., 2017b]. Equation 3.2 shows the relation between antenna measured temperature as a function of the loss coefficient L, which depends on ground loss L_g. To obtain the ground loss, it is necessary to describe the antenna beam pattern above and below the horizon, integrating the gains over the solid angles. The following approximation is used, since FEKO cannot calculate the antenna pattern below the horizon when there is the presence of a conducting medium, such as soil. The beam solid angle of an antenna over the full sphere is

$$\Omega_A = \int_0^{2\pi} \int_0^{\pi} G(\nu, \theta, \phi) d\theta d\phi, \tag{3.7}$$

where $G(\nu, \theta, \phi)$ is the antenna beam gain across frequency, as a function of θ, and ϕ. For a 100% efficient antenna, we have $\Omega_A = 4\pi$. Therefore, in order to estimate the ground loss, first the fractional solid angle above the horizon is calculated as

$$\Omega_A^+ = \frac{\int_0^{2\pi} \int_0^{\pi/2} G(\nu, \theta, \phi) \sin\theta d\theta d\phi}{4\pi}. \tag{3.8}$$

The fractional solid angle below the horizon (ground loss) is given by

$$\Omega_A^- = \frac{\int_0^{2\pi}\int_{\pi/2}^{\pi} G(\nu,\theta,\phi)\sin\theta d\theta d\phi}{4\pi}. \tag{3.9}$$

Therefore,

$$L_g \equiv \Omega_A^- = 1 - \Omega_A^+. \tag{3.10}$$

Figure 3.22, shows the antenna ground loss, obtained from a simulation in FEKO, with $\sigma = 0.02\mathrm{Sm}^{-1}$, and $\epsilon_r = 3.5$. The bottom panel shows a decrease of antenna ground loss below the horizon as the frequency increases. For frequencies above 70 MHz, the ground loss is less than 35%. As soil conductivity increases, ground loss decreases, as a highly conductive soil favors the reflections of waves. Simulations evaluating the influence of conductivity in ground loss are presented in MIST Memo 42 [1]. Ground loss affects the measured sky temperature as presented in Equation 3.3, but increasing the observation time can account for this.

[1] MIST Memo 42 - Beam Solid Angle of Blade Antenna Above Soil

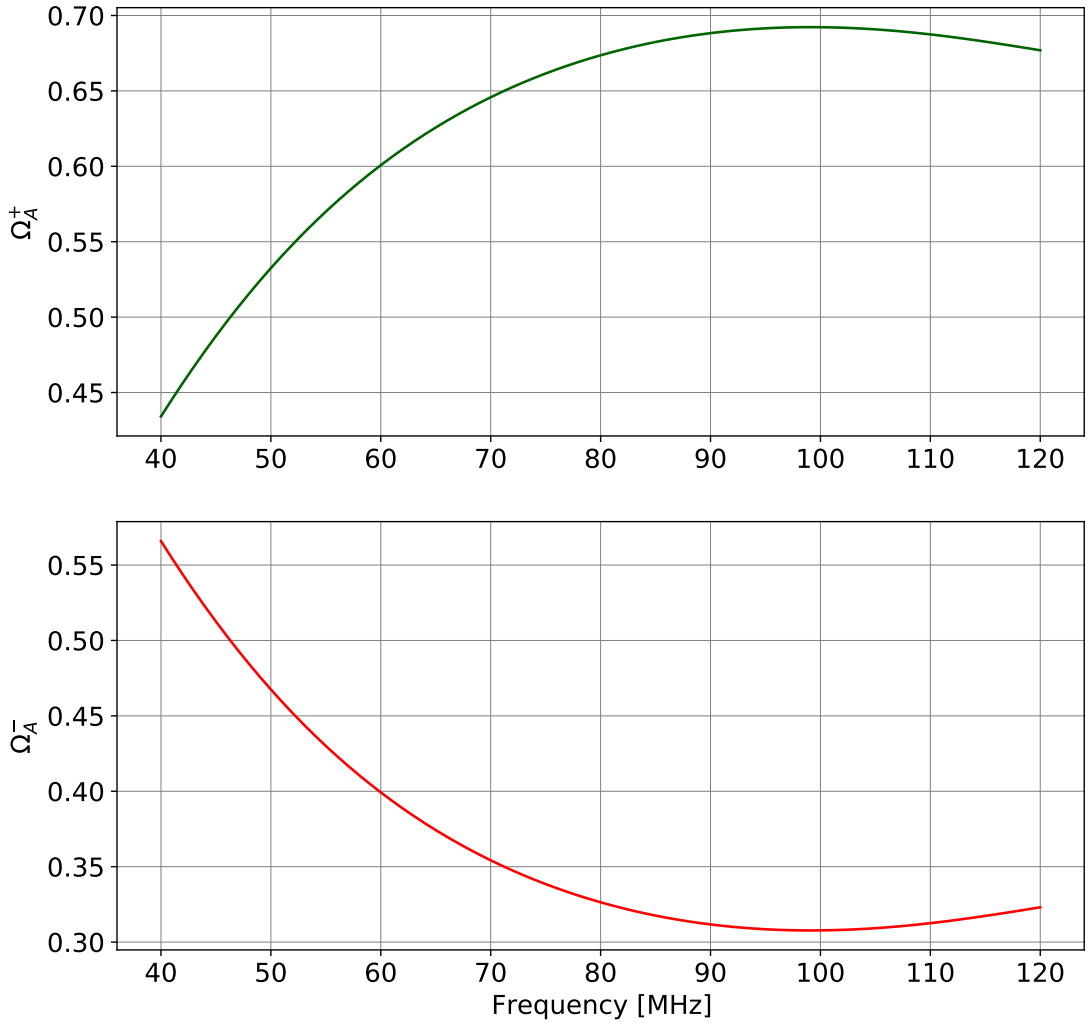

Figure 3.22: Evaluation of the MIST antenna ground loss, for a beam model of the blade antenna simulated in FEKO, with $\sigma = 0.02\text{Sm}^{-1}$, and $\epsilon_r = 3.5$. At the top, Ω_A^+, the, and at the bottom, the ground loss Ω_A^-.

3.6 Mini-MIST prototype antenna

For Mini-MIST, a smaller prototype antenna was built, with dimensions presented in Table 3.4. These dimensions were obtained by performing a manual optimization, with objectives of achieving an antenna with low chromaticities, minimal ground loss, minimal Γ, and smaller than the MIST design. In this construction, we applied some of the lessons learned with the previous MIST antenna prototype in the structure, making it more stable by adding 3-D printed fittings that go inside the fiberglass tubes and connect them in the antenna support structure.

Two small prototype antennas were constructed for the Arctic excursion that will take place in 2022, with the goal of obtaining sky measurements at two distinct locations in MARS. In Figure 3.23, we present the Mini-MIST prototype antennas. Below the antennas are the receiver, and the back-end boxes, simulating how the final configuration will be assembled on the field.

In Figure 3.24, we present Γ as a function of frequency, simulated in FEKO, with $\sigma = 0.03\mathrm{Sm}^{-1}$, and $\sigma = 0.3\mathrm{Sm}^{-1}$, with $\epsilon_r = 3.5$. These simulations were made considering the thickness of the panels, of $t = 3$ mm, and already consider the embedding of the same balun S-parameters presented in Figure 3.18, using Equation 3.6.

In comparison with the antenna designed MIST, panel (f) of Figure 3.21, the Γ for the Mini-MIST antenna does not show a sharp feature at a single frequency. For the Mini-MIST antenna simulated in Figure 3.24, there is a considerable range of frequencies, between $50 < \nu < 120$ MHz, in which the reflections are approximately at the -7 dB level and achieving as far as -13 dB at $\nu = 48$ MHz, for a soil with $\sigma = 0.03\mathrm{Sm}^{-1}$, $\epsilon_r = 3.5$. For a soil with $\sigma = 0.3\mathrm{Sm}^{-1}$, and $\epsilon_r = 3.5$, the reflections are higher, only achieving a minimum of -8 dB at frequencies above 100 MHz, and ranging between -7 dB, and -5.7 dB in the $50 < \nu < 80$ MHz frequency range. In Figure 3.25, we present the antenna beam gain, and the derivatives, for $\sigma = 0.03$, and $\epsilon_r = 3.5$.

Compared to the MIST antenna, the Mini-MIST antenna presents values for Γ that are higher across the band. The antenna is more stable due to the addition of the fittings in the support structure and for the future, Γ will be measured above soil and compared to simulations.

	Antenna dimensions [m]
Height	0.50
Separation	0.02
Length	1.20
Width	0.60

Table 3.4: Dimensions for the Mini-MIST antenna.

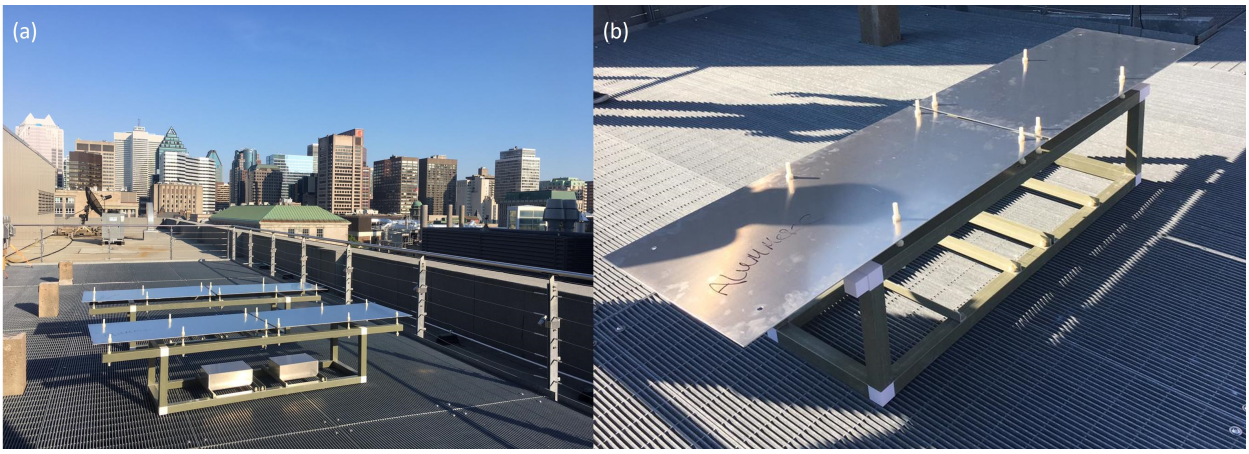

Figure 3.23: (a) shows the Mini-MIST prototype antennas sitting next to each other, with the readout boxes placed inside the structure. (b) Detail of one of the prototype antennas, with the empty space within the structure where the readout boxes are placed. The white squares in the structures represent 3D printed fittings to connect the fiberglass tubes.

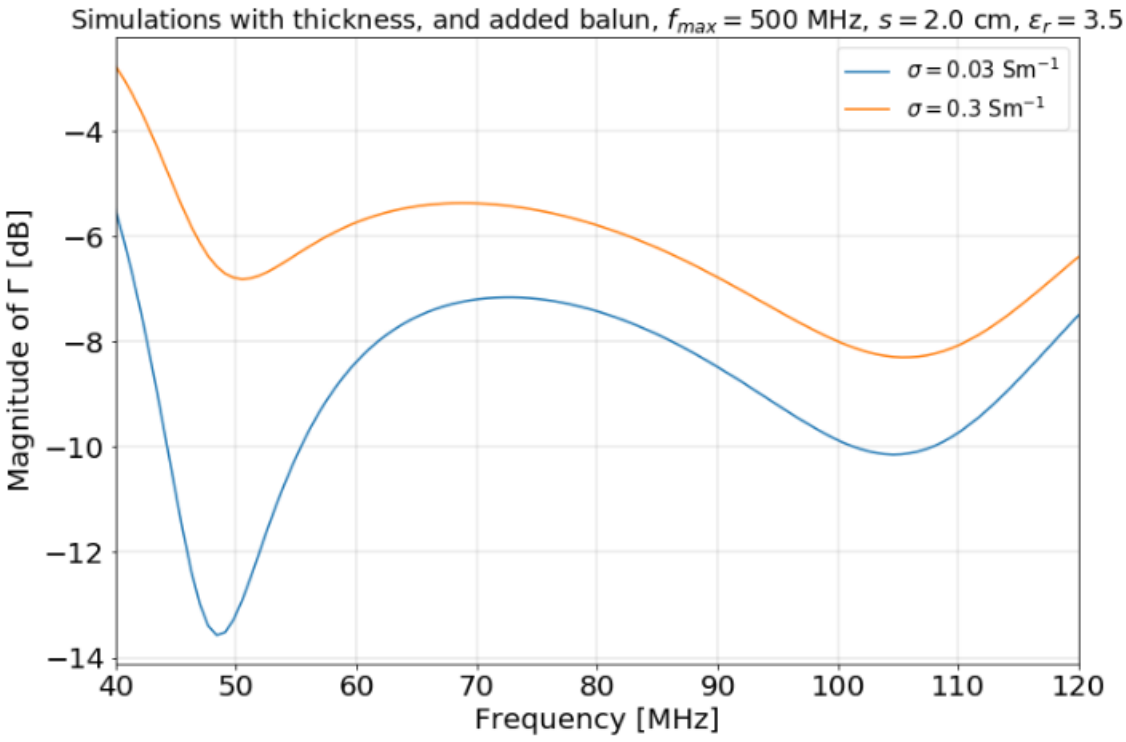

Figure 3.24: FEKO simulations for the Mini-MIST prototype antenna, considering the thickness of the panels, and the addition of the balun, for $\sigma = 0.03\text{Sm}^{-1}$, and $\sigma = 0.003\text{Sm}^{-1}$, keeping $\epsilon_r = 3.5$.

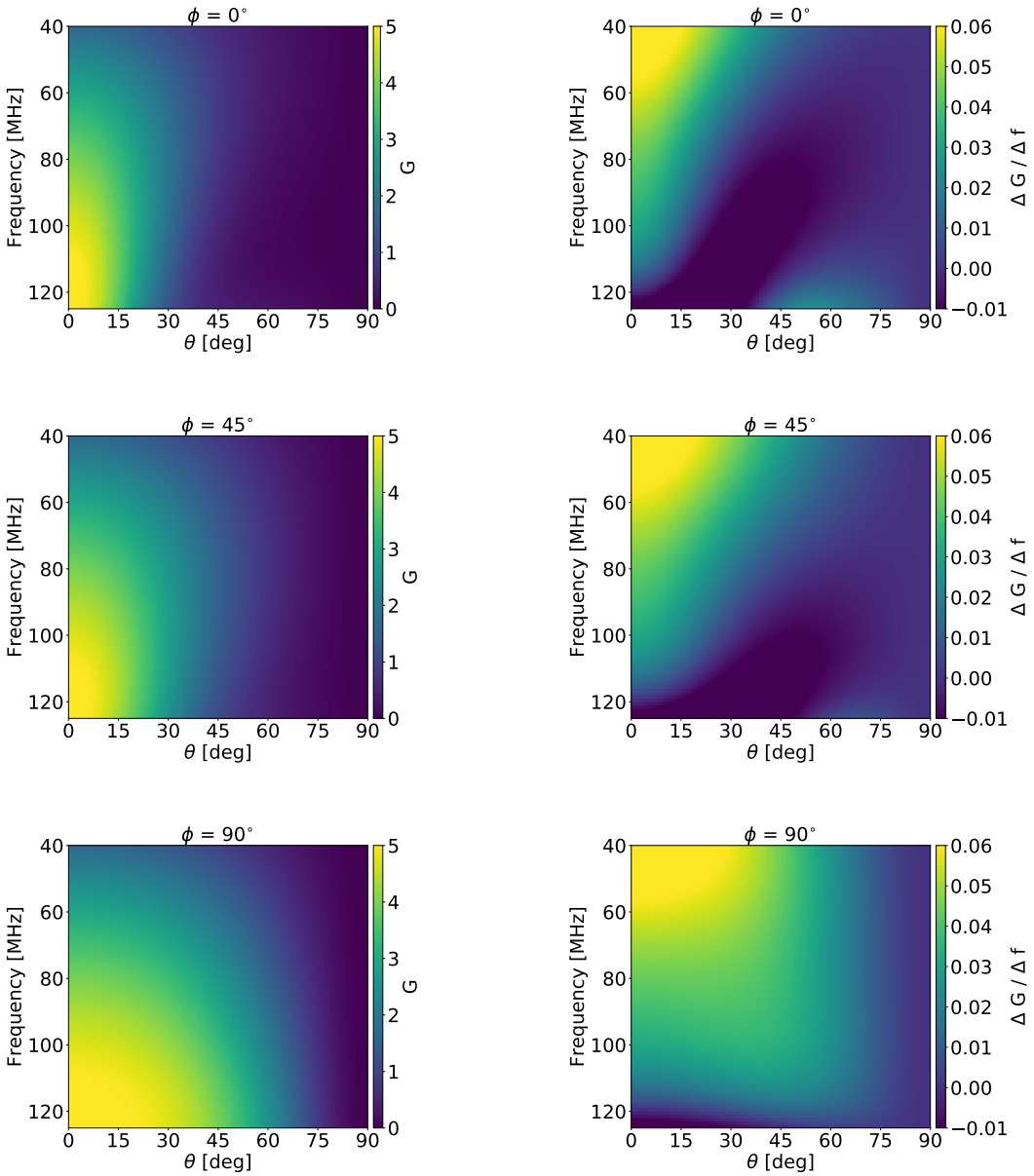

Figure 3.25: Left: Gain for the blade antenna above infinite soil with $\epsilon_r = 3.5$ and $\sigma = 0.03$ Sm^{-1}, at $\phi = 0°$, $\phi = 45°$, and $\phi = 90°$, simulated in FEKO, for the Mini-MIST antenna prototype. Right: Gain derivative as a function of frequency for the same three values of ϕ.

Chapter 4

Characterizing soil electromagnetic properties

Per ardua ad astra.

Royal Air Force

Soil characterization is essential for MIST and Mini-MIST, as soil conductivity σ, and relative permittivity ϵ_r affect Γ, and the antenna beam gain. In this chapter, we present the design and testing of a device to measure electromagnetic properties of air, and soil. These results suggested soil parameters that were used to perform FEKO simulations. Experiments and simulations were compared in terms of real, imaginary, and magnitude of impedance, and showed excellent agreement.

4.1 Soil electromagnetic properties

Soil is composed by tiny particles, which are packed together by intramolecular forces, is a dielectric. When a dielectric undergoes the action of an electric field **E**, generates a polarization

$$\mathbf{P} = \chi \mathbf{E}, \tag{4.1}$$

where χ is the dielectric susceptibility of the material. A dielectric displacement $\mathbf{D} = \epsilon_0 E + \chi \mathbf{P}$ can also be defined considering the dielectric permittivity of vacuum ϵ_0. The dielectric displacement can be written therefore as $\mathbf{D} = \epsilon \mathbf{E}$, where $\epsilon = \epsilon_0 + \chi$ [Fano, 2019].

The relative permittivity is defined as

$$\epsilon_r = \frac{\epsilon}{\epsilon_0}. \tag{4.2}$$

In non-dielectric media, **E**, and **B** are sufficient to describe a problem, and when dealing with dielectric materials, **D** and **H**. The relations between these fields can be usually written as a function of frequency, and of the electromagnetic properties as

$$\mathbf{B} = \mu(\omega)\mathbf{H} \tag{4.3}$$

$$\mathbf{D} = \epsilon(\omega)\mathbf{E} \tag{4.4}$$

$$\mathbf{J} = \sigma(\omega)\mathbf{E}. \tag{4.5}$$

σ and the relative permittivity ϵ_r can be determined experimentally using a variety of methods developed for agriculture, geophysics, and telecommunications applications [Turki et al., 2019, Parashar and Mishra, 2021].

4.2 Transmission line theory for an open-wire line

For MIST and Mini-MIST, I developed an antenna to measure soil electromagnetic properties based on transmission line theory, applicable to a range of frequencies. This antenna is composed by two rods connected to a VNA as seen in 4.1 (a), used to measure vectorially the impedance and reflections of the EM waves that are propagated through the rods into soil by the VNA. I made an approximation that layers of soil that are close to the surface are a homogeneous medium for low frequencies, and obtain the electromagnetic properties using a fit based on TL theory for the real and imaginary parts of the impedance.

A transmission line (TL) can be studied using the telegraph equations. According to the telegrapher equations, a TL can be described by elements in a model circuit presented in Figure 4.1 (b) that are infinitesimally small in length and have the following properties: conductance G, resistance R, inductance L, and capacitance C. Wave equations for voltage V and current I are obtained by applying Kirchoff's law on the nodes, and are expressed as

$$\frac{d^2V(x)}{dx^2} - \zeta^2 V(x) = 0, \tag{4.6}$$

$$\frac{d^2I(x)}{dx^2} - \zeta^2 I(x) = 0, \tag{4.7}$$

where $\zeta = \sqrt{(R + i\omega L)(G + i\omega C)}$ is the propagation constant.

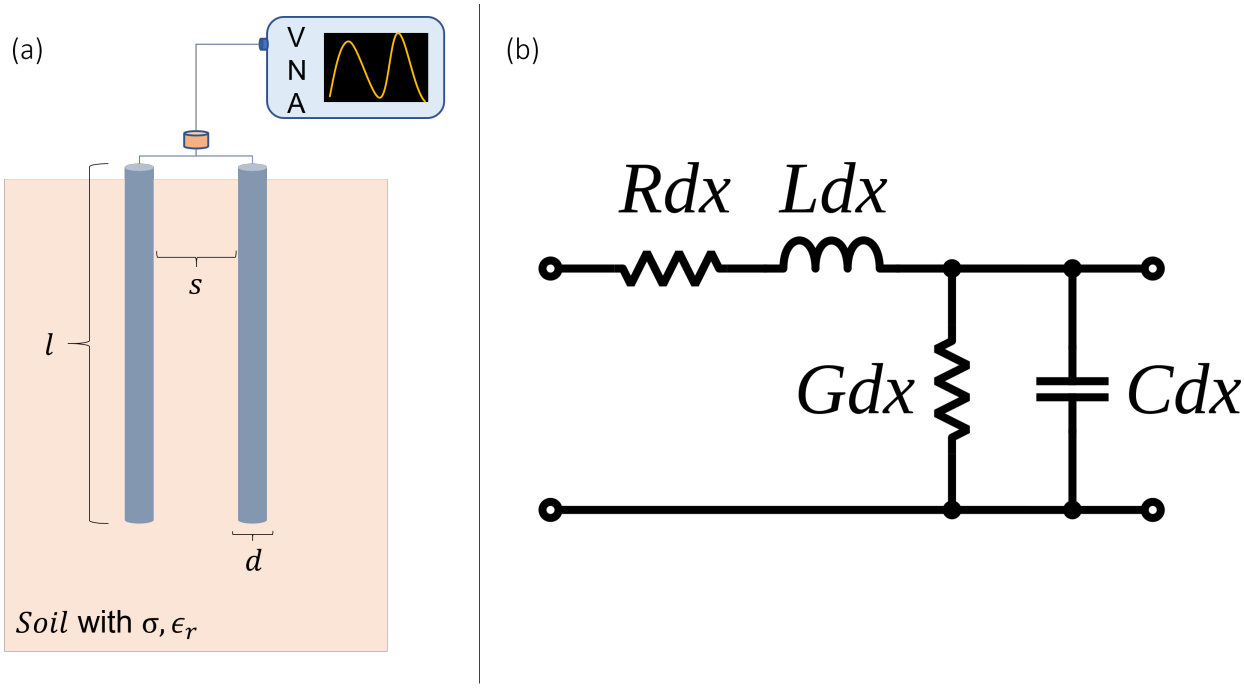

Figure 4.1: (a) Schematics of the setup to measure soil electromagnetic properties with two rods, and a VNA. (b) Schematics of a transmission line with the four elements: resistance R, conductance G, inductance L, and capacitance C. Picture taken from [Fano, 2019].

The impedance can be written as

$$z_0 = \sqrt{\frac{R + i\omega L}{G + i\omega C}}. \tag{4.8}$$

If this two-element open line is placed inside soil, the elements of the circuit can be written as a function of the soil electromagnetic properties σ, and ϵ_r.

$$C = \frac{\epsilon_r \epsilon_0 \pi}{(s/d)}, \qquad G = \frac{\sigma \pi}{(s/d)}, \qquad L = \frac{\mu_0 \mu_r}{\pi (s/d)}, \qquad R = 1.66 \times \frac{10^{-7} K \sqrt{\omega}}{d}, \tag{4.9}$$

where s is the separation between the two elements, d is the diameter of the elements, $\epsilon_0 = 8.85 \times 10^{-12}$, $\mu_0 = 1.26 \times 10^{-6}$, and $\mu_r = 1$ for the range of frequencies used. The load impedance z_l is transformed into the input impedance $_{in}$ as a function of the soil parameters, which can be extracted by minimizing

$$z_{in} = z_0 \frac{z_l \cosh(\zeta l) + z_0 \sinh(\zeta l)}{z_l \sinh(\zeta l) + z_0 \cosh(\zeta l)}, \tag{4.10}$$

where l is the length of the TL. The TL should not be electrically longer than $1/2\ \lambda$ in order for the method to work [Lau, 2010].

Figure 4.2 shows simulations for a TL of diameter $d = 4.05$ mm, and $\epsilon_r = 3.5$. Each of the four panels shows a different value for σ. The color scales indicate the difference between maximum and minimum impedance of the TL, and the axes show different lengths, and separations between the rods . This plot indicates that using smaller lengths increases the dynamic range of the measurements, at least theoretically. However, the rods need to be surrounded by and in contact soil, and therefore the TL cannot be infinitely short.

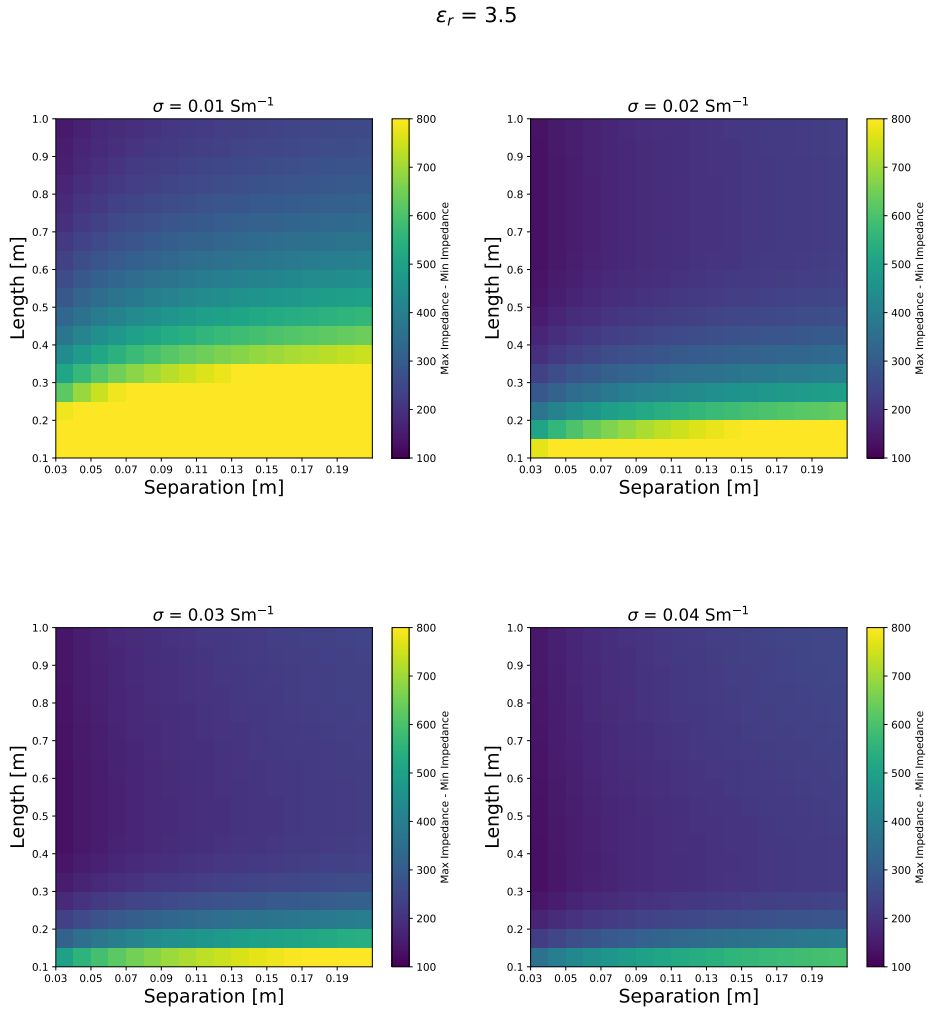

Figure 4.2: Simulations of the TL equation, with $d = 4.05$ cm, and $\epsilon_r = 3.5$. Each panel shows a different σ, for which the difference between the maximum, and minimum values of impedance was calculated for different lengths and separations. These results suggest that using a smaller TL increases the dynamic range of the measurements, for the electromagnetic properties explored.

4.3 Measurements in air

In order to verify the validity of the method, air measurements were made, since air has a known conductivity of $1 \times 10^{-15} < \sigma < 10^{-9}$ Sm^{-1} [Seran et al., 2017], and $\epsilon_r = 1.0006$ [Hector and Schultz, 1936].

The experimental setup for the air measurements is presented in Figure 4.3 and consists of two solid aluminum threaded rods attached to an SMA connector with copper wires. A fiberglass spacer was used for fixation, and to keep the separation between the rods constant. These aluminum threaded rods are connected to a VNA via coaxial cable, and the measuring plane is at the end of the cable. The VNA is calibrated using open, short, and 50 Ohm standards, as shown in Figure 4.4.

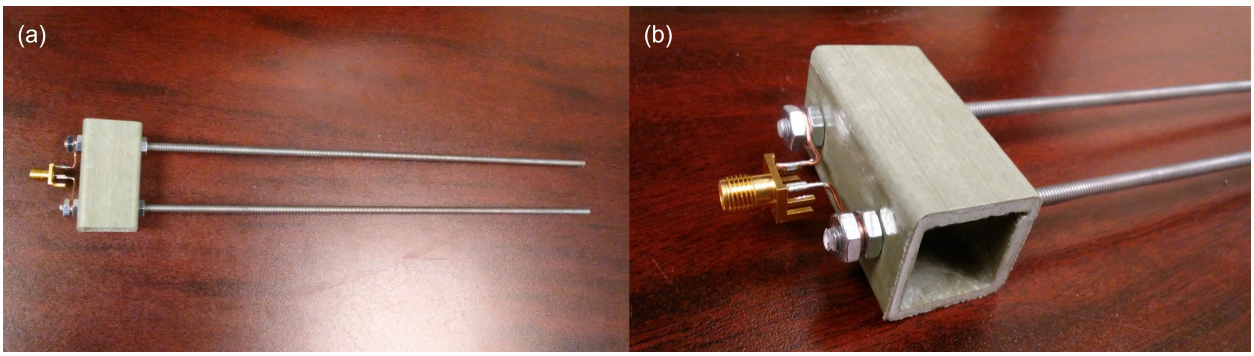

Figure 4.3: (a) Setup to measure the air properties. (b) Detail on the SMA connector on the device.

To measure the air properties, the setup was lifted at about 2m of height with respect to ground, and the impedance measurements were recorded at the VNA. The measurements happened in open air, far from walls, in to avoid reflections. The length of the rods was of $l = 29$cm, with a separation $s = 3$cm, and a diameter $d = 0.4$cm. Due to the length of the rods, the maximum frequency of 200 MHz was chosen for the fits, as it is within the $1/2\lambda$ limit for the electrical length set by the TL theory. 19 measurements were taken, and after each measurement, the cable was disconnected and reconnected from the probes in order to perform a new, fresh measurement, and to test repeatibility.

To analyze the data, we first perform an initial frequency-by-frequency minimization using Equation 4.10 for the magnitude of the impedance to get values for σ, and ϵ_r that vary across frequency. The method we propose, a uniform fit, seeks for a constant value across frequency, for both σ and ϵ_r that can describe the soil. The mean values for the distribution of σ, and ϵ_r minimization a function of frequency are used to obtain a valid initial guess for the algorithm of the uniform fit. This fit uses Equation 4.10 and fits the real and imaginary parts of the impedance using a simple chi-squared minimizer with bounds $10^{-10}\sigma < 1.0$ and $1.0 < \epsilon_r < 100$[1] to obtain

[1]The fit was implemented in curve fit, and the documentation is available here.

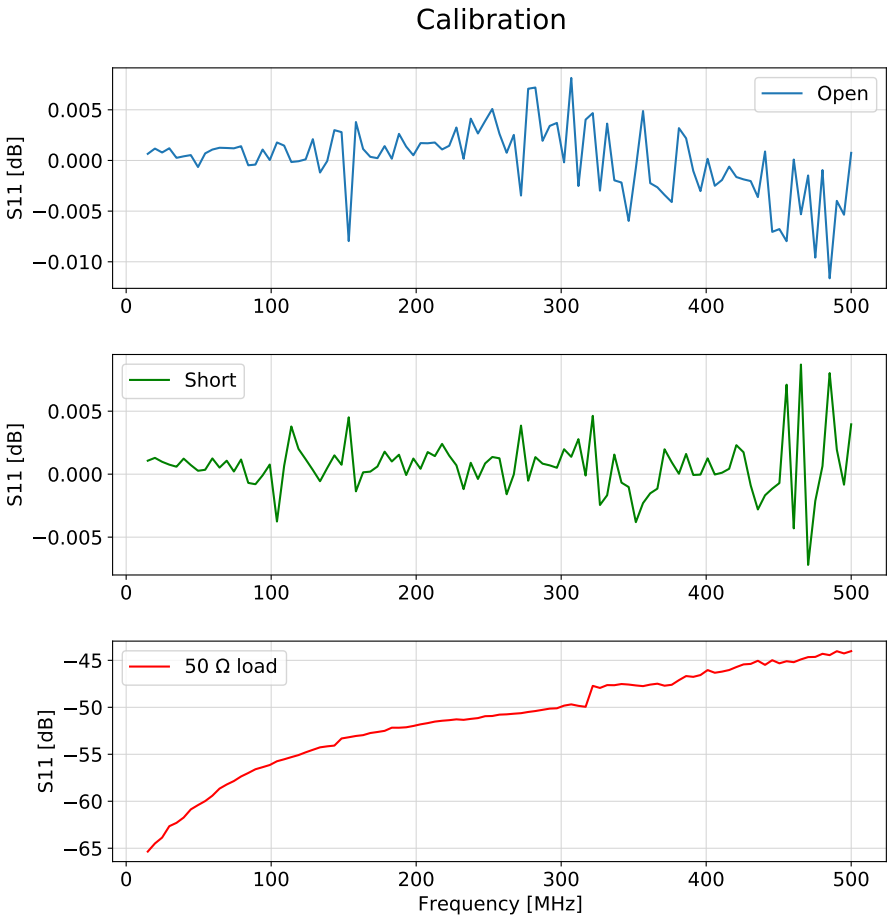

Figure 4.4: Open, short, and load standards measured after the calibration of the VNA, with the reference plane at the end of the cable that will be attached to the SMA connector of the device.

the best-fit values for σ and ϵ_r that represents the entire frequency range, as well as the covariance matrix. The fit errors were found by taking the square root of the diagonal of the covariance matrix.

We performed a weighted mean to determine the experimental electromagnetic properties for air, and the uncertainty of the measurements. The weighted mean can be written as

$$\bar{x} = \frac{\sum_{i=0}^{N} x_i w_i}{\sum_{i=0}^{N} w_i}, \tag{4.11}$$

where $w_i = 1/(\sigma_i)^2$ corresponds to the weights, and σ the error provided by the fit using the curve fit function in Python. The standard error of the weighted mean is calculated as

$$\sigma_{\bar{x}} = \sqrt{\frac{1}{\sum_{i=0}^{N} w_i^2}}. \tag{4.12}$$

The experimetally measured real and imaginary impedances showed a slight increase in amplitude as a function of frequency, as if the curve presented a slope in the y-axis. Therefore, we decided to account for this effect empirically by adding an offset and a slope for both real and imaginary parts. The final form for the fit function is

$$f(\nu, \sigma, \epsilon_r, a_1, a_2, b_1, b_2) = \left(a_1 + a_2\,\nu + \mathrm{Re}\left[z(\sigma, \epsilon_r)\right], b_1 + b_2\,\nu + \mathrm{Im}\left[z(\sigma, \epsilon_r)\right]\right), \tag{4.13}$$

where a_1 and b_1 represent the offset, a_2 and b_2 represent the slope for the real and imaginary parts, respectively.

In Figure 4.5, the measured real and imaginary parts of the impedance curve measured in one experiment (in blue), fitted with Equation 4.13 (in orange). The residuals are centered at 0 Ω, and are displayed in red. Experimentally we determined $\sigma = 1.0 \times 10^{-6} \pm 3.7 \times 10^{-6}$ Sm^{-1}, and $\epsilon_r = 1.510 \pm 0.005$, which compare well to the known parameters for air, $1 \times 10^{-15} < \sigma < 10^{-9}$ Sm^{-1} [Seran et al., 2017], and $\epsilon_r = 1.0006$ [Hector and Schultz, 1936].

In Figure 4.6, we present the comparison of five measurements against a FEKO simulation of this device to measure electromagnetic properties, where $\sigma = 1 \times 10^{-15} \mathrm{Sm}^{-1}$, and $\epsilon_r = 1.0$. Typical values for the other fitting parameters were: $a_1 = 31.9, a_2 = 5.7 \times 10^{-8}, b_1 = 68.1, b_2 = -7.2 \times 10^{-7}$. In Figure 4.5 and Figure 4.6, there are features in the real part with a maximum amplitude of 100Ω, that do not appear on the fit, and also does not appear in the FEKO simulation. One possible explanation for this effect that it was caused by the fiberglass spacer used to keep the distance between the rods constant while taking the experimental measurements, which was not accounted for in the FEKO simulation. The evaluation of the influence of spacers in the simulations is still work in progress.

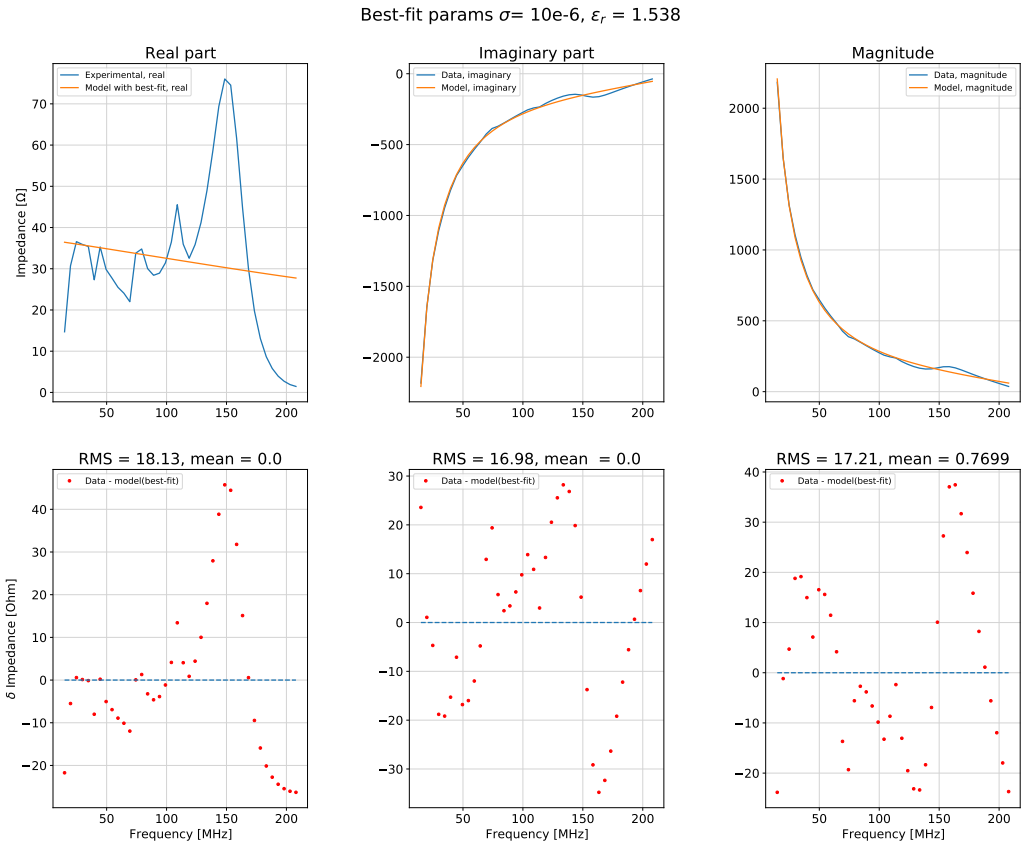

Figure 4.5: Above: Best-fit curves (in orange) for real and imaginary impedances as a function of frequency, and the resulting magnitude of impedance. The fit curve disagrees by when compared to the real part of impedance, but by a significantly lower magnitude in impedance relative to the imaginary part. The best-fit curve shows agreement in terms of the imaginary part, and the magnitude of the impedance of the experimental data. Features in the real part are noticeably smaller Below: residual plots.

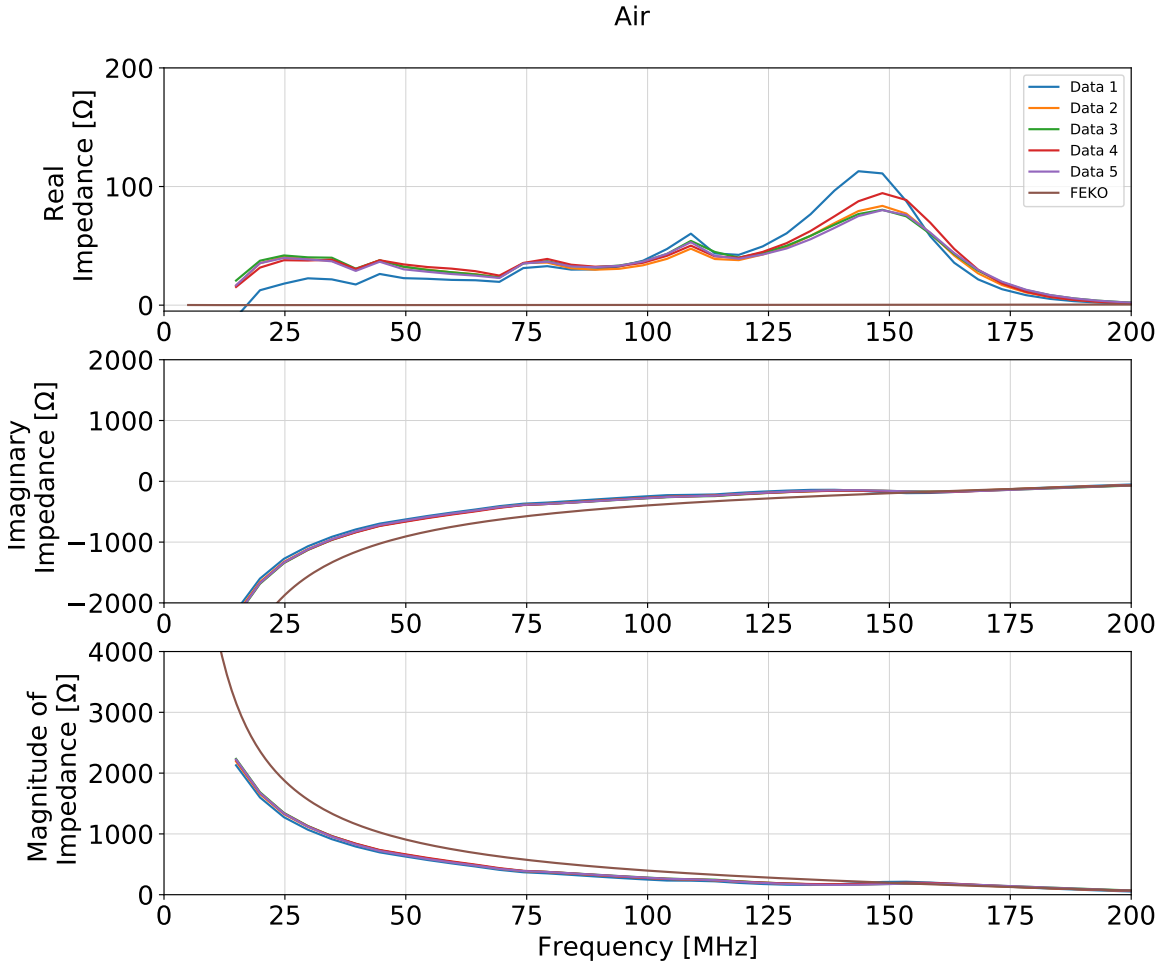

Figure 4.6: Simulations with $\epsilon_r = 1.0$, and $\sigma = 3\times10^{-15}$ Sm^{-1} for air, compared with experimental results from 5 measurements, in terms of real impedance (top), imaginary impedance (middle), and magnitude of impedance (bottom).

4.4 Soil measurements

4.4.1 Wet soil

The following measurements were taken at the McGill Space Institute's backyard, using the same aluminum rods, with the same length, separation, and diameter as for the air measurements. This soil is commonly used as a garden, and is identified wet. The procedure to perform the soil measurements was:

- inserting the threaded rods carefully, without connection with the VNA, depicted in Figure 4.7 (a), maintaining a fixed separation using the fiberlass spacer as a guide to insert the rods;
- removal of the fiberglass spacer, and connecting the rods to the VNA;
- record of the impedance measurement, depicted in Figure 4.7 (b);
- disconnection of the SMA cable and the rods;
- removal of the threaded rods from soil. The re-insertion of rods happened at the same location within the same site, 4 times. In total, 5 different locations were investigated.

Figure 4.7: (a)Threaded rods placed entirely inside soil, before being connected to the VNA. (b) Threated rods placed entirely inside soil, connected to the VNA.

For these soil measurements, the fiberglass structure was removed when taking measurements in order to avoid undesired impedance features, and to allow the rods to be fully inserted inside the ground, as shown in Figure 4.7.

To obtain the best-fit parameters, the procedure to obtain the best-fit parameters was the same as described before: perform a frequency-by-frequency minimization to obtain initial guesses, and

then perform the uniform fit with Equation 4.13 using these initial guesses. The errors in σ and ϵ_r at each location were obtained by performing a weighted average, expressed by 4.12. The maximum frequency for the fits was kept at 200 MHz.

In Figure 4.8, we present one of the impedance measurements in terms of the real part, imaginary part, and magnitude. The best-fit parameters for this specific case were $\sigma = 0.0321 \pm 0.0007$ Sm^{-1}, and $\epsilon_r = 24.03 \pm 0.09$ and typical values for the parameters were: $a_1 = -20.13, a_2 = 24.9 \times 10^{-7}, b_1 = -7.7, b_2 = -3.2 \times 10^{-7}$. In Figure 4.9, we present the comparison of one of the measurements with a FEKO simulation, using the soil parameters suggested by the fit of one curve, and the best-fit curve. We see excellent agreement between the data and the FEKO simulation: the peak in the real part of the impedance, centered at $\approx$ 100 MHz, has a magnitude that differs by 10Ω, and in the 125-200 MHz range, the differences are even lower. For the imaginary part, the agreement is better in the 35-100 MHz range, as the difference is also $\approx 2\Omega$; the magnitude of impedance shows better agreement for 50-100 MHz.

Four impedance measurements were taken at each five different locations, which were separated by approximately 1 m. Repeated measurements at a given location were made by re-inserting the rods in soil on the same holes, and reconnecting the VNA. The results are shown in Figure 4.10. Values of σ, and ϵ_r were obtained for each location after performing a weighted average of the 4 measurements. The relatively high value of ϵ_r indicates a high moisture, which confirms qualitative observations that were noticeable during the measurements that the soil is wet.

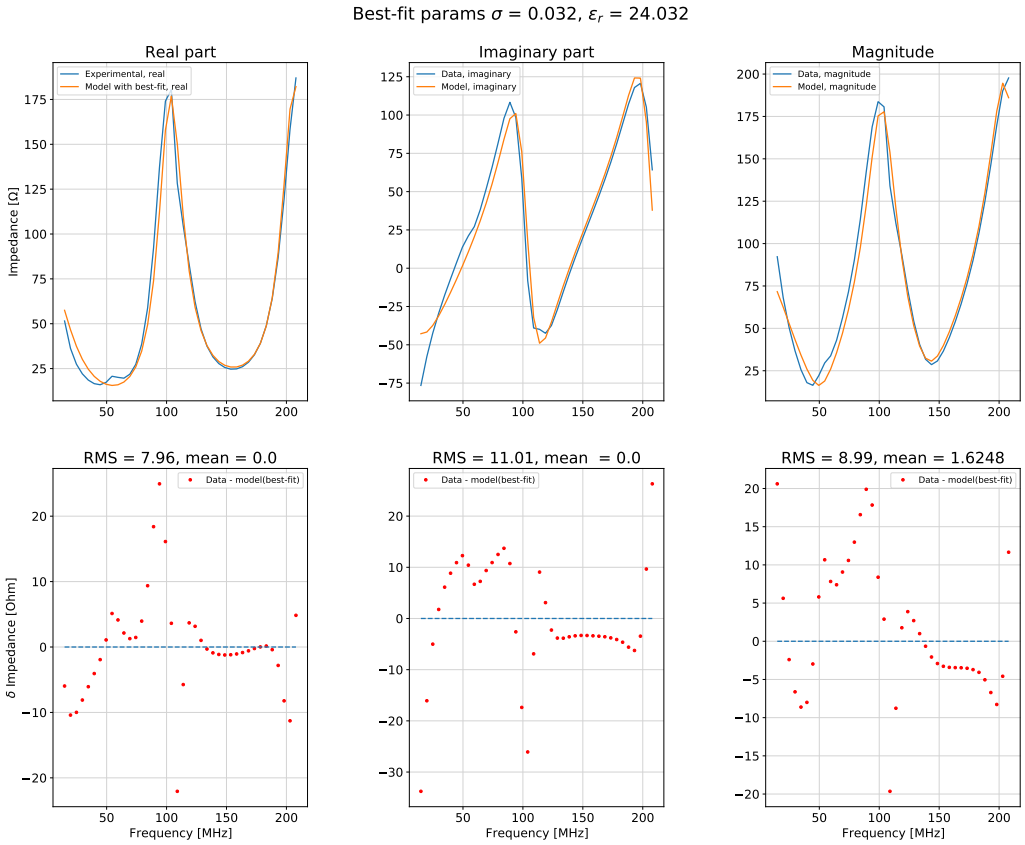

Figure 4.8: Above: Best-fit curves (in orange) for real and imaginary impedances as a function of frequency, and the magnitude of impedance. The fit curve shows agreement with the experimental data for wet soil in terms of the real and imaginary parts, and of the magnitude of the impedance. Below: residual plots.

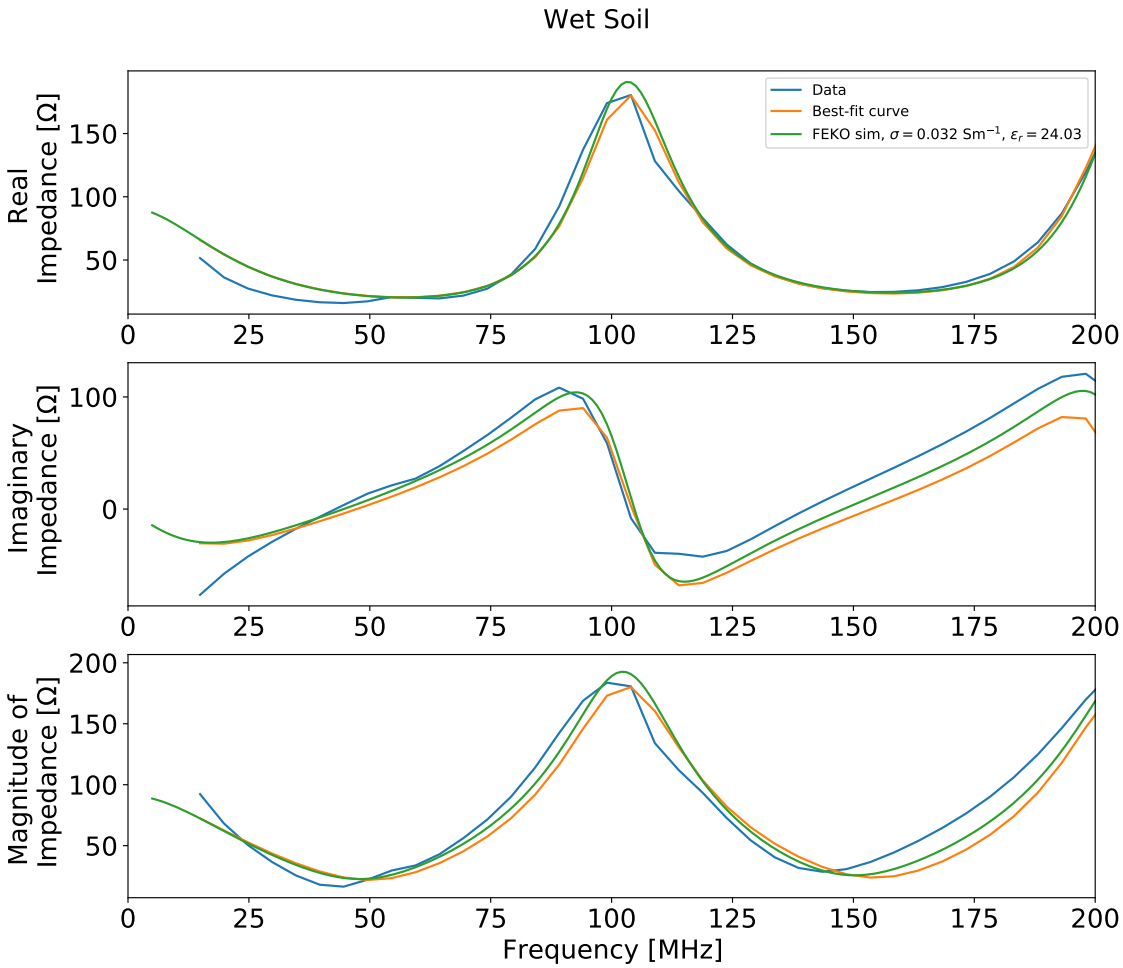

Figure 4.9: Experimental results which suggested $\epsilon_r = 24.03$, and $\sigma = 0.032$ Sm^{-1} for soil, compared to a FEKO simulation with those same soil parameters, and to the best-fit curve.

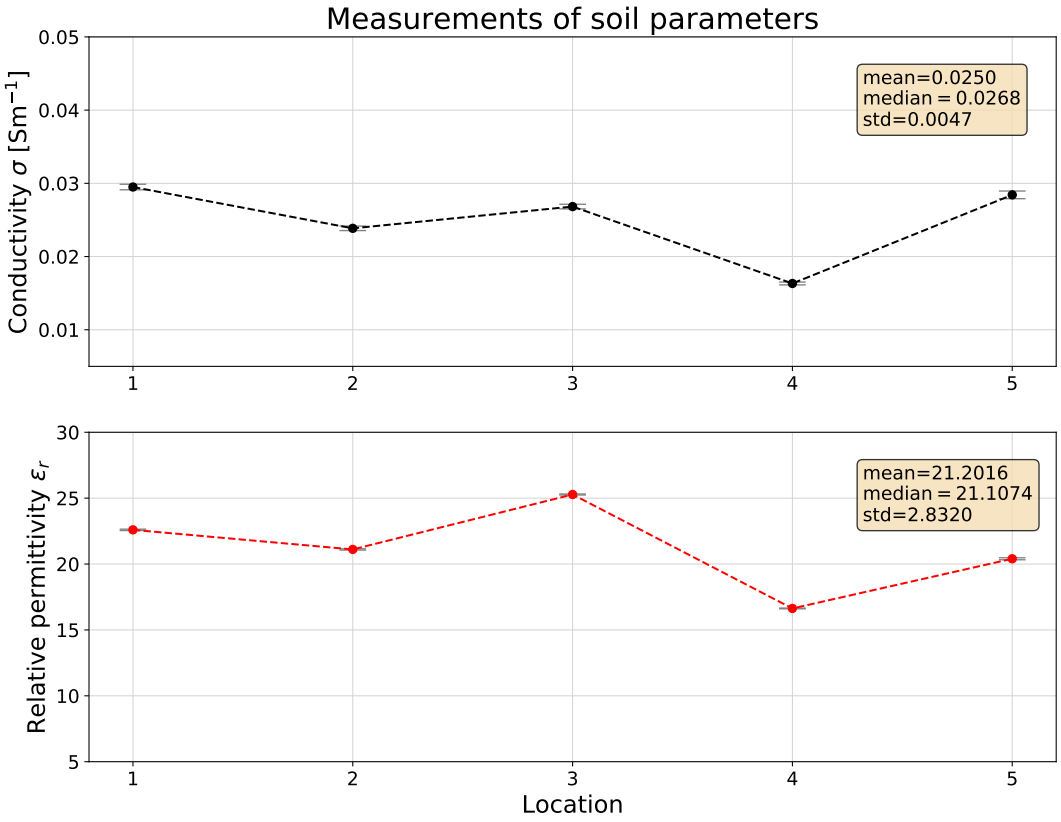

Figure 4.10: Soil parameters results at 5 different locations obtained using impedance measurements. and the weighted average (and error) of 4 repetitions at the same location. The values in the box represent the mean, median, and standard deviation, considering the 5 different locations.

4.4.2 Dry soil

The following measurements were taken at McGill's front lawn, this time using copper rods, with $l = 20$ cm, $s = 2.5$ cm, and $d = 0.63$ cm. Each measurement was taken at a different location, distant approximately 30 cm apart. The soil was drier, so in order to place the rods completely inside soil, a rubber mallet was necessary to gently hammer the rods inside soil, and this is why copper rods were used instead of aluminum ones. During the process, the rods were kept at a fixed distance by using the spacer shown in Figure 4.11 (a), which were removed to take measurements, shown in Figure 4.11 (b).

The same fitting procedure was used in these measurements. Only one measurement happened at each location this time, since sometimes holes got enlarged in the process of removing the rods from dry soil. The error for each soil parameter was taken directly from the square root of the covariance matrix provided by the output of the fitting routine. In these measurements, the maximum frequency used for the fits was 350 MHz, which is a frequency also within the theoretical electrical length size limit. In Figure 4.12, we present the example of one measurement, along with the fit, and the residuals.

Figure 4.11: (a) Spacer used to keep the separation between the rods constant while inserting them on soil. (b) Measurements of soil parameters in dry soil.

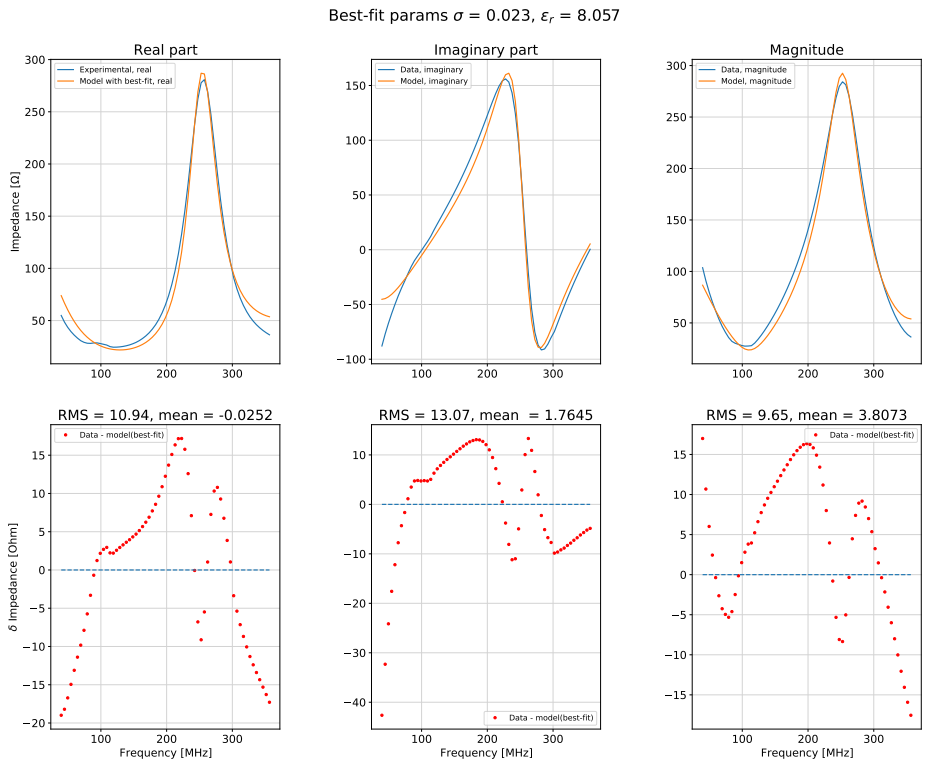

Figure 4.12: Above: Best-fit curves (in orange) for real and imaginary impedances as a function of frequency, and the magnitude of impedance. The fit curve shows agreement with the experimental data in terms of the real and imaginary parts, and of the magnitude of the impedance. Below: residual plots

The best-fit soil parameters determined experimentally were $\sigma = 0.0230 \pm 0.0003$ Sm^{-1}, and $\epsilon_r = 8.057 \pm 0.023$. Typical values for the parameters were: $a_1 = -16.69, a_2 = 1.1 \times 10^{-7}, b_1 = 4.25, b_2 = -6.51 \times 10^{-8}$. In Figure 4.9, we present the comparison of one of the measurements in dry soil with a FEKO simulation, using the soil parameters suggested by the fit, and the best-fit curve. We also see excellent agreement between the data and the FEKO simulation: for dry soil (low ϵ_r), the peak of impedance is shifted towards higher frequencies and is centered at 250 MHz, with an amplitude that differs by $\approx$5 Ω. For the imaginary part, the best agreement happens at low frequencies between 100-150 MHz, showing a difference of a few Ω, and the peak centered at 230 MHz also presents a similar shape and amplitude. Figure 4.14 shows the dispersion of electromagnetic properties for each location, with $\sigma = 0.0211 \pm 0.002$Sm^{-1}, and $\epsilon_r = 7.78 \pm 0.21$. This can be an indicator of the uniformity of the examined soil.

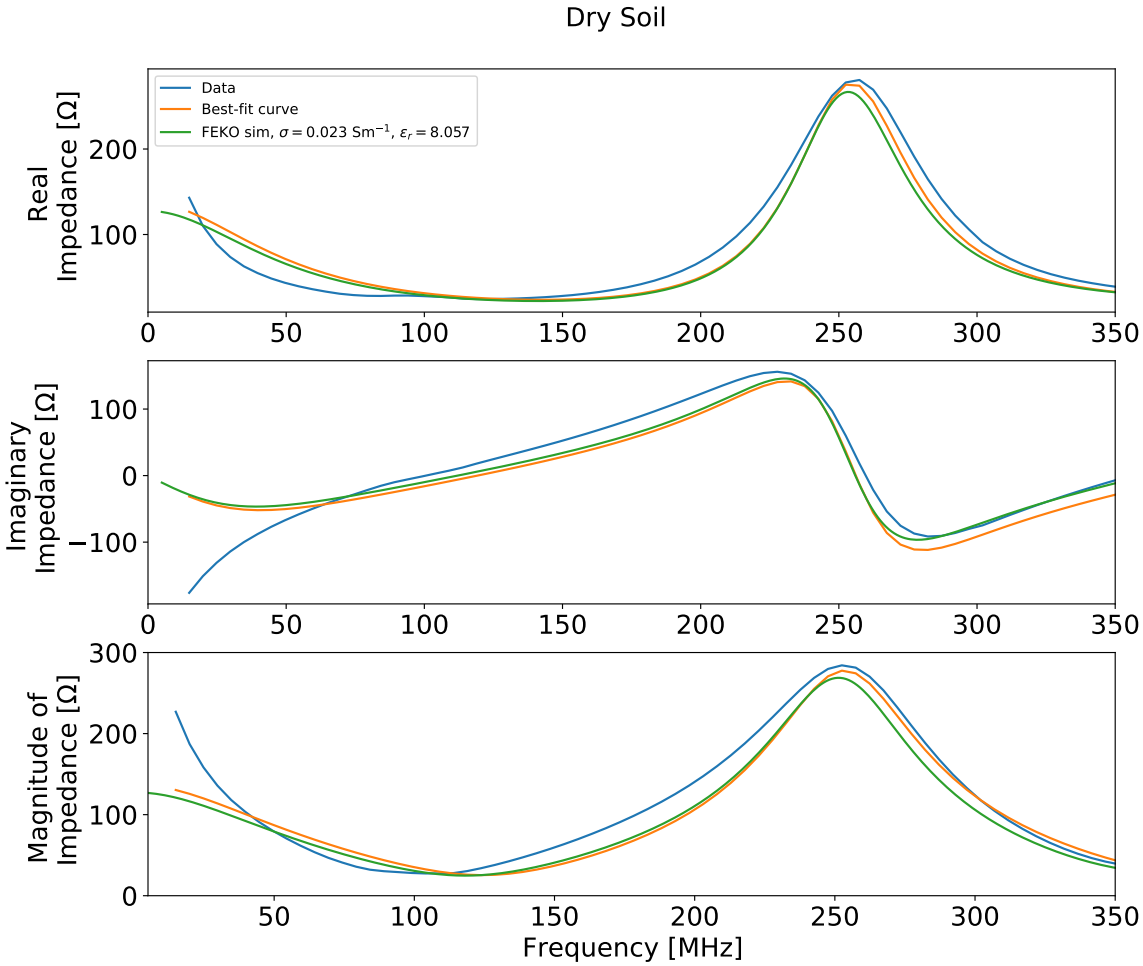

Figure 4.13: Experimental results which suggested $\epsilon_r = 8.057$, and $\sigma = 0.023$ Sm^{-1} for soil, compared to a FEKO simulation with those same soil parameters, and to the best-fit curve.

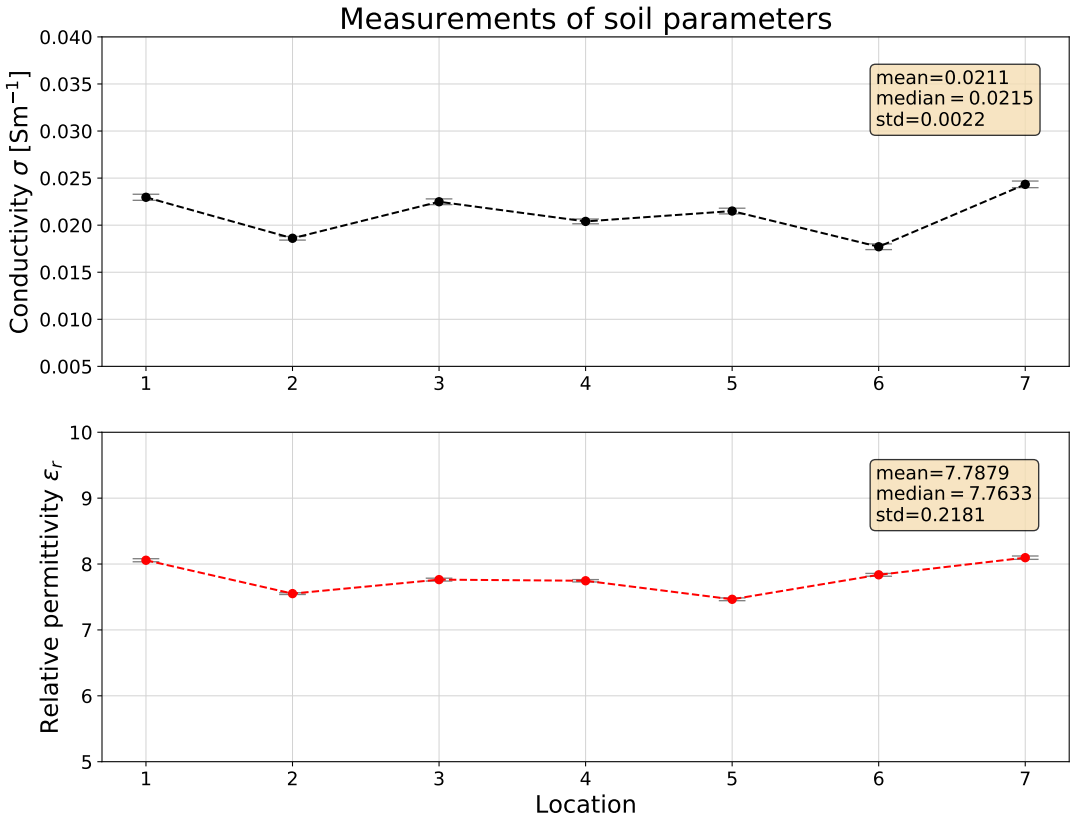

Figure 4.14: Results for soil parameters at 7 different locations. Each of the points represents a different location, and the errors were obtained by taking the square root of the covariance matrix from the fits.

4.5 Discussing results for soil characterization

For wet and dry soil, all the features in real, imaginary, and magnitude of impedance measured experimentally show agreement with simulations in FEKO over infinite soil. This is a strong evidence of the validity of the method used to obtain soil electromagnetic properties from impedance measurements. Further tests and optimizations are currently in progress.

In [Monsalve et al., 2017b] which presents the EDGES high-band results, the values for soil conductivity, $\sigma = 0.02 \mathrm{Sm}^{-1}$ and relative permittivity $\epsilon_r = 3.5$ are perturbed to determine 21-cm model rejection limits. Their results show a 1σ width uncertainty for σ and ϵ_r at the 50 % level. These uncertainties are larger in comparison to the uncertainties calculated in the experiments presented in this thesis, indicating that the precision level achieved in soil characterization is in the correct order of magnitude. When compared to FEKO simulations, soil parameter characterization has also not shown significantly different behaviors up to this point, as all impedance features are matched and comparable. For MIST and Mini-MIST we do not make use of a ground plane, therefore it is likely that we need higher precision, but this has not yet been quantified. Further work to confirm the requirements and specifications is also being done.

For field measurements, we will use a more conservative approach in terms of the errors for σ, and ϵ_r, considering independent fits for the real and imaginary parts. The uncertainty associated with a measurement will be the difference between the best-fit values for the real, and imaginary parts. Initial investigations using this more conservative approach indicate uncertainties at the 15% level for σ, and at the 2% level for ϵ_r.

Since the antenna will be placed directly above soil, a more complete description of soil in terms of its electromagnetic properties might be needed, considering the different, and deeper layers of soil. The presented method using the TL approximation is used to measure soil properties at the first layers, and does not provide information about deeper layers. For a complete soil characterization, methods such as the 4-probe-measurement using a Wenner configuration, and the usage of a ground penetrating radar (GPR) are currently being considered. A linear frequency-dependent model for σ and ϵ_r to replace the a and b parameters that were used for the fit is also currently being investigated, to determine if more physically-motivated degrees of freedom are sufficient to capture the unexplained linear slope in the measured impedances. As of it is now, our approximation is an empirically-driven model to describe the behavior of impedance as a function of frequency.

One important point is to consider is the skin depth effect. Radio waves emitted by the VNA are attenuated as they travel through soil, and their amplitude rapidly decreases as a function of depth. The skin depth δ is a distance in a given medium from a source at which the amplitude of an emitted radio wave decreases by a factor of $1/e$, and depends on soil conductivity σ, and total

permittivity $\epsilon = \epsilon_0 \epsilon_r$, and is written as

$$\delta = \left(\frac{\sqrt{2}}{\omega\sqrt{\mu\epsilon}}\right)\left[\sqrt{1+\left(\frac{\sigma}{\omega\epsilon}\right)^2}-1\right]^{-1/2}. \tag{4.14}$$

Figure 4.15 shows the different values for δ calculated using this equation. We notice that for different combinations of σ and ϵ_r, there is a decay in δ at frequencies in the $50-100$ MHz range that stabilizes at different plateaus when $\nu > 100$ MHz. These plateaus are consistent with skin depths observed in the literature for skin depth in soil [Ji et al., 2020, Edwards, 2010]. Most notably, in [Ji et al., 2020], which studies the skin depth in porous polarized media, and presents comparisons with the classic skin depth model, the exponential decay with a stabilization plateau is also observed, though for higher conductivities such as $\sigma = 0.5$ Sm^{-1}. Soils with higher conductivities also present lower values for skin depth, a tendency also observed in our experimental results. In Figure 4.16, we present the results for the median value encountered for σ, and ϵ_r.

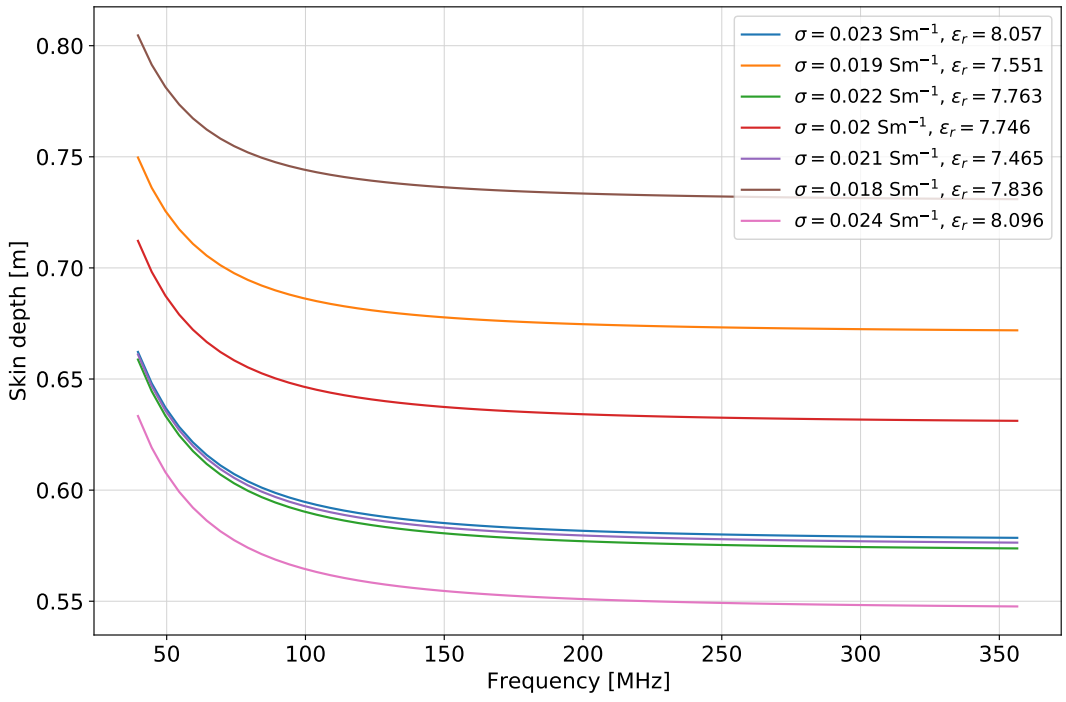

Figure 4.15: Skin depth as a function of frequency for the experimental results in dry soil. The exponential decay followed by a stabilization plateau is consistent with other models shown in the literature.

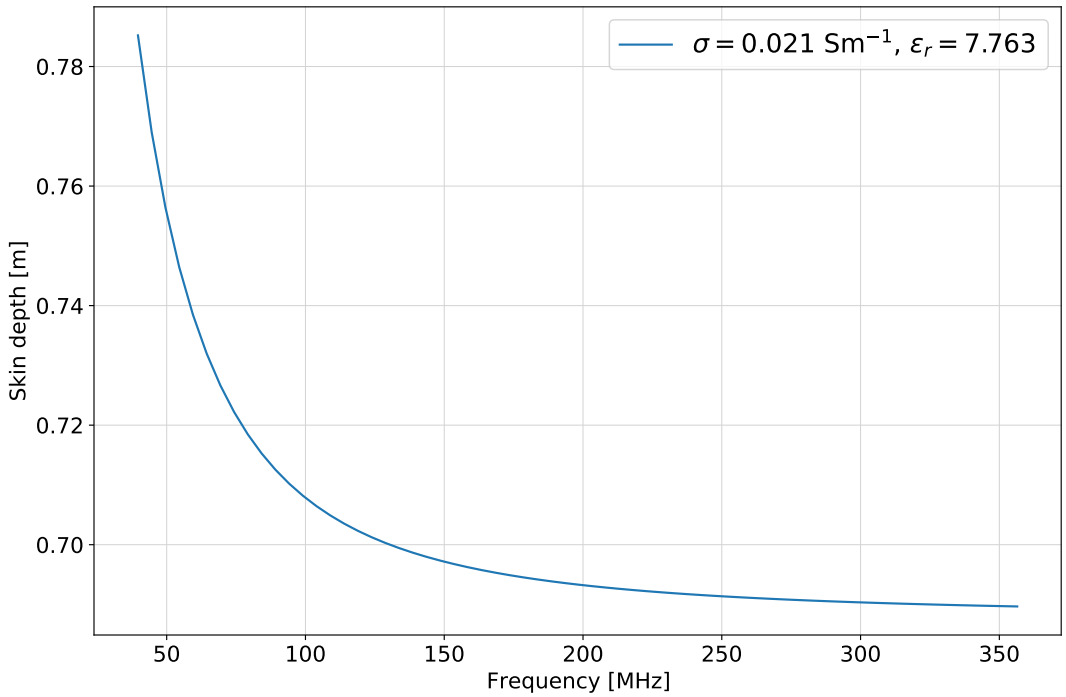

Figure 4.16: Skin depth as a function of frequency for the median value of the experimental results in dry soil.

For our applications, the importance of skin depth relies on the fact that soils can be non-uniform, and present multiple layers. The results shown in this thesis point towards a characterization of the immediate layer beneath the antenna. Results shown in Figure 4.15 show that conductivity and permittivity characterization can be considered up to 80 cm from the tip of the rods in our experiment, such that these soil parameters can be attributed to a layer of 1 m, considering the entire length of the rods used.

The effect of multiple layers of soil in antenna beam pattern, and antenna Γ has also been addressed in our explorations, but a precise comparison with experimental measurements of Γ, for example, would require a more complete characterization of soil, with a GPR, or by derivations from four-probe measurements. Such methods to characterize different layers are currently under investigation by the MIST collaboration.

Chapter 5

Conclusion and future outlook

"O correr da vida embrulha tudo. A vida é assim: esquenta e esfria, aperta e daí afrouxa, sossega e depois desinquieta. O que ela quer da gente é coragem".

Guimarães Rosa

The antenna design and instrumentation for MIST, and Mini-MIST, two experiments to measure the redshifted 21-cm global signal, were presented. Both experiments will not use make use of an electric ground plane beneath the antennas, and they will be placed directly above soil. Soil dielectric parameters affects the performance of the instrument, most notably the return loss Γ, and the beam gain; therefore, soil parameters need to be explicitly modelled and characterized. Different EM software packages were tested, in order to verify their agreement for simulations for the antenna above soil, and in the end, FEKO was chosen for being accurate enough for ground modelling.

Prototype antennas for MIST, and Mini-MIST were constructed. For the MIST antenna, Γ was measured, and simulations with different soil parameters σ, and ϵ_r were made, in order to be compared with the experimental data obtained. This was necessary, as by the time the measurements were done, there was not yet a developed method to measure the soil electromagnetic properties. The antenna dimensions for both MIST and Mini-MIST are continuously being revisited, and optimized. For Mini-MIST, further measurements of Γ over soil will be performed, and compared to simulations. Sky spectrum measurements will be used for evaluation of antenna performance.

To measure soil electromagnetic properties, a device based on the theory of transmission lines was designed, and tested in air, and in soil. To obtain the dielectric parameters, a fit was used to fit the real and imaginary impedances from the antenna, using an equation for transmission lines. The

air σ, and ϵ_r obtained experimentally were consistent with the expected values. Simulations for investigating the influence of fiberglass spacers in the experimental results for air still need to be performed. Soil measurements were also made, and compared to results from FEKO simulations, showing an excellent agreement in terms of real, and imaginary impedances. Measurements at different sites, were performed and in each, the variability of the soil parameters was investigated, and the results indicated an overall uniformity of soil in each of the sites investigated, which presented wet and dry soil.

Confirmation of soil parameters are current being tested at McGill, by making comparisons from the soil conductivity obtained by the device I proposed in this thesis with a conductivity meter, which characterizes σ using 4-probe measurements, but does not provide any information about ϵ_r. A GPR will also be used in order to characterize different layers of soil, and help confirm the values obtained for ϵ_r, but does not provide any information on σ. The most important features of the soil device presented in this thesis is that it can identify both conductivity and permittivity at the same time, with just a single measurement.

The MIST and Mini-MIST systems are at final stage of testing at the McGill Radioastronomy Laboratory. The Mini-MIST antenna will be assembled and tested on the field with all subsystems. The nearest deployment date is August 2021, in Manicouagan, a radio quiet site with low RFI levels identified in Northern Québec. During Summer 2022, the experiment will be deployed at the MARS station. During 2022, we also expect to take measurements at the Atacama Desert, in Chile.

Bibliography

[Aghanim et al., 2020] Aghanim, N., Akrami, Y., Ashdown, M., Aumont, J., Baccigalupi, C., Ballardini, M., Banday, A., Barreiro, R., Bartolo, N., Basak, S., et al. (2020). Planck 2018 results-vi. cosmological parameters. *Astronomy & Astrophysics*, 641:A6.

[Baumann, 2009] Baumann, D. (2009). Tasi lectures on inflation. *arXiv preprint arXiv:0907.5424*.

[Bernal et al., 2016] Bernal, J. L., Verde, L., and Riess, A. G. (2016). The trouble with h0. *Journal of Cosmology and Astroparticle Physics*, 2016(10):019.

[Bernardi et al., 2015] Bernardi, G., McQuinn, M., and Greenhill, L. (2015). Foreground model and antenna calibration errors in the measurement of the sky-averaged λ21 cm signal at z 20. *The Astrophysical Journal*, 799(1):90.

[Bowman et al., 2018] Bowman, J. D., Rogers, A. E., Monsalve, R. A., Mozdzen, T. J., and Mahesh, N. (2018). An absorption profile centred at 78 megahertz in the sky-averaged spectrum. *Nature*, 555(7694):67–70.

[Bradley et al., 2019] Bradley, R. F., Tauscher, K., Rapetti, D., and Burns, J. O. (2019). A ground plane artifact that induces an absorption profile in averaged spectra from global 21 cm measurements, with possible application to edges. *The Astrophysical Journal*, 874(2):153.

[Brandenberger, 2000] Brandenberger, R. H. (2000). Inflationary cosmology: Progress and problems. In *Large Scale Structure Formation*, pages 169–211. Springer.

[Brandenberger, 2004] Brandenberger, R. H. (2004). Lectures on the theory ofácosmologicaláperturbations. In *The Early Universe and Observational Cosmology*, pages 127–167. Springer.

[Brandenberger, 2011] Brandenberger, R. H. (2011). Introduction to early universe cosmology. *arXiv preprint arXiv:1103.2271*.

[Breysse et al., 2018] Breysse, P. C., Ali-Haïmoud, Y., and Hirata, C. M. (2018). Ultimate frontier of 21-cm cosmology. *Physical Review D*, 98(4):043520.

[Chiang et al., 2020] Chiang, H., Dyson, T., Egan, E., Eyono, S., Ghazi, N., Hickish, J., Jauregui-Garcia, J., Manukha, V., Ménard, T., Moso, T., et al. (2020). The array of long baseline antennas for taking radio observations from the sub-antarctic. *arXiv preprint arXiv:2008.12208*.

[Chiang, 2009] Chiang, H. C. (2009). *Observation of cosmic microwave background polarization with BICEP*. PhD thesis, California Institute of Technology.

[de Lera Acedo, 2019] de Lera Acedo, E. (2019). Reach: Radio experiment for the analysis of cosmic hydrogen. In *2019 International Conference on Electromagnetics in Advanced Applications (ICEAA)*, pages 0626–0629. IEEE.

[DeBoer et al., 2017] DeBoer, D. R., Parsons, A. R., Aguirre, J. E., Alexander, P., Ali, Z. S., Beardsley, A. P., Bernardi, G., Bowman, J. D., Bradley, R. F., Carilli, C. L., et al. (2017). Hydrogen epoch of reionization array (hera). *Publications of the Astronomical Society of the Pacific*, 129(974):045001.

[Dyson et al., 2020] Dyson, T., Chiang, H., Egan, E., Ghazi, N., Menard, T., Monsalve, R., Moso, T., Peterson, J., Sievers, J., and Tartakovsky, S. (2020). Radio-frequency interference at the mcgill arctic research station. *arXiv preprint arXiv:2012.06521*.

[Edwards, 2010] Edwards, R. (2010). Rf skin depth in the ground vs. frequency for given soil characteristics. *Ground Systems, Tigertek Inc*.

[Ellingson et al., 2009] Ellingson, S. W., Clarke, T. E., Cohen, A., Craig, J., Kassim, N. E., Pihlstrom, Y., Rickard, L. J., and Taylor, G. B. (2009). The long wavelength array. *Proceedings of the IEEE*, 97(8):1421–1430.

[Fano, 2019] Fano, W. G. (2019). The electrical properties of soils with their applications to agriculture, geophysics, and engineering. In *Electromagnetic Field Radiation in Matter*. IntechOpen.

[Fialkov and Barkana, 2019] Fialkov, A. and Barkana, R. (2019). Signature of excess radio background in the 21-cm global signal and power spectrum. *Monthly Notices of the Royal Astronomical Society*, 486(2):1763–1773.

[Fialkov et al., 2018] Fialkov, A., Barkana, R., and Cohen, A. (2018). Constraining baryon–dark-matter scattering with the cosmic dawn 21-cm signal. *Physical review letters*, 121(1):011101.

[Field, 1958] Field, G. B. (1958). Excitation of the hydrogen 21-cm line. *Proceedings of the IRE*, 46(1):240–250.

[Fixsen et al., 1996] Fixsen, D., Cheng, E., Gales, J., Mather, J. C., Shafer, R., and Wright, E. (1996). The cosmic microwave background spectrum from the full cobe* firas data set. *The Astrophysical Journal*, 473(2):576.

[Furlanetto et al., 2006] Furlanetto, S. R., Oh, S. P., and Briggs, F. H. (2006). Cosmology at low frequencies: The 21 cm transition and the high-redshift universe. *Physics reports*, 433(4-6):181–301.

[Griffiths, 1982] Griffiths, D. J. (1982). Hyperfine splitting in the ground state of hydrogen. *American Journal of physics*, 50(8):698–703.

[Hector and Schultz, 1936] Hector, L. and Schultz, H. (1936). The dielectric constant of air at radiofrequencies. *Physics*, 7(4):133–136.

[Hubble, 1929] Hubble, E. (1929). A relation between distance and radial velocity among extra-galactic nebulae. *Proceedings of the national academy of sciences*, 15(3):168–173.

[Ji et al., 2020] Ji, Y., Meng, X., Shao, J., Wu, Y., and Wu, Q. (2020). The generalized skin depth for polarized porous media based on the cole–cole model. *Applied Sciences*, 10(4):1456.

[Klöckner et al., 2013] Klöckner, H.-R., Kramer, M., Falcke, H., Schwarz, D., Eckart, A., Kauffmann, G., and Zensus, A. (2013). Pathway to the square kilometre array. *arXiv preprint arXiv:1301.4124*.

[Lau, 2010] Lau, H. (2010). Measurement of the ground (soil) conductivity and relative permittivity at high frequency using an open wire line (owl).

[Liu and Shaw, 2020] Liu, A. and Shaw, J. R. (2020). Data analysis for precision 21 cm cosmology. *Publications of the Astronomical Society of the Pacific*, 132(1012):062001.

[Miralda-Escudé, 2003] Miralda-Escudé, J. (2003). The dark age of the universe. *Science*, 300(5627):1904–1909.

[Monsalve et al., 2019] Monsalve, R. A., Fialkov, A., Bowman, J. D., Rogers, A. E., Mozdzen, T. J., Cohen, A., Barkana, R., and Mahesh, N. (2019). Results from edges high-band. iii. new constraints on parameters of the early universe. *The Astrophysical Journal*, 875(1):67.

[Monsalve et al., 2017a] Monsalve, R. A., Rogers, A. E., Bowman, J. D., and Mozdzen, T. J. (2017a). Calibration of the edges high-band receiver to observe the global 21 cm signature from the epoch of reionization. *The Astrophysical Journal*, 835(1):49.

[Monsalve et al., 2017b] Monsalve, R. A., Rogers, A. E., Bowman, J. D., and Mozdzen, T. J. (2017b). Results from edges high-band. i. constraints on phenomenological models for the global 21 cm signal. *The Astrophysical Journal*, 847(1):64.

[Monsalve et al., 2016] Monsalve, R. A., Rogers, A. E., Mozdzen, T. J., and Bowman, J. D. (2016). One-port direct/reverse method for characterizing vna calibration standards. *IEEE Transactions on Microwave Theory and Techniques*, 64(8):2631–2639.

[Nambissan et al., 2021] Nambissan, J., Subrahmanyan, R., Somashekar, R., Shankar, N. U., Singh, S., Raghunathan, A., Girish, B., Srivani, K., and Rao, M. S. (2021). Saras 3 cd/eor radiometer: design and performance of the receiver. *Experimental Astronomy*, pages 1–42.

[Nhan et al., 2018] Nhan, B., Bradley, R. F., and Burns, J. O. (2018). The cosmic twilight polarimeter: A model-independent approach to measure the sky-averaged foreground spectrum for global 21-cm cosmology. In *American Astronomical Society Meeting Abstracts# 232*, volume 232, pages 102–04.

[Otárola et al., 2014] Otárola, A., Nagar, N., Bustos, R., and Rubio, M. (2014). Parque astronómico de atacama: An ideal site for millimeter, submillimeter, and mid-infrared astronomy.

[Paciga et al., 2011] Paciga, G., Chang, T.-C., Gupta, Y., Nityanada, R., Odegova, J., Pen, U.-L., Peterson, J. B., Roy, J., and Sigurdson, K. (2011). The gmrt epoch of reionization experiment: a new upper limit on the neutral hydrogen power spectrum at z 8.6. *Monthly Notices of the Royal Astronomical Society*, 413(2):1174–1183.

[Parashar and Mishra, 2021] Parashar, V. and Mishra, B. (2021). Designing efficient soil resistivity measurement technique for agricultural wireless sensor network. *International Journal of Communication Systems*, 34(8):e4785.

[Penzias and Wilson, 1965] Penzias, A. A. and Wilson, R. W. (1965). A measurement of excess antenna temperature at 4080 mc/s. *The Astrophysical Journal*, 142:419–421.

[Philip et al., 2019] Philip, L., Abdurashidova, Z., Chiang, H., Ghazi, N., Gumba, A., Heilgendorff, H., Jáuregui-García, J., Malepe, K., Nunhokee, C., Peterson, J., et al. (2019). Probing radio intensity at high-z from marion: 2017 instrument. *Journal of Astronomical Instrumentation*, 8(02):1950004.

[Price et al., 2018] Price, D., Greenhill, L., Fialkov, A., Bernardi, G., Garsden, H., Barsdell, B., Kocz, J., Anderson, M., Bourke, S., Craig, J., et al. (2018). Design and characterization of the large-aperture experiment to detect the dark age (leda) radiometer systems. *Monthly Notices of the Royal Astronomical Society*, 478(3):4193–4213.

[Pritchard and Loeb, 2012] Pritchard, J. R. and Loeb, A. (2012). 21 cm cosmology in the 21st century. *Reports on Progress in Physics*, 75(8):086901.

[Rogers and Bowman, 2012] Rogers, A. E. and Bowman, J. D. (2012). Absolute calibration of a wideband antenna and spectrometer for sky noise spectral index measurements. *arXiv preprint arXiv:1209.1106*.

[Rybicki and Lightman, 2008] Rybicki, G. B. and Lightman, A. P. (2008). *Radiative processes in astrophysics*. John Wiley & Sons.

[Seran et al., 2017] Seran, E., Godefroy, M., Pili, E., Michielsen, N., and Bondiguel, S. (2017). What we can learn from measurements of air electric conductivity in 222rn-rich atmosphere. *Earth and Space Science*, 4(2):91–106.

[Singh et al., 2018] Singh, S., Subrahmanyan, R., Shankar, N. U., Rao, M. S., Girish, B., Raghunathan, A., Somashekar, R., and Srivani, K. (2018). Saras 2: a spectral radiometer for probing cosmic dawn and the epoch of reionization through detection of the global 21-cm signal. *Experimental Astronomy*, 45(2):269–314.

[Sokolowski et al., 2015] Sokolowski, M., Tremblay, S. E., Wayth, R. B., Tingay, S. J., Clarke, N., Roberts, P., Waterson, M., Ekers, R. D., Hall, P., Lewis, M., et al. (2015). Bighorns-broadband instrument for global hydrogen reionisation signal. *Publications of the Astronomical Society of Australia*, 32.

[Sutinjo et al., 2015] Sutinjo, A., Colegate, T., Wayth, R., Hall, P., de Lera Acedo, E., Booler, T., Faulkner, A., Feng, L., Hurley-Walker, N., Juswardy, B., et al. (2015). Characterization of a low-frequency radio astronomy prototype array in western australia. *IEEE Transactions on Antennas and Propagation*, 63(12):5433–5442.

[Turki et al., 2019] Turki, N., Elaoud, A., Gabtni, H., Trabelsi, I., and Khalfallah, K. K. (2019). Agricultural soil characterization using 2d electrical resistivity tomography (ert) after direct and intermittent digestate application. *Arabian Journal of Geosciences*, 12(14):1–11.

[van Haarlem et al., 2013] van Haarlem, M. P., Wise, M. W., Gunst, A., Heald, G., McKean, J. P., Hessels, J. W., de Bruyn, A. G., Nijboer, R., Swinbank, J., Fallows, R., et al. (2013). Lofar: The low-frequency array. *Astronomy & astrophysics*, 556:A2.

[Voytek et al., 2014] Voytek, T. C., Natarajan, A., García, J. M. J., Peterson, J. B., and López-Cruz, O. (2014). Probing the dark ages at z 20: The sci-hi 21 cm all-sky spectrum experiment. *The Astrophysical Journal Letters*, 782(1):L9.

[Wiklind et al., 2012] Wiklind, T., Mobasher, B., and Bromm, V. (2012). *The first galaxies: theoretical predictions and observational clues*, volume 396. Springer Science & Business Media.

[Wouthuysen, 1952] Wouthuysen, S. (1952). On the excitation mechanism of the 21-cm (radio-frequency) interstellar hydrogen emission line. *The Astronomical Journal*, 57:31–32.

[Zaroubi, 2013] Zaroubi, S. (2013). The epoch of reionization. *The First Galaxies*, pages 45–101.

[Zheng et al., 2017] Zheng, H., Tegmark, M., Dillon, J. S., Kim, D. A., Liu, A., Neben, A., Jonas, J., Reich, P., and Reich, W. (2017). An improved model of diffuse galactic radio emission from 10 mhz to 5 thz. *Monthly Notices of the Royal Astronomical Society*, 464(3):3486–3497.